TUSCIA UNIVERSITY

DEPARTMENT OF SCIENCES AND TECHNOLOGY FOR AGRICULTURE, FORESTRY, NATURE AND ENERGY

PhD course in

Agricultural and Forestry Engineering - XXVII Cycle

HEAT TRANSFER SIMULATION IN ENERGY - EFFICIENT SOLUTIONS BY MEANS OF FEM AND FDM: AN APPLICATION TO THREE DIFFERENT CASE STUDIES

(Scientific disciplinary sector: ING-IND/09)

PhD candidate:

Elena Allegrini

Elena Allegrini

Course Coordinator:

Prof. Massimo Cecchini

Tutor:

Prof. Maurizio Carlini

Maurizio Carlini

Date of dissertation defence

May 4, 2015

Contents

NOMENCLATURE

Roman letters

A	Overall heat exchange area (m^2)
A_f	Area of the frame (m^2)
A_g	Area of the glass (m^2)
$[B]$	Matrix for temperature gradients interpolation
C	Conductivity of non homogeneous materials ($W/m^2/K$)
c_p	Specific heat capacity [J/ (kg x K)]
d_{ext}	External diameter of the pipe (m)
d_{int}	Internal diameter of the pipe (m)
dT/dx	Temperature gradient (K/m)
EP_{DHW}	Total primary energy consumption for domestic hot water ($kWh/m^3/year$) or ($kWh/m^2/year$)
EP_{GL}	Global primary energy consumption ($kWh/m^3/year$) or ($kWh/m^2/year$)
EP_W	Global energy performance indicator for winter heating ($kWh/m^3/year$) or ($kWh/m^2/year$)
$\{f\}$	Global load vector
$\{f\}_e$	Load vector for the individual element *e*
g	Acceleration of gravity (m/s^2)
G	Heat generated in the control volume (W/m^3)
G_λ	Spectral irradiation (W/m^2)
$G_{\lambda,abs}$	Absorbed radiation (W/ m^2)
$G_{\lambda,ref}$	Reflected radiation (W/ m^2)
$G_{\lambda,tr}$	Transmitted radiation (W/ m^2)
Gr	Grashof number (dimensionless)
h	Convection heat transfer coefficient (W/m^2)
h_{io}	Heat transfer coefficient inside the pipe ($W/m^2/K$)
h_{eo}	Heat transfer coefficient in the groundwater basin ($W/m^2/K$)
I_g	Perimeter of the glass (m)
$I_{\varphi,T}$	Solar radiation at latitude φ (W/m^2)

$I_{\varphi,R1}$	Solar radiation at the lower latitude if compared to φ (W/m^2)
$I_{\varphi,R2}$	Solar radiation at the higher latitude if compared to φ (W/m^2)
k	Thermal conductivity [W/(m x K)]
[K]	Global Left Side Hand matrix
$[K]_e$	Left Side Hand matrix for the element *e*
l	Length of a one-dimensional linear element
L	Characteristic length (m)
m	Flow rate (m^3/s)
n	Time step
n	Spatial coordinate pointing into the solid
n_{norm}	Outward direction normal to the surface
{n}	Outer normal to the surface of the body
[N]	Matrix of shape functions
N_i	Shape function
N_m	Number of material components forming the solid
Nu	Nusselt number (dimensionless)
p	Pressure (Pa)
P	Perimeter (m)
Pr	Prandtl number (dimensionless)
q_r	Incoming heat flux (W/m^2)
q_s	Specified heat flux (W/m^2)
q_{tr}	Power transmitted through the wall (W/m^2)
q_x	Heat flux in the x direction (W/m^2)
q_y	Heat flux in the y direction (W/m^2)
q_z	Heat flux in the z direction (W/m^2)
q_{conv}	Convective heat flux (W/m^2)
q_{rad}	Radiative heat flux (W/m^2)
Q	Withdrawable heat (W)
R	Fouling factor (dimensionless)
R_a	Thermal resistance of gap (m^2K/W)
Ra	Rayleigh number (dimensionless)
Re	Reynolds number (dimensionless)
Rsi	Internal resistance (m^2K/W)
Rse	External resistance (m^2K/W)

s_i	Thickness of the layer within the wall (m)
S_1	Surface where T_s is specified
S_2	Surface where q_s is given
S_3	Surface where the convection boundary condition occurs
S_4	Surface where the radiation boundary condition occurs
t	Time (s)
T	Temperature (K)
{T}	Global unknown vector of temperature
T_e	Known environmental temperature (K)
T_{ext}	Water temperature inside the well (K)
T_f	Temperature of the fluid (K)
T_g	Gas temperature in the centre of the first gas phase cell (K)
T_{in}	Water temperature at the beginning of the pipe (K)
T_o	Prescribed temperature on the boundary surface (K)
T_s	Unknown surface temperature (K)
$T_{s,\,1/2}$	Surface temperature, defined as the average of $T_{s,0}$ and $T_{s,1}$ (K)
T_w	Temperature of the wall surface (K)
u_i	Fluid velocity in the x_i direction (m/s)
U	Bulk velocity (m/s)
U_{atm}	Theoretical camera output voltage for a blackbody of temperature T_{atm} according to the calibration (V)
U_D	Overall heat transfer coefficient ($W/m^2/K$)
U_f	Thermal transmittance of the window frame ($W/m^2/K$)
U_g	Thermal transmittance of the glass ($W/m^2/K$)
U_{obj}	Calculated camera output voltage for a blackbody of temperature T_{obj} (V)
U_{refl}	Theoretical camera output voltage for a blackbody of temperature T_{refl} according to the calibration (V)
U_{tot}	Measured camera output voltage for the actual case (V)
U_{tr}	Thermal transmittance ($W/m^2/K$)
U_w	Thermal transmittance of the window ($W/m^2/K$)
U_{wall}	Thermal transmittance of the wall ($W/m^2/K$)
v	Air speed (m/s)
V	Domain volume

W_{atm}	Total energy depending on the presence of atmosphere
W_{refl}	Total energy depending on other sources standing around the measurement
W_{tot}	Total energy that hits the camera when the object to be analysed is focused
x	x coordinate
X_{α}	Volume fraction component
y	y coordinate
z	z coordinate

Greek symbols

α	Thermal diffusivity (m^2/s)
α_{surf}	Surface absorption coefficient
β	Thermal expansion (1/K)
δn	Normal grid spacing
ΔT	Temperature difference outdoor - indoor (K)
ΔT_{LM}	Logarithmic mean temperature difference (K)
Γ	Boundary surface
ε	Emissivity
μ	Dynamic viscosity (Pa x s)
ν	Kinematic viscosity (m^2/s)
ρ	Density (kg/m^3)
$\rho_{s,\alpha}$	Component density (kg/m^3)
σ	Stefan-Boltzmann constant equal to 5,669 x 10^{-8} [W/(m^2 x K^4)]
φ	Latitude (°)
φ_{R1}	Lower latitude if compared to φ (°)
φ_{R2}	Higher latitude if compared to φ (°)
Ψ_g	Linear thermal transmittance of the glass (W/m/K)

ABSTRACT

(Italian)

L'efficienza energetica occupa un posto di rilevante importanza nel complesso delle misure e delle azioni necessarie a rafforzare l'approvvigionamento energetico e contemporaneamente a ridurre le emissioni di gas climalteranti in atmosfera. Tale ruolo di spicco è stato ulteriormente sottolineato dai recenti documenti programmatici sia a livello comunitario sia all'interno della Strategia Energetica Nazionale. Se si considera che circa il 40% del consumo finale di energia negli Stati Membri è attribuibile direttamente al settore terziario e residenziale (case, uffici pubblici e privati, negozi e altre categorie di edifici), si evince immediatamente che il potenziale di risparmio in tale settore è estremamente elevato. In base all'analisi condotta dall'Energy Efficiency Report, realizzato dall'Energy & Strategy Group del Politecnico di Milano, gli interventi di miglioramento dell'efficienza energetica devono riguardare l'involucro edilizio, sia chiusure opache che trasparenti, la produzione e distribuzione di energia termica ed elettrica, ed i servizi generali (ad esempio illuminazione, aria compressa, refrigerazione).

L'attività di ricerca ha pertanto riguardato l'analisi dello scambio termico di alcune soluzioni energeticamente efficienti -attraverso il metodo degli elementi finiti e delle differenze finite- al fine di valutare l'effettivo miglioramento della scelta proposta. La tesi comprende:

- caso studio 1: utilizzo di uno scambiatore di calore geotermico per la fornitura di energia termica presso il Vivaio Daniel Plants (Viterbo);
- caso studio 2: analisi del comportamento termico di una superficie opaca in presenza ed assenza di cappotto esterno, in condizioni invernali ed estive, nella Caserma del Corpo Forestale dello Stato di Sabaudia (Latina);
- caso studio 3: utilizzo della termografia IR attiva nell'analisi del comportamento termico degli infissi, sia in fase di riscaldamento che di raffreddamento.

(English)

Energy efficiency is increasingly becoming a relevant issue both in the European and national regulations, which are aimed at reducing greenhouses gas emissions and to strengthen fossil fuels independence.

Since buildings of tertiary sector and residential structures account for approximately 40% of the total energy consumption, it is important to immediately act. According to the Energy Efficiency Report, the most effective interventions should involve opaque and transparent enclosures, thermal and electrical energy production and distribution, and general services (lighting, refrigeration).

Hence, the present Doctoral thesis is addressed to investigate the thermal behaviour of some energy-efficient solutions and to evaluate the improvement which may be reached. It concerns the use of the Finite Element and Finite Difference Methods in order to solve the differential equations describing the specific phenomenon. The following examples will be investigated:

- case study 1: use of a Downhole Heat Exchanger for heating in the Province of Viterbo;
- case study 2: thermal behaviour of the external opaque enclosures in a public building in Sabaudia (Latina), both in winter and summer conditions;
- case study 3: use of active IR thermography for glasses thermal behaviour, during the heating and cooling phases.

INTRODUCTION

1. Aims and motivation of the research

According to recent national and European regulations, ambitious targets need to be achieved by reducing greenhouses gases emissions, producing energy from renewable sources and improving the energy efficiency.

Since buildings account for approximately 40% of energy consumption in the European Union, their energy efficiency retrofitting is increasingly becoming a relevant environmental issue to still work on, both in industry and academic research. According to the Energy Efficiency Report published in 2013 by the Politecnico di Milano (Italy), the following technologies should be implemented to ensure energy efficiency: interventions on opaque enclosures and glasses, thermal energy production by means of renewable sources, use of the uninterruptible power supply in the electrical system and distribution, and building automation systems.

Thus, the aim of the present thesis is to investigate the thermal behaviour of some energy-efficient technologies and the improvement which may be reached with specific interventions. Since the solution of the heat transfer differential equations is required, the analysis will be carried out by means of two software products which are based on the Finite Element and Finite Difference Methods.

2. Structure of the thesis

The present Doctoral thesis consists of 4 chapters:

- Chapter 1 briefly describes the theoretical background of heat transfer, paying attention on basic principles and fundamental equations. After a short theory recall, an explanation of the numerical solutions of heat differential equations is given, namely Finite Element and Finite Difference Methods, which are implemented by the two software products I used, Comsol Multiphysics and Fire Dynamic Simulator respectively.
- Chapters 2, 3, and 4 describe three different case studies, according to this following structure: aim of the specific investigation,

introduction to the problem, materials and methods (distinguished in several sub-paragraphs describing the steps of the adopted methodology), results and discussion, and conclusion. In more detail, Chapter 2 involves the analysis of the thermal behaviour of a Downhole Heat Exchanger for heating in the Province of Viterbo. Chapter 3 concerns the thermal behaviour of the external opaque enclosures and thermal bridges in a public building in Sabaudia (Latina, Central Italy), with regard to winter and summer conditions. Chapter 4, which is the most extensive part and the core of the whole work, investigates the thermal behaviour of five glasses. This research was carried out in collaboration with the Polytechnic University of Valencia (Spain).

3. <u>Published papers during the PhD studies</u>

The present Doctoral thesis includes some of the papers published during my PhD studies, which are mentioned at the beginning of each case study (Chapters 2 and 3). However, other scientific articles were published in International Journals or as Conference Papers. Here is the full list of the manuscripts:

1. Boubaker K, de Franchi M, Colantoni A, MonarcaD, Cecchini M, Longo L, Allegrini E, Di Giacinto S, Biondi P, Menghini G. Prospective for hazelnut cultivation small energetic plants outcome in Turkey: Optimization and inspiration from an Italian model (2015) Renewable Energy, 74, pp. 523-527.

2. Carlini M, Allegrini E, Zilli D, Castellucci S. Simulating heat transfers through the building envelope: A useful tool in the economical assessment (2014) Energy Procedia, 45, pp. 395-404.

3. Carlini M, Castellucci S, Allegrini E, Giannone B, Ferrelli S, Quadraroli E, Marcantoni D, Saurini MT. Ceramic flaws: Laboratory tests and analysis using Scanning Electron Microscope to identify surface defects (2014) Journal of the European Ceramic Society, 34 (11), pp. 2655-2662.

4. Boubaker K, Colantoni A, Allegrini E, Longo L, Di Giacinto S, Monarca D, Cecchini M. A model for musculoskeletal disorder-related fatigue in upper limb manipulation during industrial vegetables sorting (2014) International Journal of Industrial Ergonomics, 44 (4), pp. 601-605.

5. Allegrini E, Cocchi S, Carlini M, Castellucci S. Economic feasibility of energy-efficient solutions: an Italian case study towards green engineering. 4^{TH} VALENCIA GLOBAL 2014, 19-20 June 2014, Valencia, Spain.

6. Carlini M, Castellucci S, Cocchi S, Allegrini E. Slaughterhouse wastes: A review on regulations and current technologies for biogas production (2014) Advanced Materials Research, 827, pp. 91-98.

7. Boubaker K, Colantoni A, Longo L, Menghini G, Baciotti B, Allegrini E, Cecchini M. Optimizing the energy conversion process: An application to a biomass gasifier-Stirling engine coupling system (2013) Applied Mathematical Sciences, 7 (137-140), pp. 6931-6944.

8. Carlini M, Castellucci S, Cocchi S, Allegrini E, Li M. Italian residential buildings: Economic assessments for biomass boilers plants (2013) Mathematical Problems in Engineering, 2013, art. no. 823851.

9. Cecchini M, Cossio F, Marucci A, Monarca D, Colantoni A, Petrelli M, Allegrini E. Survey on the status of enforcement of European directives on health and safety at work in some Italian farms (2013) Journal of Food, Agriculture and Environment, 11 (3-4), pp. 595-600.

10. Boubaker K, ColantoniA, Allegrini E, Longo L, Di Giacinto S, Biondi P. Short-Term perspectives for hybrid wind/solar/geothermal renewable energy (2013) International Journal of Renewable Energy Research, 3 (2), pp. 436-440.

11. Carlini M, Castellucci S, Allegrini E, Cocchi S. Heat transfers through the building envelope: a simulation for a private dwelling in Central Italy. 7th

International Image Processing & Wavelet on Real World Applications Conference IWW 2013, 5-6 September 2013, Valencia, Spain.

12. Colantoni A, Allegrini E, Boubaker K, Longo L, Di Giacinto S, Biondi P. New insights for renewable energy hybrid photovoltaic/wind installations in Tunisia through a mathematical model (2013) Energy Conversion and Management, 75, pp. 398-401.

13. Mosconi EM, Carlini M, Castellucci S, Allegrini E, Mizzelli L, Arezzo Di Trifiletti M. Economical assessment of large-scale photovoltaic plants: An Italian case study (2013) Lecture Notes in Computer Science (including subseries Lecture Notes in Artificial Intelligence and Lecture Notes in Bioinformatics), 7972 LNCS (PART 2), pp. 160-175.

14. Marucci A, Monarca D, Cecchini M, Colantoni A, Allegrini E, Cappuccini A. Use of semi-transparent photovoltaic films as shadowing systems in mediterranean greenhouses (2013) Lecture Notes in Computer Science (including subseries Lecture Notes in Artificial Intelligence and Lecture Notes in Bioinformatics), 7972 LNCS (PART 2), pp. 231-241.

15. Colantoni A, Allegrini E, Recanatesi F, Romagnoli M, Biondi P, Boubaker K. Mathematical analysis of gasification process using Boubaker polynomials expansion scheme (2013) Lecture Notes in Computer Science (including subseries Lecture Notes in Artificial Intelligence and Lecture Notes in Bioinformatics), 7972 LNCS (PART 2), pp. 288-298.

16. Petroselli A, Arcangeletti E, Allegrini E, Nunzio R, Grimaldi S. The influence of the net rainfall mixed Curve Number – Green Ampt procedure in flood hazard mapping: a case study in Central Italy, AIIA Conference, September 2013.

17. Carlini M, Castellucci S, Allegrini E, Tucci A. Down-hole heat exchangers: Modelling of a low-enthalpy geothermal system for district heating (2012) Mathematical Problems in Engineering, 2012, art. no. 845192.

CHAPTER 1
THEORETICAL BACKGROUND

1.1 Introduction

In order to describe natural phenomena, scientific computing encompasses a three-stage process: modelling of the problem by means of appropriate equations, computing the solution by an adequate software, and presenting the result generated by the software output [Pentenrieder, 2005].

According to this approach, the present chapter is aimed at describing the theoretical background of the scientific computing adopted in the research project. It briefly defines the different modes of heat transfer and the solution of the governing equations by means of the Finite Element Method (FEM) and Finite Difference Method (FDM). This is to better understand how the two software products I used implement and solve heat transfer equations. Then, attention will be focused on describing the software itself, namely Comsol Multiphysics and Fire Dynamic Simulator.

1.2 Modes of heat transfer

If a system interacts with the surroundings, energy can be transferred in terms of work and heat. Broadly speaking, heat transfer is meant as the thermal energy in transit due to a spatial difference of temperature or gradient: consequently, whenever a temperature difference exists, heat transfer occurs. By definition, heat flows from the higher to the lower level of temperature, without performing work [Pentenrieder, 2005; Incropera *et al.*, 2007].

To some extent, the amount of transferred heat (*flow*) is given by the multiplication of the transport coefficient by the potential gradient, where the former depends on the particular mode of heat transfer, while the second represents a derivative or some difference expression. The term *flow* may be related to heat flux -i.e. energy per time and area- or heat transfer rate -i.e. energy per time passing though a fixed reference area [Pentenrieder, 2005].

The modes of heat transfer processes can be distinguished as follows [Lewis *et al.*, 2004; Incropera *et al.*, 2007]:

- ✓ conduction, to refer the heat transfer occurring through the medium because of an exchange of energy from one molecule to another without the actual motion, or because of the motion of free electrons;
- ✓ convection, which occurs between a moving fluid and a surface at different temperatures. The transfer occurs from one region to another because of macroscopic motion in a liquid or gas. It may be free, forced or mixed;
- ✓ thermal radiation: all bodies emit thermal radiation at all temperature which propagates by means of electromagnetic waves from the body surface. When these waves strike other bodies, a part of the radiation is transmitted, a part is reflected, and the remaining part is absorbed.

A real physical problem presents all modes of heat transfer in different and varying degrees: in order to correctly solve heat transfer problems, the most significant mode needs to be identified, deciding whether one of the others may be neglected [Lewis *et al.*, 2004].

In heat transfer analysis, the amount of energy per unit time is a fundamental aspect and is given by the rate equations. For 1D heat conduction, the rate equation is expressed by *Fourier's Law* (Eq. 1.1). *Newton's Law* of cooling gives the rate equation for convective heat transfer (Eq. 1.2): the solution of heat conduction in solids often uses the convection heat transfer coefficient as a boundary condition. The maximum flux emitted by a radiating black surface is expressed by *Stefan-Boltzmann Law* (Eq. 1.3). Since a real surface emits less heat flux than that of a black surface, the radiative property -referred to as the emissivity of the material- is considered, as shown in Eq. 1.4 [Lewis *et al.*, 2004; Incropera *et al.*, 2007].

$$q_x = -k \cdot \frac{dT}{dx} \tag{1.1}$$

$$q_{conv} = h \cdot \left(T_w - T_f\right) \tag{1.2}$$

$$q_{rad} = \sigma \cdot T_w^{\ 4} \tag{1.3}$$

$$q_{rad} = \varepsilon \cdot \sigma \cdot T_w^{\ 4} \tag{1.4}$$

1.3 Conduction

The aim of a conduction analysis is to determine the temperature field in a medium resulting from conditions imposed on its boundaries: the temperature distribution is a function of space at steady state and as a function of time in transient conditions. Once it is known, the conduction heat flux at any point may be computed by Eq. 1.1 [Lewis *et al.*, 2004; Incropera *et al.*, 2007].

The conduction equation in Cartesian coordinates is derived by applying the energy conservation law to the differential control volume as shown in figure 1 (left). Thus, the transient heat conduction equation in anisotropic materials is expressed by:

$$\frac{\partial}{\partial x}\left(k_x \frac{\partial T}{\partial x}\right)+\frac{\partial}{\partial y}\left(k_y \frac{\partial T}{\partial y}\right)+\frac{\partial}{\partial z}\left(k_z \frac{\partial T}{\partial z}\right)+G=\rho c_p \frac{\partial T}{\partial t} \tag{1.5}$$

Eq. 1.5 is often referred to as the heat diffusion equation, provides the basic tool for heat conduction analysis, and describes an important physical condition, that is conservation energy. Its solution leads to determine the temperature distribution T(x, y, z) as a function of time. Hence, this equation states that at any point in the medium the net rate energy transfer due to conduction into a unit volume plus the volumetric rate of thermal energy generation must equal the rate of change of thermal energy stored within the volume. The heat diffusion equation may be also expressed both in cylindrical and spherical coordinates. Simplifications may be introduced in Eq. 1.5:

If thermal conductivity is constant, introducing the thermal diffusivity α=k/ρ x cp:	$$\frac{\partial^2 T}{\partial x^2}+\frac{\partial^2 T}{\partial y^2}+\frac{\partial^2 T}{\partial z^2}+\frac{G}{k}=\frac{1}{\alpha}\frac{\partial T}{\partial t} \quad (1.6)$$
Under state-steady and anisotropic conditions:	$$\frac{\partial}{\partial x}\left(k \frac{\partial T}{\partial x}\right)+\frac{\partial}{\partial y}\left(k \frac{\partial T}{\partial y}\right)+\frac{\partial}{\partial z}\left(k \frac{\partial T}{\partial z}\right)+G=0 \quad (1.7)$$
If the heat transfer is one-dimensional (e.g. in the x direction) and no energy generation occurs:	$$\frac{d}{dx}\left(k \frac{dT}{dx}\right)=0 \quad (1.8)$$

Table 1: Simplifications of the heat diffusion equation.

The solution of Eq. 1.5 depends on the physical conditions existing at the boundaries of the medium and on conditions existing in the medium at some initial time if the problem is time dependent. The boundary conditions for conduction equation can be distinguished into two common types, namely constant surface temperature and constant heat flux (figure 1, right). While the former is often referred to as Dirichlet condition, in which the temperature on the boundaries is known:

$$T = T_0 \ \ on \ \Gamma_T \tag{1.9}$$

in the latter condition, which is usually referred to as Neumann condition, the heat flux is imposed and is expressed as:

$$q = -k\frac{\partial T}{\partial n} = h \ \ on \ \Gamma_{qf} \tag{1.10}$$

If h is equal to zero, the insulated or adiabatic condition occurs. It should be noted that Eq. 1.5 has second-order terms and thus two boundary conditions are required. Moreover, since time appears as a first-order term, only one initial value is needed:

$$T = T_0 \ \ all\ over\ the\ domain\ \Omega\ at\ t = t_0 \tag{1.11}$$

The temperature is a scalar and makes easy to implement the constant or variable temperature conditions [Lewis *et al.*, 2004; Incropera *et al.*, 2007].

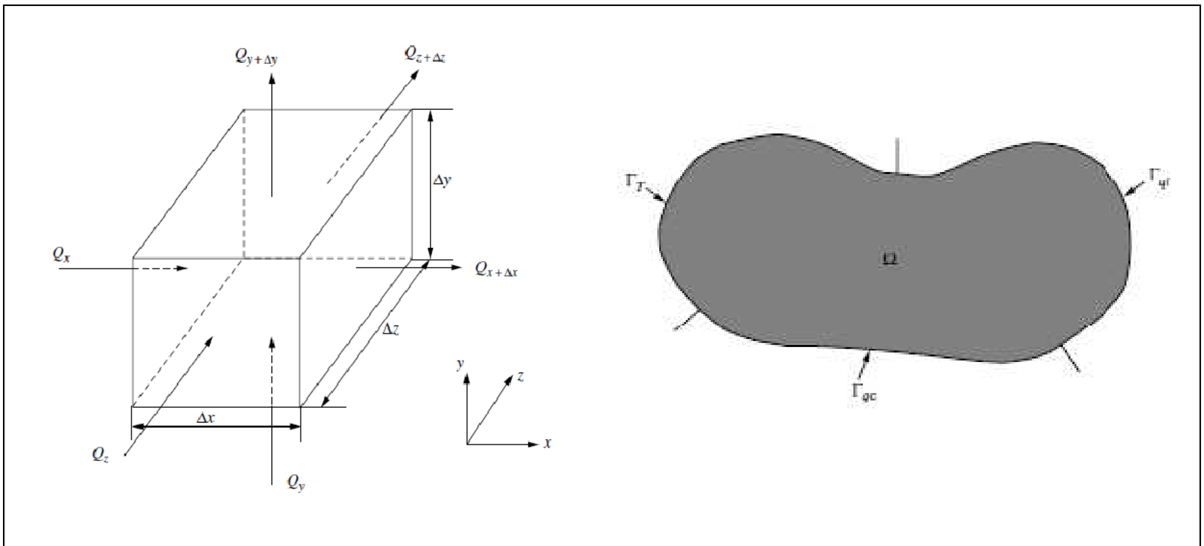

Figure 1: A differential control volume for heat conduction analysis (left); Boundary conditions (right) [Lewis *et al.*, 2004].

1.4 Convection

Convection can be divided into natural and forced convection: while in the former case, buoyancy force –induced by temperature differences and the thermal expansion of the fluid- drives the flow, the latter is created by an external force, for example a pump.

Flow with a higher inlet velocity will transport heat at higher rate: the flow rate is often described by a dimensionless parameter, called the Reynolds number. The Reynolds number represents the ratio of the inertia to viscous force: if it is small, inertia forces are insignificant relative to viscous forces. The disturbances are then dissipated and the flow remains laminar. For higher values and above its critical value, the inertia forces can be sufficient to amply the triggering mechanism so that a transition to turbulence occurs [Lewis *et al.*, 2004; Incropera *et al.*, 2007; Comsol Multiphysics, 2013].

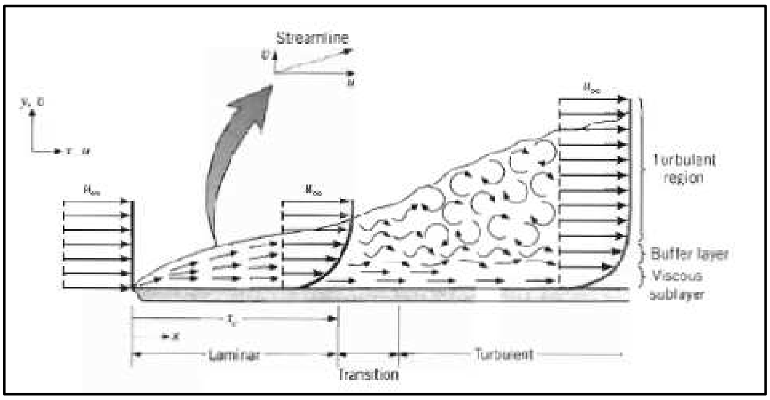

Figure 2: Laminar and turbulent flow [Comsol Multiphysics, 2013].

The mathematical model is governed by the Navier-Stokes equations, which conserve mass, momentum, and energy, as it is shown in the indicial forms of Eq. 1.12, 1.13, and 1.14 [Lewis *et al.*, 2004]:

$$\frac{\partial \rho}{\partial t} + \frac{\partial(\rho u_i)}{\partial x_i} = 0 \tag{1.12}$$

$$\rho\left(\frac{\partial u_i}{\partial t} + u_j \frac{\partial u_i}{\partial x_j}\right) = -\frac{\partial p}{\partial x_i} + \mu\left(\frac{\partial^2 u_i}{\partial x_i^2}\right) \tag{1.13}$$

$$\frac{\partial T}{\partial t} + u_i \frac{\partial T}{\partial x_i} = \alpha\left(\frac{\partial^2 T}{\partial x_i^2}\right) \tag{1.14}$$

In many heat transfer applications, data may be generated by non-dimensionalizing the Eq. 1.12, 1.13, and 1.14 using appropriate non-dimensional scales. These equations depend on the following dimensionless parameters [Lewis *et al.*, 2004; Incropera *et al.*, 2007; Comsol Multiphysics, 2013].

$$\mathrm{Re} = \frac{\rho \cdot U \cdot L}{\mu} \tag{1.15}$$

$$\mathrm{Pr} = \frac{\mu \cdot c_p}{k} \tag{1.16}$$

$$Gr = \frac{g \cdot \beta \cdot (T_s - T_\infty) \cdot L^3}{\nu^2} \tag{1.17}$$

$$Ra = Gr \cdot \mathrm{Pr} = \frac{g \cdot \beta \cdot (T_s - T_\infty) \cdot L^3}{\nu \alpha} \tag{1.18}$$

1.5 Thermal radiation

Thermal radiation is associated with the rate at which energy is emitted by matter due to its finite temperature. As a matter of fact, at this moment it is being emitted by all the surrounding matter, such as the furniture and walls of the room for indoor conditions or by the ground, buildings, and the atmosphere and sun if you are outside [Incropera *et al.*, 2007].

The mechanism of emission is related to energy released as a result of oscillations or transitions of the electrons that constitute matter and can be seen as a surface phenomenon. The spectral distribution varies with the nature and temperature of the emitting surface. In addition to the spectral nature, directionality is the second feature to consider: a surface may emit preferentially in certain directions, creating a directional distribution of the emitted radiation.

Since radiation that leaves a surface can propagate in all possible directions, radiation incident upon a surface may come from different directions, and the manner in which the surface responds depends on the direction. Such effect can be important in determining the net radiative heat transfer rate and may be treated by introducing the concept of radiation intensity [Incropera *et al.*, 2007].

For a spectral component of the irradiation, portions of this radiation may be reflected, absorbed and transmitted, and from a radiation balance on the medium, it follows that:

$$G_{\lambda} = G_{\lambda,ref} + G_{\lambda,abs} + G_{\lambda,tr} \tag{1.19}$$

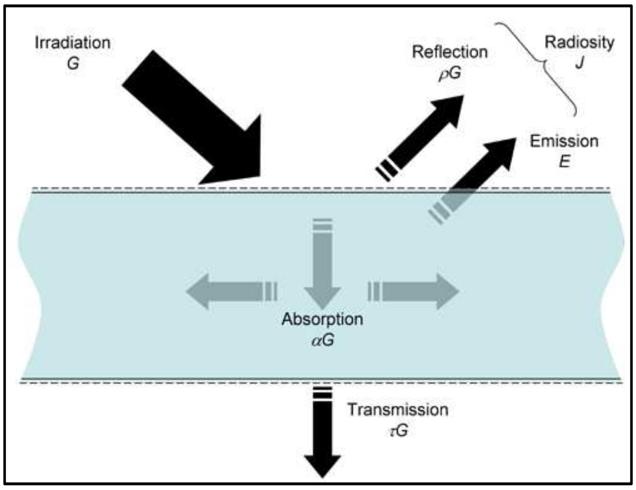

Figure 3: Absorption, reflection and transmission processes associated with a semitransparent medium [Comsol Multiphysics, 2013].

Usually, the calculation of these components is complex, depending on the upper and lower surface conditions, the wavelength of the radiation, and the composition and thickness of the medium. Since in most engineering applications the medium is opaque, $G_{\lambda.tr}$ is equal to zero. The absorption and reflection processes may be treated as surface phenomena and it is interesting to note that they are responsible of our perception of colour.

The absorptivity determines the fraction of the irradiation absorbed by a surface. The reflectivity is a property that determines the fraction of the incident radiation reflected by a surface. It depends on the direction of the incident and reflected radiation [Incropera *et al.*, 2007; Comsol Multiphysics, 2013].

1.6 Solution of heat transfer equations: FEM and FDM

Since analytical solutions to many heat transfer problems are not often possible because of the geometry or boundary conditions complexity, a numerical solution is required in such situations. The Finite Element (FEM), Finite Difference (FDM) and Finite Volume Method (FVM) are the most commonly employed numerical techniques [Lewis *et al.*, 2004; Nikishov, 2004].

While an analytical solution leads to the temperature determination at any point of the medium, a numerical solution is referred to discrete points in which the temperature distribution is given. As a consequence, the first step is represented by selecting these points simply dividing the region of interest into a number of smaller sub-regions [Lewis *et al.*, 2004].

The FEM is a numerical tool for calculating approximate solutions of many engineering problems. According to this approach, the solution region encompasses many small and interconnected elements and gives a piece-wise approximation to the governing equations. Therefore, the complex Partial Differential Equations (PDEs) are reduced to either linear or nonlinear simultaneous equations. Thank to the finite element discretization , the continuum problem, having an infinite number of unknowns, is reduced to one with a finite number of unknowns at specified points, called nodes [Hughes 2000; Zienkiewicz and Taylor, 2000; Lewis *et al.*, 2004].

According to the FEM technique, the solution of a continuum problem is approximated by the following step-by-step procedure, as shown in figure 4 [Lewis *et al.*, 2004]:

- discretization of the continuum: divide the solution region into non-overlapping elements. A variety of elements shape -e.g. triangles or quadrilaterals- is allowed;
- selection of the shape functions: it is to choose the type of interpolation that represents the variation of the field variable over the element;
- formulation of the element equations: this step creates the matrix equations which express the properties of the individual elements by forming a Left Hand Side (LHS) matrix and a load vector:

$$[K]_e = \frac{Ak}{l}\begin{bmatrix} 1 & -1 \\ -1 & 1 \end{bmatrix} \tag{1.20}$$

$$\{f\}_e = \begin{Bmatrix} Q_i \\ Q_j \end{Bmatrix} \tag{1.21}$$

- assembling the element equations to obtain a system of simultaneous equations: this is to obtain a resulting matrix which represents the behaviour of the entire solution region of the problem:

$$[K]\{T\} = \{f\} \tag{1.22}$$

- solving the system of equations: Eq. 1.22 may be solved to obtain the nodes values of the field variable, for example temperature;
- calculation of the secondary quantities from the nodal values, such as the space heat flux.

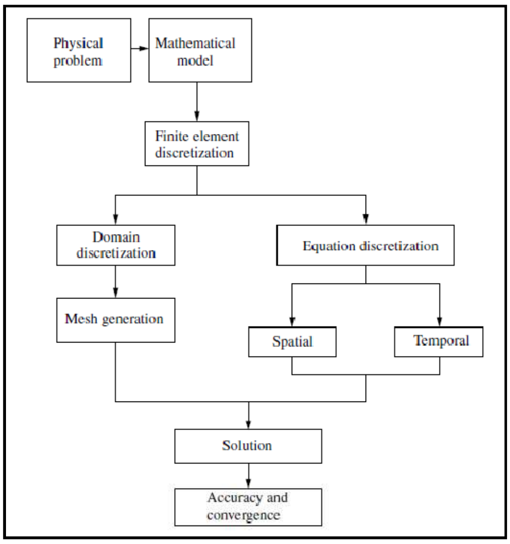

Figure 4: Numerical model for heat transfer calculations [Lewis *et al.*, 2004].

The physical formulation can be transformed into its finite element discrete analogue by following several approaches. If the former is a Partial Differential Equation, the Galerkin method is chosen, as in the present research project. According to this technique, the domain is divided into finite elements connected at nodes and shape functions N_i are introduced for interpolating the temperature inside a finite element:

$$T = [N]\{T\} \tag{1.23}$$

$$[N] = [N_1 \;\; N_2 \; ...] \tag{1.24}$$

$$\{T\} = \{T_1 \;\; T_2 \; ...\} \tag{1.25}$$

By differentiating the temperature interpolation equation given by (1.23), it follows:

$$\begin{Bmatrix} \partial T / \partial x \\ \partial T / \partial y \\ \partial T / \partial z \end{Bmatrix} = \begin{Bmatrix} \partial N_1 / \partial x & \partial N_2 / \partial x... \\ \partial N_1 / \partial y & \partial N_2 / \partial y... \\ \partial N_1 / \partial z & \partial N_2 / \partial z... \end{Bmatrix} \{T\} = [B]\{T\} \tag{1.26}$$

Thus, using the Galerkin method and considering Eq. 1.1, Eq. 1.5 can be written as:

$$\int_V \left(\frac{\partial q_x}{\partial x} + \frac{\partial q_y}{\partial y} + \frac{\partial q_z}{\partial z} - G + \rho c_p \frac{\partial T}{\partial \tau} \right) N_i dV = 0 \tag{1.27}$$

Applying the divergence method to the first three terms in Eq. 1.27 and inserting the boundary conditions, the discretized finite element equations for heat transfer problems in an isotropic body is given by [Nikishov, 2004]:

$$[C]\{\dot{T}\} + ([K_c] + [K_h] + [K_r])\{T\} = \{R_T\} + \{R_Q\} + \{R_q\} + \{R_h\} + \{R_r\} \tag{1.28}$$

where:

$$[C] = \int_V \rho c_p [N]^T [N] dV \tag{1.29}$$

$$[K_c] = \int_V k [B]^T [B] dV \tag{1.30}$$

$$[K_h] = \int_{S3} h [B]^T [B] dV \tag{1.31}$$

$$[K_r]\{T\} = \int_{S4} \sigma \varepsilon T^4 [N] dS \tag{1.32}$$

$$[R_T] = -\int_{S1} \{q\}^T \{n\} [N]^T dS \tag{1.33}$$

$$[R_Q] = -\int_V Q [N]^T dV \tag{1.34}$$

$$[R_q] = -\int_{S2} q_s [N]^T dS \tag{1.35}$$

$$[R_h] = -\int_{S3} h T_e [N]^T dS \tag{1.36}$$

$$[R_r] = -\int_{S4} \alpha_{surf} q_r [N]^T dS \tag{1.37}$$

In order to solve partial differential equations of heat transfer, the software Comsol Multiphysics implements FEM.

The FDM is based on replacing differential equations by algebraic equations, where derivatives are substituted by differences. According to this approach, problems can be distinguished into explicit or implicit methods. While the former yields the temperature at a given time level directly from the previously computed values, the latter solves a simultaneous system of algebraic equations at each time step. The explicit technique provides a simple and effective algorithm, although stability constraints impose a maximum limit on the length of time steps (Wang, 1995; Agarwal, 2010).

If the calculations are performed over a large period of time, a high number of steps is required. The implicit method has no restriction on the size of the time step and this goal is successfully reached by the so called Crank-Nicholson approach. This scheme is a combination of the forward Euler method at n and the backward Euler method at (n+1) (Özisik, 1994). The software Fire Dynamic Simulator is based on this approach, updating the temperature at the centre of each solid cell $T_{s,i}$ in time. The discretization indexing system is shown in figure 5.

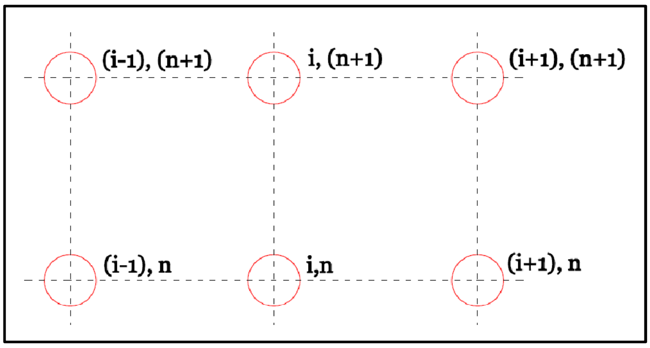

Figure 5: Crank-Nicolson's discretization scheme.

Hence the terms in Eq. 1.5 becomes:

$$(\rho_s \cdot c_s)\frac{\partial T_s}{\partial t} = (\rho_s \cdot c_s)_i \cdot \frac{T_{s,i}^{n+1} - T_{s,i}^{n}}{\delta t} \tag{1.38}$$

$$\frac{\partial}{\partial x}\left(k_s \frac{\partial T_s}{\partial x}\right) = \frac{1}{2\delta x^2}\left\{ \begin{aligned} &\left[k_{s,i+1/2}\cdot\left(T_{s,i+1}^{n} - T_{s,i}^{n}\right) - k_{s,i-1/2}\cdot\left(T_{s,i}^{n} - T_{s,i-1}^{n}\right)\right] + \\ &+\left[k_{s,i+1/2}\cdot\left(T_{s,i+1}^{n+1} - T_{s,i}^{n+1}\right) - k_{s,i-1/2}\cdot\left(T_{s,i}^{n+1} - T_{s,i-1}^{n+1}\right)\right] \end{aligned} \right\} \tag{1.39}$$

The temperatures at the front and back surface are determined from the boundary conditions. The boundary conditions at the front surface are given by:

$$-k_{s,1}\frac{T_{s,1}^{\ n+1} - T_{s,0}^{\ n+1}}{\delta x^2} = q_{conv} + q_{rad} \tag{1.40}$$

The convective heat flux is calculated as:

$$q_{conv} = \mathrm{h}\left[\mathrm{T_g} - \frac{1}{2}\left(T^{n}_{s,1/2} + T^{n+1}_{s,1/2}\right)\right] \tag{1.41}$$

The radiative heat flux is expressed by:

$$q_{rad} = q_{rad,IN} - \varepsilon\sigma\left(\mathrm{T}^{n+1}_{s,1/2}\right)^4 \tag{1.42}$$

Introducing Taylor series expansion for Eq. (1.42), the front boundary condition becomes:

$$-k_{s,1}\frac{T_{s,1}{}^{n+1} - T_{s,0}{}^{n+1}}{\delta x^2} \approx$$
$$\mathrm{h}\left[\mathrm{T_g} - \frac{1}{2}\left(T^{n}_{s,1/2} + T^{n+1}_{s,1/2}\right)\right] + q_{rad,IN} - 4\varepsilon\sigma\left(T_{s,1/2}{}^{n}\right)^3 \cdot T_{s,1/2}{}^{n+1} + 3\varepsilon\sigma\left(T_{s,1/2}{}^{n}\right)^4 \tag{1.43}$$

Similar considerations occur for the back boundary conditions [McGrattan *et al.*, 2013].

1.6.1 Comsol Multiphysics

1.6.1.1 General description

Comsol Multiphysics is a powerful interactive environment for modelling and solving a huge variety of scientific and engineering problems, extending conventional models for one type of physics into multiphysics models that solve coupled physics phenomena simultaneously. When solving the models, the software runs the finite element analysis together with adaptive meshing (if selected) and error control using a variety of numerical solvers [Comsol Multiphysics, 2013].

The Comsol Multiphysics environment is completely controlled by the Comsol Desktop, consisting of the Model Builder, node settings, Graphics windows, and other dockable windows. They can be opened, closed, and placed according to the modelling settings you need to access and the Graphical User Interface (GUI) configuration you want to work in. At the top of every window is the main menu and toolbar, which has a drop down menu and standard buttons for frequently used actions. At the right bottom corner of the Desktop is the Messages, Progress and Numerical results window (figure 6) [Comsol Multiphysics, 2013].

When COMSOL Multiphysics is first opened, or when you start creating a new model, the GUI displays the Model Builder, Model Wizard, and Graphics windows (figure 7). The modelling procedure is controlled by the following steps: geometry or drawing phase, selection of the physics, meshing, solving, and postprocessing (figure 8).

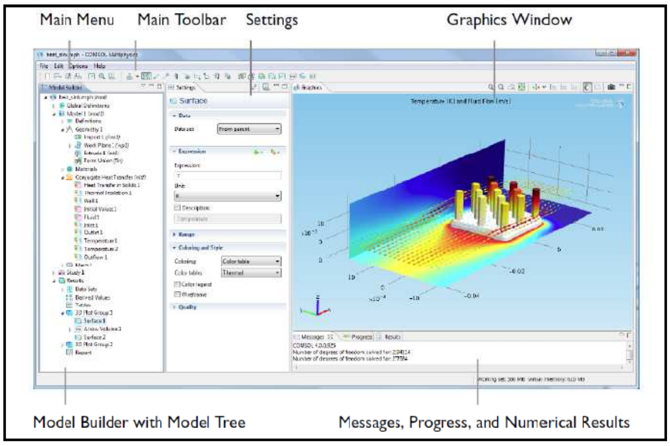

Figure 6: The Comsol Desktop with its major windows in a widescreen layout [Comsol Multiphysics, 2013].

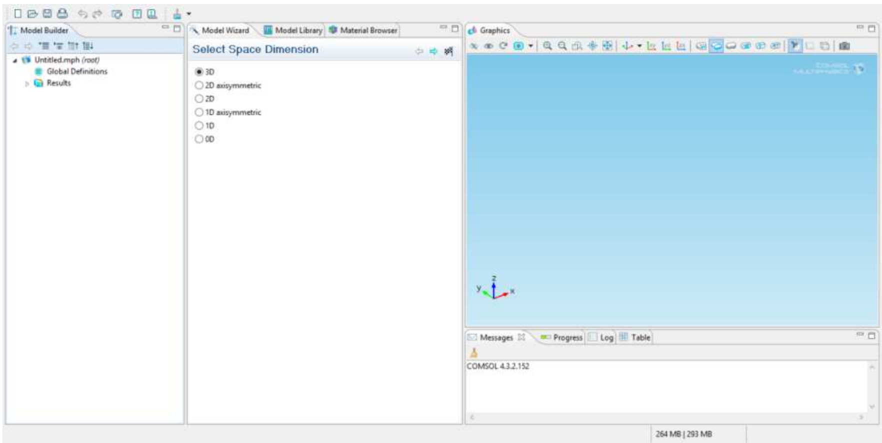

Figure 7: Model Builder, Model Wizard, and Graphics window when launching the software.

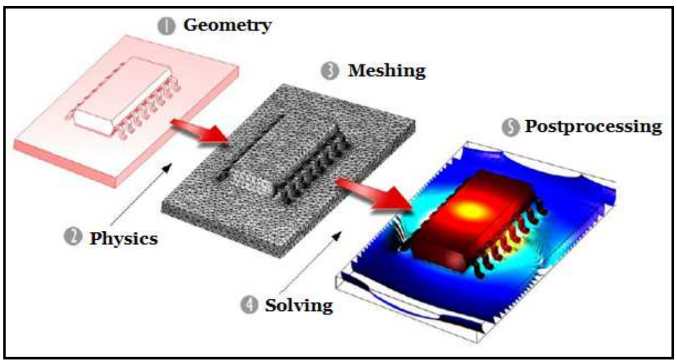

Figure 8: Modelling sequences in Comsol Multiphysics [Comsol Multiphysics, 2013].

The Model Wizard window contains a series of pages to help the user in starting to build a model (figure 9) [Comsol Multiphysics, 2013]:

- Select Space Dimension, namely 3D, 2D axisymmetric, 2D, 1D axisymmetric, 1D, or 0D. 0D is used for physics interfaces modelling spatially homogeneous systems such as chemical reacting systems and electrical circuits;
- Select Physics, e.g. heat transfer in solids;
- Select Study Type depending on the set of physics and mathematics interfaces included in the model. The user can select the study type from one of the following branches:
    - ✓ Preset Studies for Selected Physics: the study types applicable to all of the interfaces which you have chosen to solve for (Stationary, Time Dependent, Eigenfrequency, Eigenvalue and Frequency Domain);
    - ✓ Custom Studies: this branch contains study types for which not all physics solved for can generate suitable equations.

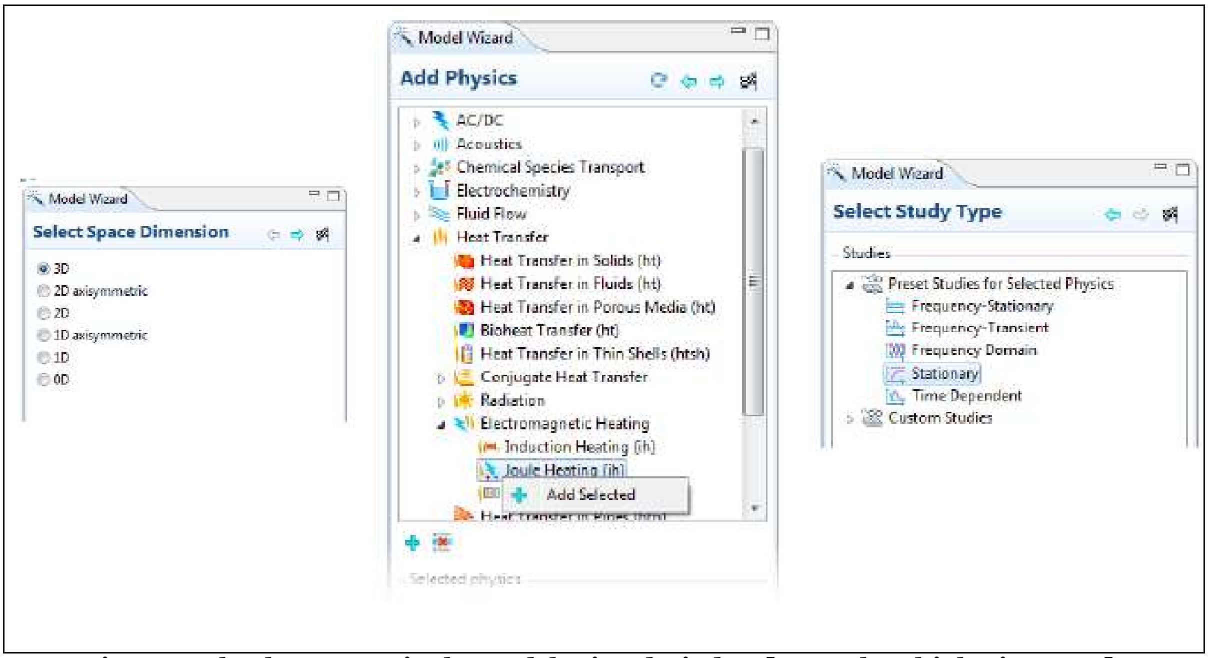

Figure 9: The three pages in the Model Wizard window [Comsol Multiphysics, 2013].

The Model Builder window includes a model tree with all the functionality and operations for building and solving models and displaying the results. These are introduced to your modelling procedure by adding a branch, such as the

Geometry branch. Branches can have further nodes that relate to their parent node. A leaf is considered to be the final node in a branching structure (tree) and usually has a number of attributes with their own settings that are characteristic to it. Branches and sub-branches can also contain attributes and settings.

The user can proceed through the Model Builder by selecting the branches in the order suggested by their default positions, from the top down, or selecting and defining each branch as needed. The main branches include Global Definitions, Model, Study, and Result (figure 10).

The Global Definitions branch collects parameters, variables, and functions accessible at all levels in the Model Builder.

The Model branch encompasses Definitions (D), Geometry (G), Materials (Ma), the selected Physics (P), and Mesh (Me). The D branch (one per Model) collects the definitions of variables, functions, and other objects whose geometric scope is restricted to a single model. The G branch is the drawing phase where the user can build the chosen geometry in the Model Wizard by using geometrical operations or importing CAD data. The Ma branch is where all the material properties are given: the Material Browser, namely a database, is available for rapidly adding a material. The P branch is the selected physics in the Model Wizard, containing the governing equations of the phenomenon and the required boundary conditions for solving the problem (figure 11). The Me branch contains the sequence of operations that defines the computational meshes for the model, and enables the discretization of the geometry model into small units of simple shapes, referred to as mesh elements (triangles, quadrilaterals, or tetrahedral, hexahedral, prism, or pyramid mesh elements).

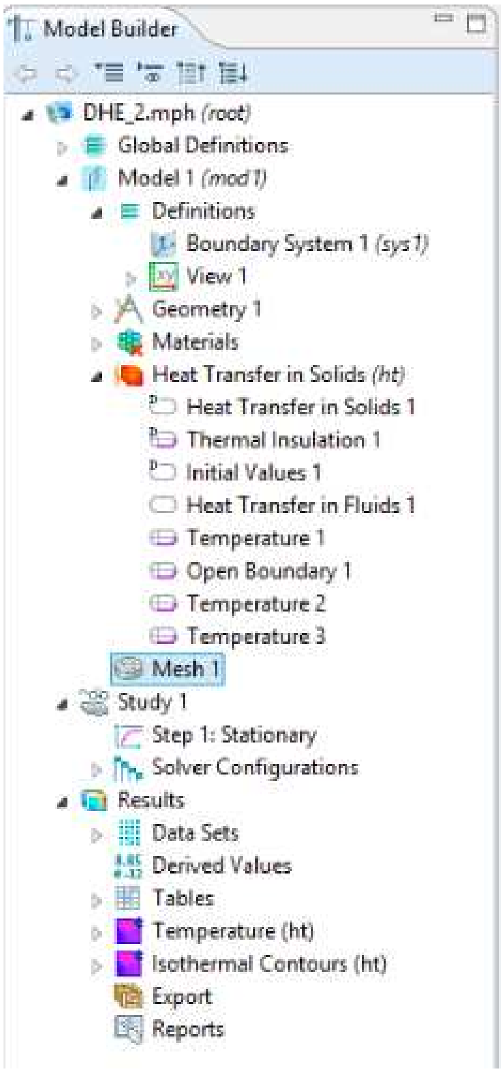

Figure 10: The Model Builder branches and sub-branches [Comsol Multiphysics, 2013].

The Study branch is where the user can set up study steps and solver configurations for solving a model using one or more study types for different analyses.

The Results branch is for presenting and analysing the results [Comsol Multiphysics, 2013].

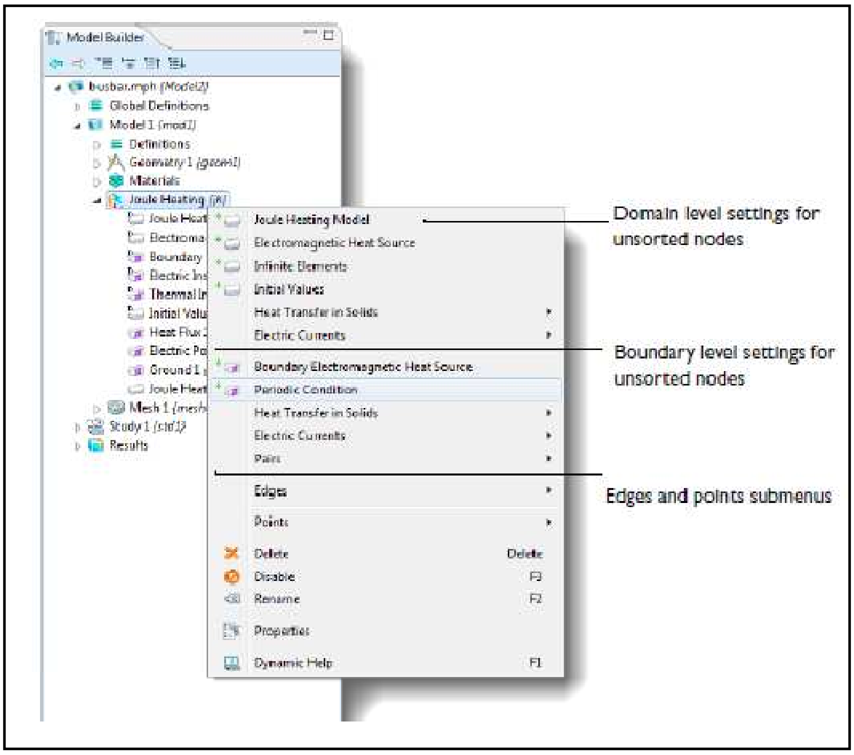

Figure 11: Boundary conditions [Comsol Multiphysics, 2013].

The Graphics window presents a graphical view of the geometry, mesh, and results of the model. Furthermore, it has useful tools for changing the view and selecting multiple entities—geometry objects as well as domains, boundaries, edges, and points for defining the physics or selecting geometric entities.

The Graphics toolbar at the top of the Graphics window contains a set of tools for changing the visualization (for example, to zoom in or out or to add transparency) and making selections.

Plot windows are closable graphics windows. They are automatically generated for displaying results while solving. The Messages window contains information useful to the user after an operation is performed, namely the number of mesh elements and degrees of freedom in your model. The Progress window displays the progress of the solver or mesher during the process, including a progress bar and progress information for each solver or mesher. The Log window contains information from previous solver runs. A horizontal divider (==============) indicates the start of a new solver progress log. To differentiate logs from different models, the log contains a horizontal divider displaying the name of the Model MPH-file each time a model is opened (figure 12) [Comsol Multiphysics, 2013].

There are three COMSOL Multiphysics model file formats: MPH-files, Model Java-files, and Model M-files. The default standard file with the extension .mph, containing contains both binary and text data. The mesh and solution data are stored as binary data, while all other information is stored as plain text. All the models in the COMSOL Multiphysics Model Library and the model libraries in the add-on modules are MPH-files. Model M-files are editable script files, similar to the Model Java-files, for use with MATLAB) [Comsol Multiphysics, 2013].

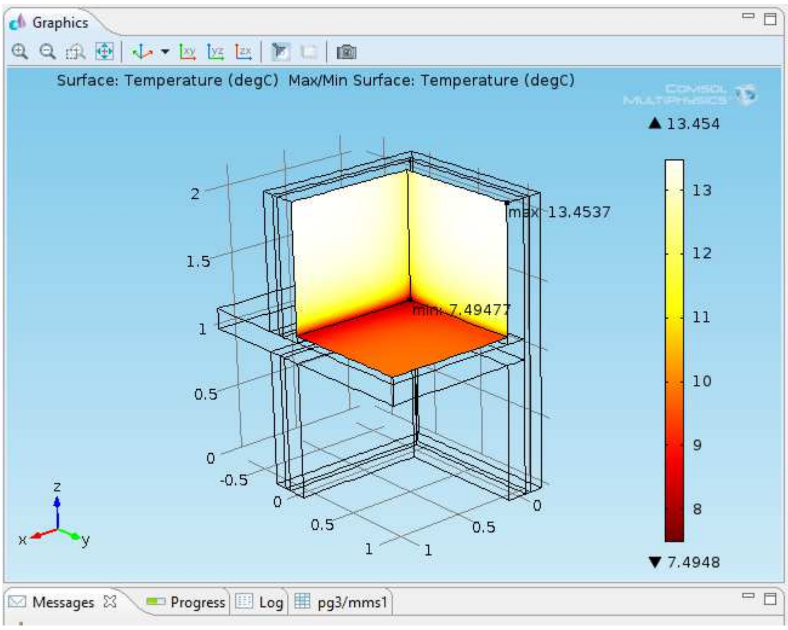

Figure 12: Graphics, Messages, Progress, and Log window.

Several add-on products are available for COMSOL Multiphysics, as it is shown in figure 13. The present research investigates the use of the Heat Transfer module. The Heat Transfer interfaces model heat transfer by conduction and convection. Surface-to-ambient radiation effects around edges and boundaries can also be included. The interfaces are suitable for modelling heat transfer in solids and fluids. The interfaces are available in 1D, 2D, and 3D and for axisymmetric models with cylindrical coordinates in 1D and 2D. The default dependent variable is the temperature, T [Comsol Multiphysics, 2013].

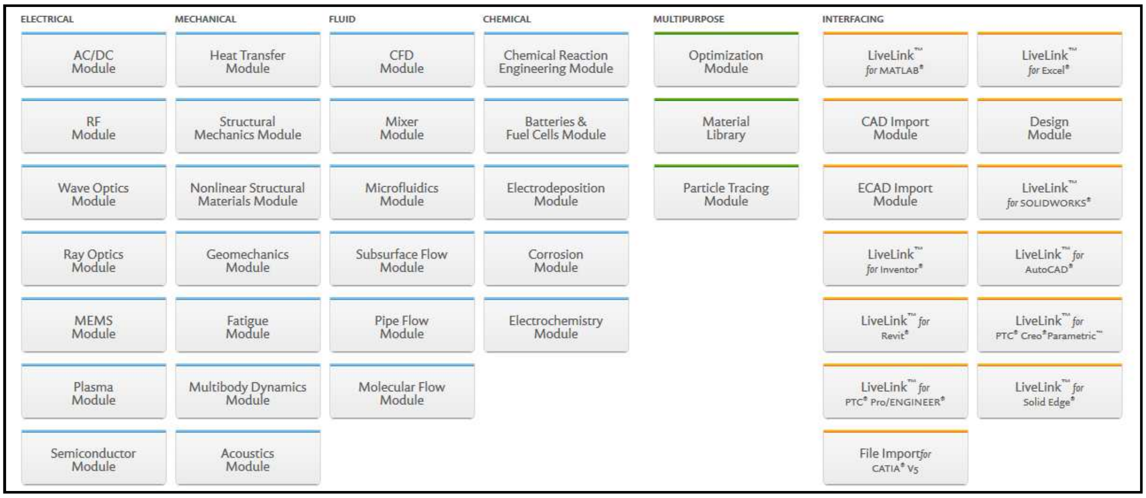

Figure 13: Suitable modules in Comsol Multiphysics [Comsol Multiphysics, 2013].

1.6.2 Fire Dynamic Simulator

1.6.2.1 General description

Fire Dynamic Simulator (FDS) is a computational fluid dynamics (CFD) modelling software for describing fire-driven fluid flows. FDS numerically solves a form of the Navier-Stokes equations appropriate for low-speed, that is Ma<0, 3, thermally-driven flow emphasising the presence of smoke and heat transport. The software has been validated and verified. Smokeview is a separate visualization program that is used to display the results of an FDS simulation [McGrattan *et al.*, 2013].

FDS and Smokeview are free and open-source software tools provided by the National Institute of Standards and Technology (NIST) of the United States Department of Commerce. Furthermore, this software is not subject to copyright protection and is in the public domain [McGrattan *et al.*, 2013].

Since it is a Fortran program, the software reads input parameters from a text file and writes user-specified output data to files. FDS approximates the governing equations on a rectilinear mesh: all the rectangular obstructions are required to conform to the underlying mesh. All solid surfaces have thermal boundary conditions and heat and mass transfer to and from solid surfaces is usually handled by empirical correlations [McGrattan *et al.*, 2013].

The work described in chapter 4 is based on the use of FDS 6, which was released in 2013.

1.6.2.2 Boundary conditions in FDS

In FDS the solid surfaces are considered as multiple layers of multiple material components: heat conduction is assumed to occur normally to the surface. The boundary condition on the front surface of a solid obstruction is given by:

$$k_s \frac{\partial T_s}{\partial x}(0,t) = q_{conv} + q_{rad} \tag{1.44}$$

If the radiation is assumed to penetrate in depth, the surface radiation term is set to zero.

On the back surface, there are two possible boundary conditions: if the back surface is assumed to be open to an ambient void or to another part of the computational domain, the back side boundary is similar to that of the front side; or if the back side is assumed to be perfectly insulated, an adiabatic condition is used [McGrattan *et al*, 2013]:

$$-k_s \frac{\partial T_s}{\partial x} = 0 \tag{1.45}$$

If the thermal radiation from the surroundings is assumed to be absorbed within an infinitely thin layer at the surface of the solid obstruction, the net radiative heat flux is given by the sum of incoming and outgoing components:

$$q_{rad} = q_{rad,\mathrm{IN}} - q_{rad,OUT} \tag{1.46}$$

where $q_{rad,IN}$ depends on the intensity of the wall and its emissivity and $q_{rad,OUT}$ is calculated according to Stefan-Boltzmann's law. In this formulation, the surface emissivity and the internal absorption are assumed to be constant.

The calculation of the convective heat flux depends on whether a Direct Numerical Simulation (DNS) or a Large Eddy Simulation (LES) is chosen. In the former, it is obtained directly from the gas temperature gradient at the boundary:

$$q_{conv} = -k\frac{\partial T}{\partial n} = -k\frac{T_w - T_g}{\delta n/2} \tag{1.47}$$

In an LES calculation, the convective heat flux takes into account the convective heat transfer coefficient, which is based on a combination of natural and forced convection correlations:

$$q_{conv} = h\left(T_g - T_w\right) \tag{1.48}$$

where h is given by:

$$h = \max\left[C\,|T_g - T_w|^{1/3}, \frac{k}{L} \cdot Nu \right] \tag{1.49}$$

The thermal conductivity and volumetric heat capacity of a solid are defined as follows:

$$k_s = \sum_{\alpha=1}^{N_m} X_\alpha k_{s,\alpha} \tag{1.50}$$

$$\rho_s c_s = \sum_{\alpha=1}^{N_m} \rho_{s,\alpha} c_{s,\alpha} \tag{1.51}$$

1.6.2.3 Procedure to run an FDS calculation

FDS can be run from the command prompt on a single or multiple computers (figure 14). Input files are typically given names in order to easily identify the particular case, followed by the suffix .fds. The operation of FDS is based on a single ASCII (American Standard Code for Information Interchange) text file, which contains parameters organize into namelist groups. The latter consists of a Fortran input record. Parameters are specified within an input file by using namelist formatted records, beginning with the ampersand character & followed by the name of the namelist group, a coma-delimited list of input parameters, and a forward slash / [McGrattan *et al.*, 2013].

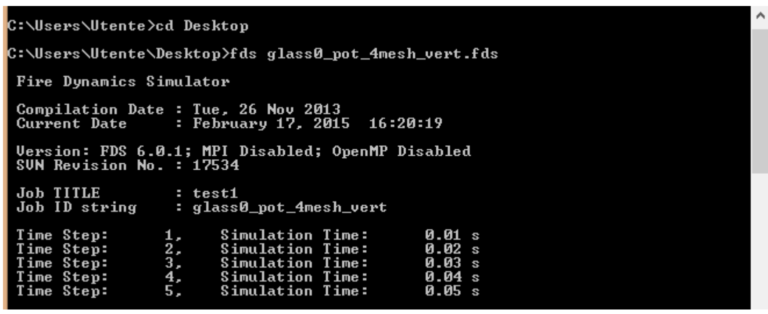

Figure 14: Command prompt to run an FDS simulation.

FDS reads the entire input file which is between:

$$\begin{aligned} &\&HEAD\ CHID = job\_name/ \\ &\&TAIL/ \end{aligned} \tag{1.52}$$

When writing an input file, a general rule is to add parameters which differ from the default value: this is a good way to easily distinguish what you want and FDS wants. Moreover, when setting up an input file, the first thing to do is to give the project a name. The namelist group HEAD encompasses such information by means of two parameters as shown in the example below:

$$\& HEAD\ CHID = 'WTC\_05',\ TITLE = 'TEST\_01'/ \tag{1.53}$$

CHID is a string of 30 characters as maximum number and is used to tag the output files. TITLE is a string containing the maximum number of 60 characters and is simply a brief descriptive text [McGrattan *et al.*, 2013].

TIME is the name of a group of parameters, defining the time duration of the simulation and the initial time step used to advance the solution of the discretized equations. The simulation time is set by the parameter T_END, which is equal to 1 second by default. If we want to instruct FDS to run a simulation for 5400 seconds, the following line is required:

$$\& TIME\ T\_END = 5400\ / \tag{1.54}$$

Moreover, if the time line to start is a number other than zero, the parameter T_BEGIN can be used in order to specify the time written to file for the first time step. This is useful for matching time lines coming from experimental data or video recordings [McGrattan *et al.*, 2013].

A domain is required in order to perform an FDS calculation: this goal is achieved by creating meshes. A mesh is divided into rectangular cells, whose number depends on the desired resolution of the flow dynamics. The computational domain is defined by the namelist MESH. The origin point of a mesh is defined the first, third and fifth values of the real number sextuplet, XB, while the second, fourth and sixth values refer to the opposite corner. An example is given below:

$$\& MESH\quad IJK = 10, 20, 30,\ XB = 0.0, 1.0, 0.0, 2.0, 0.0, 3.0\ / \tag{1.55}$$

The line defines a mesh whose volume extends from the origin (0, 0, 0) up to 1 m in the positive x direction, 2 m in the positive y direction, and 3 m in the positive z direction. The parameter IJK subdivides the mesh into uniform cells: in the present examples, it is made of 10 cm-cubes. Broadly speaking, mesh cells should resemble cubes, that is their length, width, and height ought to be roughly the same. Moreover, if obstructions or vents extend beyond the mesh boundary, they will be cut off at the boundary and will not appear in Smokeview [McGrattan *et al.*, 2013].

The second and third dimensions of the mesh, J and K, should be of the form $2^l\, 3^m\, 5^n$, where l, m, and n are integers, since part of the calculation uses a Poisson solver based on Fast Fourier Transforms (FFTs). This requirement is not needed for the first number of mesh cell divisions, i.e. the I in the IJK, because it does not use FFTs. Figure 15 shows list of numbers between 1 and 1024 which can be factored down to 2's, 3's and 5's [McGrattan *et al.*, 2013]:

2	3	4	5	6	8	9	10	12	15	16	18	20	24	25
27	30	32	36	40	45	48	50	54	60	64	72	75	80	81
90	96	100	108	120	125	128	135	144	150	160	162	180	192	200
216	225	240	243	250	256	270	288	300	320	324	360	375	384	400
405	432	450	480	486	500	512	540	576	600	625	640	648	675	720
729	750	768	800	810	864	900	960	972	1000	1024				

Figure 15: List of numbers that can be factored down to 2's, 3's and 5's [McGrattan *et al.*, 2013].

MISC is the namelist group of global miscellaneous input parameters. Only one MISC line should be entered in the data file. The MISC parameters vary in scope and importance. An example is given by the following line:

$$\&\ MISC\quad TMPA = 25\,/ \tag{1.56}$$

which sets the ambient temperature within the computational domain at 25°C (by default it is equal to 20°C) [McGrattan *et al.*, 2013].

An FDS simulation usually begins at time t = 0 with ambient conditions: the air temperature is assumed to be constant with height, and its density and pressure decrease with height (z direction). If the user wants to modify the local initial temperature, the following line can be added:

$$\&\ INIT\quad XB = 0.0, 0.1, 0.0, 0.025, 0.0, 0.1,\ TEMPERATURE = 60\ / \tag{1.57}$$

This is to indicate that the temperature is equal to 60°C instead of the ambient within the bounds given by the sextuplet XB [McGrattan *et al.*, 2013].

The geometry into an FDS model is described in terms of rectangular obstructions and vents: both need to be assigned a boundary condition describing its thermal properties. The bounding surfaces consist of the characteristics which are defined by the solid surfaces of a smooth inert wall with the temperature fixed at TMPA, referred to as 'INERT'. Any SURF lines do not need to be added if only this boundary condition is required. Each SURF line consists of an identification string ID = '...': this is to allow references to it by an obstruction or vent. Hence, the character string SURF_ID = '...' on each obstruction or vents indicates the ID of the SURF line containing the desired boundary condition parameters [McGrattan *et al.*, 2013].

The geometry is described in terms of rectangular obstructions defined by the parameters in the namelist group OBST. The entire model is made up of rectangular solids, each one introduced on a single line in the input file. Each OBST line contains the coordinates of a rectangular solid within the flow domain: its position and geometry are defined by two points, (x_1, y_1, z_1) and (x_2, y_2, z_2), that are entered on the OBST line in terms of a sextuplet XB. In addition to the coordinates, the parameter SURF_ID can be used to specify a boundary condition. If different properties occur for the top, sides and bottom of an obstruction, SURF_IDS can be used instead of one SURF_ID. SURF_IDS is an array of three character strings specifying the boundary condition IDs for the top, sides, and bottom respectively [McGrattan *et al.*, 2013].

The VENT group is used to prescribe planes adjacent to obstructions or external walls and are defined by a sextuplet XB denoting a plane abutting a solid surface.. XB can be replaced by MB (Mesh Boundary) to easily specify an entire external wall. MB is a character string, whose value is one of the following: 'XMAX', 'XMIN', 'YMAX', 'YMIN', 'ZMAX', 'ZMIN', denoting x = XMAX, x = XMIN, y = YMAX, y = YMIN, z = ZMAX, and z = ZMIN respectively. The boundary condition of a vent is expressed by means of SURF_ID. No SURF_ID needs to be set if the default boundary condition is desired. A VENT may have three different SURF_IDs [McGrattan *et al.*, 2013]:

- ✓ namelist group SURF. The default boundary condition is 'OPEN', which is used only if the VENT is applied to the exterior boundary of the computational domain. By default, FDS assumes that the exterior boundary of the control volume, namely the XBs on the MESH line, is a solid wall. In order to create a totally or partially open domain, OPEN vents can be used on the exterior mesh boundaries;
- ✓ 'MIRROR', which is used to denote a symmetry plane, corresponding to a no-flux, free-slip boundary. It can be applied only to any exterior boundary of the computational domain;
- ✓ 'PERIODIC', which is used to define a periodic trend.

In order to clearly visualize the results of a simulation, colouring obstruction or vents is useful. Colours can be prescribed into two ways: a triplet of integer colour values, RGB, or a character string, COLOR.

The three RGB integers range from 0 to 255, depending on the amount of Red, Green or Blue that make up the colour. Colour parameters can be specified on a SURF line. The word COLOR needs to be typed exactly as it is listed in the colour tables (figure 16) [McGrattan *et al.*, 2013].

Name		R	G	B	Name		R	G	B
AQUAMARINE		127	255	212	MAROON		128	0	0
ANTIQUE WHITE		250	235	215	MELON		227	168	105
BEIGE		245	245	220	MIDNIGHT BLUE		25	25	112
BLACK		0	0	0	MINT		189	252	201
BLUE		0	0	255	NAVY		0	0	128
BLUE VIOLET		138	43	226	OLIVE		128	128	0
BRICK		156	102	31	OLIVE DRAB		107	142	35
BROWN		165	42	42	ORANGE		255	128	0
BURNT SIENNA		138	54	15	ORANGE RED		255	69	0
BURNT UMBER		138	51	36	ORCHID		218	112	214
CADET BLUE		95	158	160	PINK		255	192	203
CHOCOLATE		210	105	30	POWDER BLUE		176	224	230
COBALT		61	89	171	PURPLE		128	0	128
CORAL		255	127	80	RASPBERRY		135	38	87
CYAN		0	255	255	RED		255	0	0
DIMGRAY		105	105	105	ROYAL BLUE		65	105	225
EMERALD GREEN		0	201	87	SALMON		250	128	114
FIREBRICK		178	34	34	SANDY BROWN		244	164	96
FLESH		255	125	64	SEA GREEN		84	255	159
FOREST GREEN		34	139	34	SEPIA		94	38	18
GOLD		255	215	0	SIENNA		160	82	45
GOLDENROD		218	165	32	SILVER		192	192	192
GRAY		128	128	128	SKY BLUE		135	206	235
GREEN		0	255	0	SLATEBLUE		106	90	205
GREEN YELLOW		173	255	47	SLATE GRAY		112	128	144
HONEYDEW		240	255	240	SPRING GREEN		0	255	127
HOT PINK		255	105	180	STEEL BLUE		70	130	180
INDIAN RED		205	92	92	TAN		210	180	140
INDIGO		75	0	130	TEAL		0	128	128
IVORY		255	255	240	THISTLE		216	191	216
IVORY BLACK		41	36	33	TOMATO		255	99	71
KELLY GREEN		0	128	0	TURQUOISE		64	224	208
KHAKI		240	230	140	VIOLET		238	130	238
LAVENDER		230	230	250	VIOLET RED		208	32	144
LIME GREEN		50	205	50	WHITE		255	255	255
MAGENTA		255	0	255	YELLOW		255	255	0

Figure 16: Colour definitions (RGB) [McGrattan *et al.*, 2013].

1.6.2.4 Thermal boundary conditions

Thermal boundary conditions are often used where there is a few information about the properties of the solid materials. If they are known, it is better to specify these properties and let the model compute the heat flux and temperatures of walls and other solid surfaces. The thermal properties of a solid boundary are specified by means of MATL namelist [McGrattan *et al.*, 2013].

A solid boundary may consist of multiple layers of different materials, and each layer can consist of multiple material components. By default, the maximum number of material layers is 20 and the maximum number of material components is 20. Material layers and components are defined by the SURF line via the array MATL_ID (IL, IC). IL is an integer indicating the layer index, starting at 1 (layer at the exterior boundary), while IC is an integer indicating the component index. For instance, MATL_ID (2, 3) = 'BRICK' indicates that the third material component of the second layer is BRICK [McGrattan *et al.*, 2013].

Without arguments, the parameter MATL_ID is assumed to be list of the materials in multiple layers, where each layer consists of only a single material component. Thermal CONDUCTIVITY [W/(m x K)], DENSITY (kg/m^3), SPECIFIC_HEAT [kJ/ (kg x K)], and EMISSIVITY (0,9 by default) can be specified for any solid material. Moreover, both CONDUCTIVITY and SPECIFIC_HEAT can be functions of temperature, while DENSITY and EMISSIVITY cannot. Temperature-dependence is specified by using the RAMP convention: in this case, the RAMP parameter T means temperature, and F is the value of either the specific heat or conductivity. An ABSORPTION_COEFFICIENT (1/m) can be also assigned to the solid material, allowing the radiation to penetrate and absorbing into the solid [McGrattan *et al.*, 2013].

The layers of a solid boundary are listed in order from the surface. By default, this inner layer is assumed to be in direct contact with an air gap at ambient temperature. However, there are other back side boundary conditions: for example, one considers that the wall backs up to an insulated material in which case no heat is lost to the backing material. In this case, BACKING = 'INSULATED' must be added in the SURF line: this condition means that no other properties of the inner insulating material need to be specified because it is considered as perfectly insulated [McGrattan *et al*, 2013].

In order to calculate the heat transfer through the wall into the space behind the wall when the latter is assumed to back up to the room on the other side of the wall, BACKING = 'EXPOSED' needs to be listed on the SURF line [McGrattan *et al.*, 2013].

However, sometimes a fixed temperature boundary condition may be useful and TMP_FRONT can be set up in the model (by default it is given in °C). If the convective heat transfer needs to be specified, a constant value

HEAT_TRANSFER_COEFFICIENT [W/(m^2 x K)] on the SURF line can be added. Furthermore, instead of altering the convective heat transfer coefficient, a fixed heat flux can be specified. To do that, the NET_HEAT_FLUX (kW/m^2) can be defined: when this parameter is specified, FDS will compute the surface temperature required to ensure that the combined radiative and convective heat flux from the surfaces is equal to the given NET_HEAT_FLUX [McGrattan *et al.*, 2013].

CHAPTER 2

CASE STUDY 1: HEAT TRANSFER IN A DOWNHOLE HEAT EXCHANGER

2.1 Aim of the investigation

According to the Directive 2009/28/CE which was implemented in Italy in 2010, ambitious targets need to be achieved in order to ensure a clean and sustainable future for the forthcoming generations. In more detail, its aim is to reduce greenhouses gases emissions by 20%, to produce 20% of energy from renewable sources and to decrease the consumption by 20% improving the energy efficiency. These goals must be reached by 2020.

This regulation led the public administrations and private stakeholders to investigate new technologies which may face the growing energy demands by the use of renewable sources alternative to fossil fuels. Thus, energy supply might change from being predominantly fossil fuelled to being fuelled by locally available sources. In this scenario, low-enthalpy geothermal plants, such as Downhole Heat Exchangers (DHEs) for heating and cooling buildings can be successfully used [Lo Russo *et al.*, 2009].

The present research investigates the use of a DHE for heating purposes in the Province of Viterbo, Central Italy, calculating the amount of withdrawable heat in Matlab and the heat transfer in the surrounding of the DHE in Comsol Multiphysics.

The chapter encompasses some unpublished results and the following paper:

- Carlini M, Castellucci S, Allegrini E, Tucci A. Down-hole heat exchangers: Modelling of a low-enthalpy geothermal system for district heating. Mathematical Problems in Engineering 2012, art. no. 845192.

The full text is available on www.scopus.com and the .pdf version can be downloaded.

2.2 Introduction

Basically, ground source heat pump systems can be distinguished in two different types: earth- coupled or closed-loop and groundwater or open-loop. In the first case, heat exchangers are underground and located horizontally (known as GSHP, acronym for "ground source heat pump"), vertically (known as DHE, acronym for "down-hole heat exchanger") or obliquely. Heat is transferred from or to the ground thank to a heat-carrying which circulates within the exchanger [Lo Russo *et al.*, 2009].

The exploitation of geothermal resources by DHEs is not characterized by mass withdrawal from the aquifer: more precisely, they permit heat transfer without extracting any fluid from the ground. This is to avoid the aquifer depletion, as requested by legislative restrictions. However, an important aspect has to be considered: the amount of withdrawable heat may be limited and is usually less than 100 kW. This phenomenon is mainly due to the interaction between heat exchanger, well and aquifer. As a consequence, DHEs are mostly used in small applications, such as buildings, greenhouses and thermal baths [Carotenuto *et al.*, 2001; Carotenuto *et al.*, 2012].

In order to increase vertical circulation of water and the natural mass transfer between aquifer and well, promoters can be used. The exchangers consist in pipes or tubes which are located within the well. Because of the low capacity, these systems are successful up to 150 m of depth. Several designs are nowadays available but the most common one is a U-tube which extends to near the bottom of the well. Multiple tubes can be alternatively used [Lund, 1999].

In Italy, several studies were carried out in the past and led to the reconstruction of the stratigraphy, the evaluation of heat flow, the probable origin of hot waters and the chemical properties of gas and hydrothermal emissions. Della Vedova *et al.* developed a new heat flow map as shown in figure 17: it can be seen how the highest values (red and orange areas) are mostly located in the Tyrrhenian Sea and in Central Italy (western coastline, especially in Tuscany and northern Latium) [Della Vedova *et al.*, 2001; Scrocca *et al.*, 2003].

The Province of Viterbo is located in northern Latium and hosts several thermal springs in its territory. They had been already known by Romans who used them for therapeutic purposes. Bullicame Spring is one of the most famous hydrothermal source and is even mentioned by the poet Dante Alighieri.

Nowadays, thermal waters are exploited for direct use or to supply spas and pools [Piscopo *et al.*, 2006].

In the Province of Viterbo, hydrogeological settings and shallow groundwater basins seem to be particularly suitable for a wide implementation of DHE systems. Moreover, performances of geothermal heat pumps are significantly limited since groundwater basin temperatures vary from 40°C up to 90°C. Thus, their use is not recommended and implemented in the area [Piscopo *et al.*, 2006].

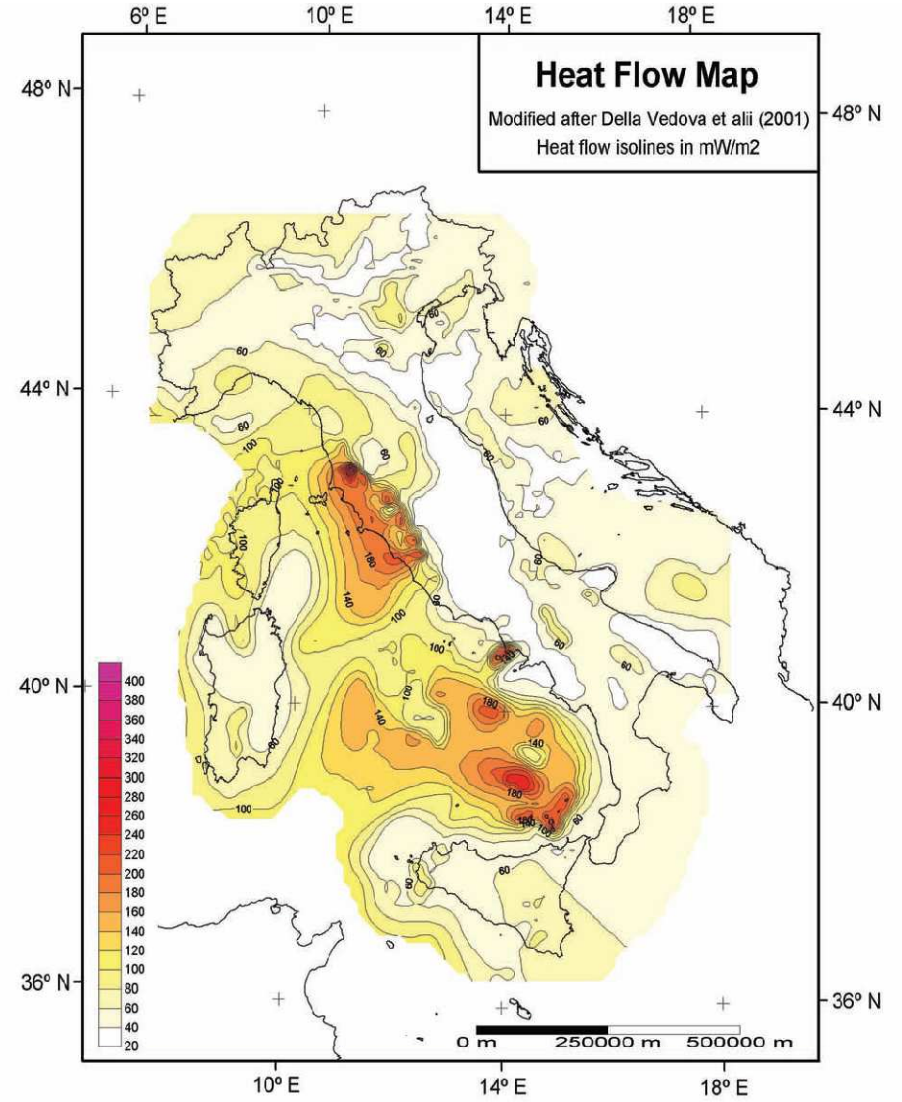

Figure 17: Heat flow map [Della Vedova *et al.*, 2001].

Figure 18 shows the location of Viterbo hydrothermal area (dotted circle) within the regional geological picture. The investigated area lies between the Tyrrhenian coastline and the Apennines. From a geological point of view, the region is characterized by sedimentary basins belonging to the upper Miocene-

Pleistocene age, elongated between ridges of Mesozoic-Paleogene rocks, which overlay a Paleozoic-Triassic metamorphic basement. Within this geological framework, Cimini volcanic complex consists of quartzolatitic domes and ignimbrites and lavas. The Vico complex is characterized by explosive activity and is a typical stratovolcano. The substrate beneath them is made of sedimentary rocks [Piscopo *et al.*, 2006].

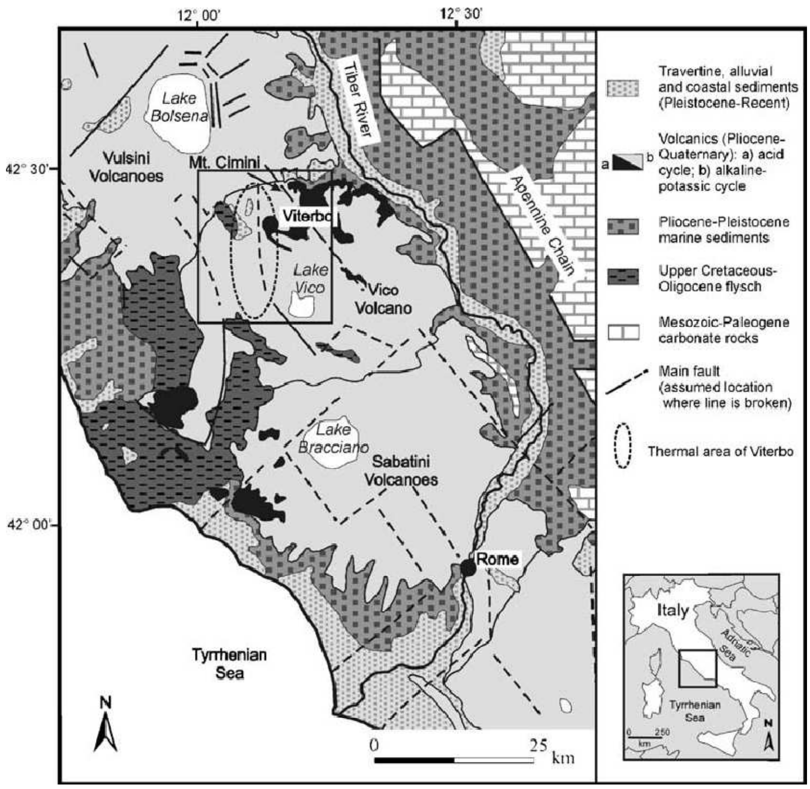

Figure 18: Hydrothermal area within the regional geological picture [Piscopo *et al.*, 2006].

An appropriate interpretation of the stratigraphy is successfully reached by drilling wells and can be correlated to surface geology in order to get the reconstruction of the hydrostratigraphy of the thermal area. Formations of Cimini and Vico complexes occur from the first 10 m down to 100 m. The shallow unconfined aquifer consists in these rocks and its thickness decreases where there are more layers of travertine. Plio-Pleistocene deposits lie beneath the volcanic aquifer and marly-calcareous-arenaceous flysh occurs below them [Piscopo *et al.*, 2006].

The Province of Viterbo is characterized by overlapped interacting aquifers. More precisely, the shallow volcanic aquifer has fresh waters which come from the area around Cimini Mountains. It is limited at the bottom by the semiconfining marly-calcareous-arenaceous complex and low-permeability clays. Vertical upflows of thermal waters –consisting in sulphate-chloride-alkaline-earth type and gases- occur westwards of Viterbo. This phenomenon is mainly due to the uplifted carbonate reservoir, the limited thickness of the semiconfining layer and the high local geothermal gradient. Hot waters are characterized by temperatures varying between 30 and 60°C thank to the deep circulation in carbonate rocks. The minimum upward flow is 0,1 m^3/s, feeding springs and deep wells [Piscopo *et al.*, 2006].

A high concentration of wells and thermal springs occurs in the central area of the Province of Viterbo. Data –such as elevation, discharge and temperature- are available. With specific regard to the most important thermal springs in the province, the following data are given [Piscopo *et al.*, 2006]:

Name	Elevation (m a.s.l.)	Discharge (l/s)	Temperature (°C)
Bagnaccio	310-390	10	38-64
Monterozzo	305-319	5	27-51
Zitelle	289-308	6,5	39-65
Carletti	285	1,5	57
Bullicame	298	10,4	57
S. Cristoforo	245	0,1	53
S. Sisto	230	3	57
Bacucco	315-320	2	36-49
Urcionio	305-319	20	28-60

Table 2: Data of the main thermal springs in the province of Viterbo [Piscopo *et al.*, 2006].

2.3 Materials and methods

The experimental plant is located in the central thermal area of figure 19 and was provided by Mr. Daniele Cortese, who owns the company "Plants and Bulbs". Since regulations discourage the drilling of new wells, an existing one was chosen to develop the system. Moreover, the well is linked to the volcanic aquifer which is characterized by low hydraulic gradients and lays between swampy deposits and travertine. The local substratum is more than 50 m deep and consists in marly-calcareous-arenaceous complex [Carlini and Castellucci, 2010].

The low-enthalpy geothermal system can be easily drafted as a reservoir which contains hot water and a pipe. According to the drilling log, the well is 60 m deep below the ground level. Its diameter is 150 mm and reaches the bottom of the aquifer. Moreover, a steel flanged pipe is located on the top of the well in order to contain the upflow water, which is generated by gases pressure, and reaches 1,5 m above ground level. The heat exchanger consists in a single vertical U-pipe: the internal and external diameters are 29,1 mm and 33,7 mm respectively and the total length is 110 m. The pipe is made of steel and its thickness is 4,6 mm. The hydraulic system is made of PVC pipes connected to the heat exchanger (figure 20). Moreover, the plant is set through manual valves in order to allow series or in parallel connection between the heat exchangers. The hydraulic system is equipped with a pressure gauge and a valve to avoid air accumulation within the pipes which may reduce fluid flow and heat transfer [Carlini and Castellucci, 2010].

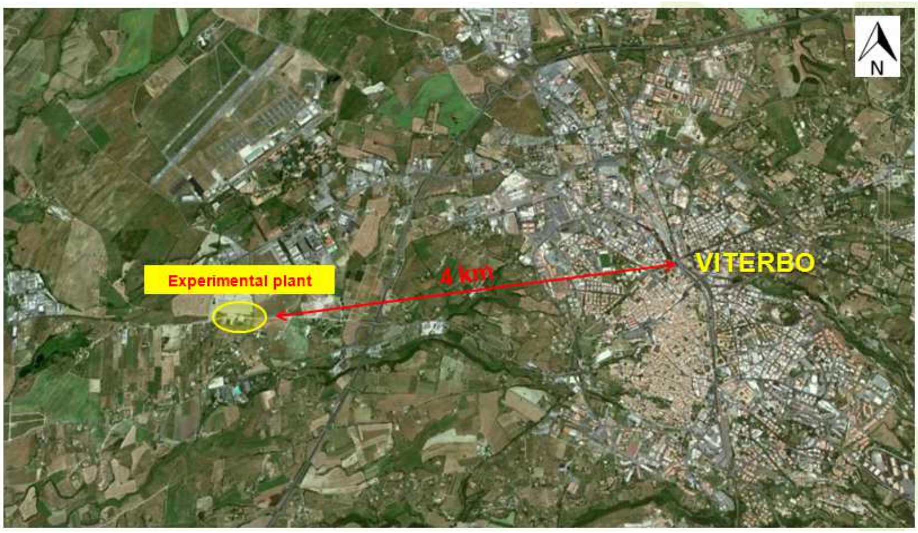

Figure 19: Location of the low enthalpy system.

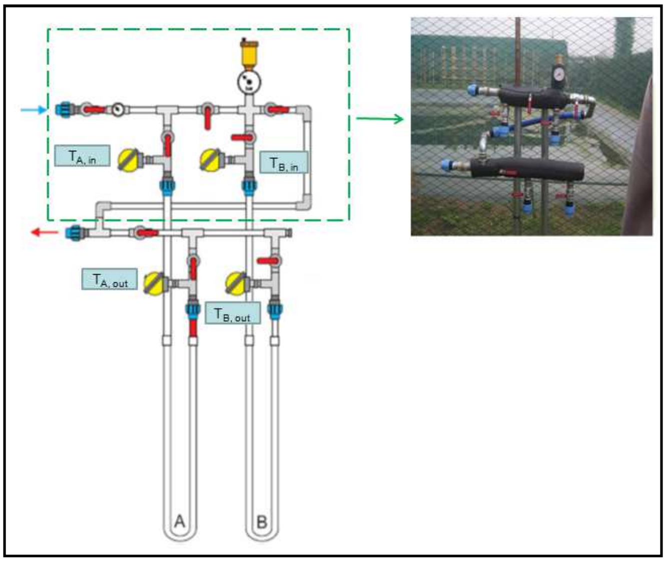

Figure 20: Hydraulic system of the DHE.

Measurements of the groundwater basin temperature were carried out at different depths, 2, 26 and 44 m respectively (figure 21): after a very rapid transitory of 15 minutes, the temperature shows a constant trend, reaching 60°C. The water temperature was measured by a PTC sensor, while the operating conditions were controlled by a monitoring system [Carlini and Castellucci, 2010].

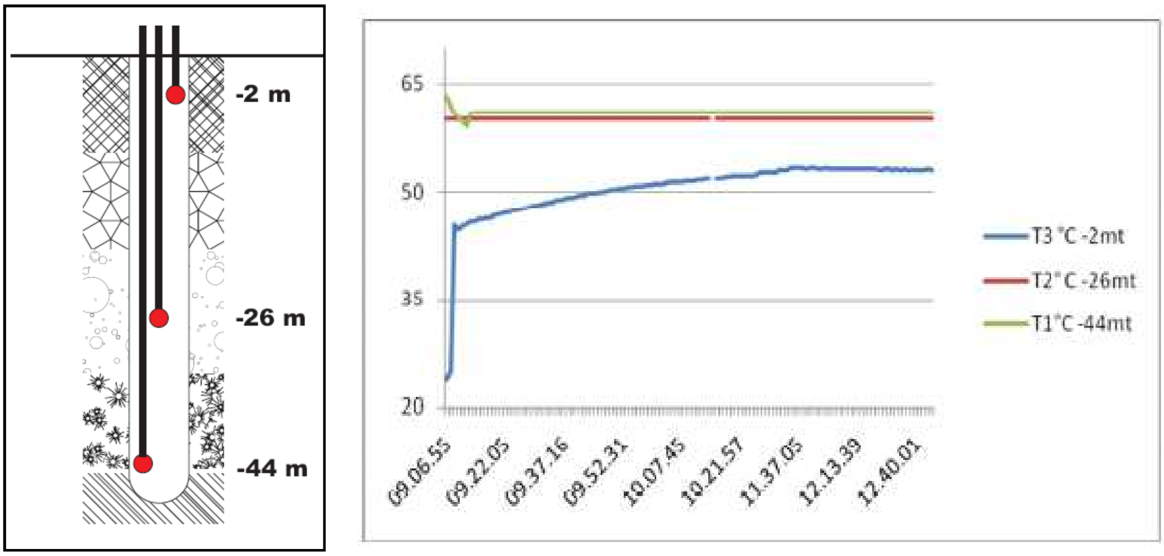

Figure 21: Temperature measurements at different depths.

Three different modes of heat transfers occur: natural convection in the groundwater basin, conduction within the wall of the pipe, and forced convection inside the heat exchanger. The latter is due to the pumping of water. The groundwater within the well is characterised by convective motions which are due to differences of density and consequently cause heat transfers [Carlini and Castellucci, 2010].

In order to evaluate the total amount of withdrawable heat using the above-described system, an implementation in MATLAB is developed. The overall heat transfer rate is formally represented by:

$$Q = A \cdot U_D \cdot \Delta T_{LM} \tag{2.1}$$

where U_D can be successfully calculated using the following formula:

$$\frac{1}{U_D} = \frac{1}{h_{io}} + \frac{d_{ext}}{2k} \cdot \ln\left(\frac{d_{\text{int}}}{d_{ext}}\right) + \frac{1}{h_{eo}} + R \tag{2.2}$$

The second term in the definition of U_D is related to conduction but can be neglected since the thickness of the tube is limited. Moreover, k results from the type of material and R is tabulated depending on type of fluid, heat exchangers and temperature.

Figure 22 shows a schematic model with the different modes of heat transfers and the heat transfer coefficient related to them [Carlini and Castellucci, 2010; Carlini *et al.*, 2010; Carlini and Castellucci, 2011; Cui *et al.*, 2011; Michopoulos *et al.*, 2011; Ostergaard and Lund, 2011; Shengjun *et al.*, 2011;].

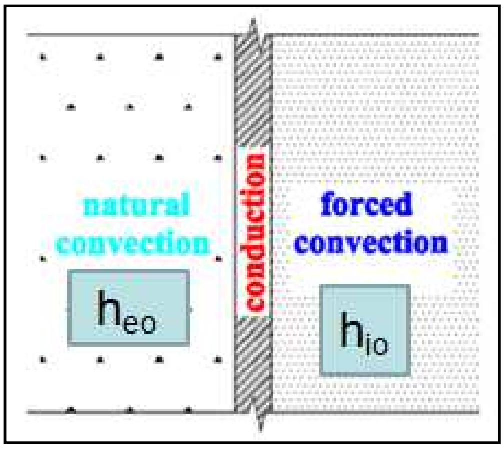

Figure 22: Heat transfers and heat transfer coefficients.

In Eq. (2.2), h_{io} can be calculated using the Reynolds number and the heat transfer coefficient J_h which depends on fluid motion conditions inside the pipe. The Reynolds number is related with the water velocity inside the heat exchanger which can be easily calculated using the values of flow rate at the entrance of the pipe and the cross section area [Carlini and Castellucci, 2010].

Moreover, h_{eo} depends on several parameters -such as the density of the fluid in the groundwater basin and the coefficient of thermal expansion- which result from the temperature of the film (T_{film}) between the thermal water and the wall of the heat exchanger. Thus, T_{film} is linked to the water temperature inside the well (T_{ext}) and the temperature of the wall (T_{wall}). T_{wall} is obtained using $T_{m,fluid}$ (mean temperature of the fluid in the pipe) and T_{ext}. In order to calculate $T_{m,fluid}$, the values of water temperature at the beginning (T_{in}) – which is known- and at the end (T_{out}) of the tube are required. The mean temperature profile within the pipe can be defined by the following equation [Carlini and Castellucci, 2010]:

$$T_{out}(x) = T_{ext} - (T_{ext} - T_{in}) \cdot \exp\left(-\frac{P \cdot U_D}{\dot{m} \cdot c_p} \cdot x \right) \qquad (2.3)$$

Since T_{out} depends on U_D which results from h_{io} and h_{eo}, an iteration loop is developed in MATLAB: an initial value for T_{out} and h_{eo} is adopted and the iteration process continues until the convergence is reached. MATLAB is a high-level language and interactive environment which enables you to perform numerical computations and intensive tasks. It is an abbreviation for "MATrix LABoratory" and is designed to operate primarily on matrices and arrays [www.mathworks.com.].

After defining the temperature profile within the heat exchanger, a simulation in Comsol Multiphysics was carried out in order to analyse the thermal behaviour of the well surrounding at 44 m-depth.

The Module Heat Transfer was used and involved the following stages:

- selection of the space dimension, namely 2D to represent the horizontal section;
- drawing the geometry of the problem after defining parameters in the Global Definition branch, as shown in table 3. The geometry consists of 6 domains;
- choice of the material and its thermophysical properties for water and steel according to the Material Library in Comsol Multiphysics, and for the basalt according to the value given in table 3;
- selection of the physics and definition of the boundary conditions, as shown in figure 23, in order to solve the differential equation;
- meshing the control volume, following the physical-controlled mesh. A normal size was chosen for the simulation, consisting of 1852 and 208 domain and boundary elements respectively;
- results visualization in terms of isothermal contours.

Parameters	Description
D_int_p = 29,1 mm	Internal diameter of the pipe
D_ext_p = 33,7 mm	External diameter of the pipe
D_w = 150 mm	Diameter of the well
D_s = 80 cm	Diameter of the surrounding volume
T_44_wat = 60°C	Water temperature at 44 m
T_44_p_in = 28°C	Inlet water temperature at 44 m
T_44_p_out = 37°C	Outlet water temperature at 44 m
k_b_2 = 2,5 W/m/K	Thermal conductivity of basalt

Table 3: Parameters for the Geometry Branch.

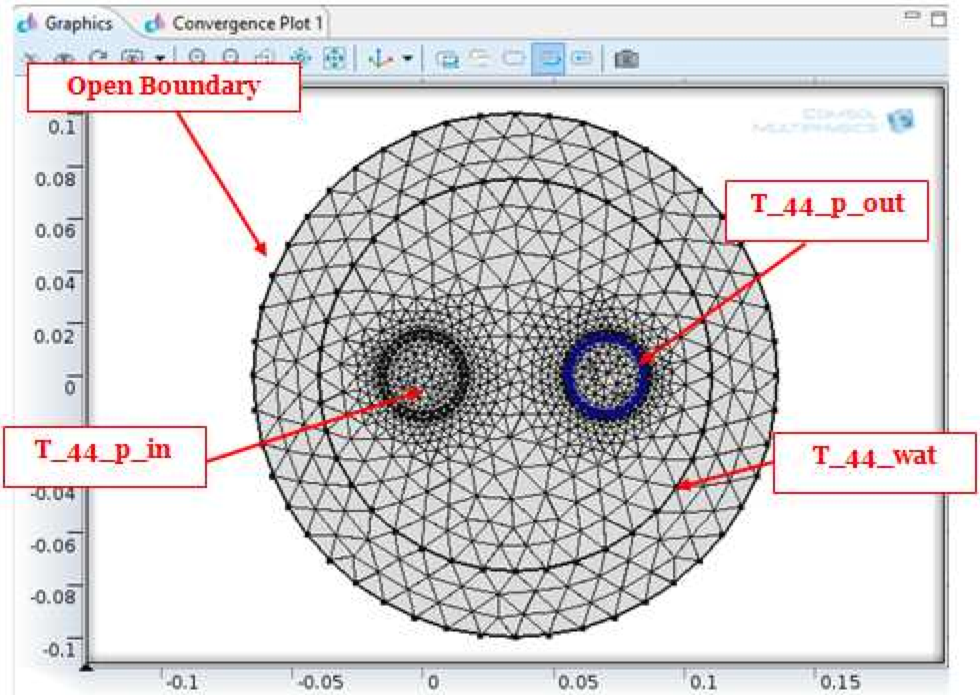

Figure 23: Meshing phase and boundary condition.

2.4 <u>Results and discussion</u>

The results in table 4 are given by the implementation in MATLAB environment. It can be seen that the condition of turbulence occurs because of the high value of the Reynolds number. The water temperature on the outgoing cross section of the DHE is equal to 45°C, thus increasing up to 30°C if compared with the initial value at the entrance (15°C). The temperature difference is only due to the heat transfer occurring between terrain, groundwater basin, pipe and water within the DHE.

The calculation of these parameters led to define the water temperature trend along the U pipe, namely the spatial coordinate x, as shown in figure 24. It can be noted that the temperature value rapidly increases as far as the fluid reaches the end of the DHE. The water exiting the DHE has a limited value if compared with Chiasson *et al.* (2004) and Culver and Lund (1999), who considered a 123-m deep well cased to 112 meters with a bottom hole temperature of 160 °C. However, this value is in good agreement with Steins *et al.* (2008) who investigated two wells drilled to 55 m. The survey demonstrated that the outlet temperature ranges between 42 and 77°C, the temperature difference from 2 to 33°C and the heat output from 2 to 49 kW. Moreover, the heat output generated from the low-enthalpy geothermal system can be successfully used for civil purposes, such as district heating, which provides energy to supply thermal needs [Muñoz, 2015].

		OUTPUT			
Re	34543	**T_{out}**	45 °C	**U_D**	138 W/m²/K
$T_{m,fluid}$	30 °C	**h_{io}**	4269 W/m²/K	**A**	11,65 m²
T_{wall}	31 °C	**h_{eo}**	146 W/m²/K	**ΔT_{LM}**	27,31 K
T_{film}	45,5 °C			**Q**	43386 W

Table 4: Output data generated in Matlab.

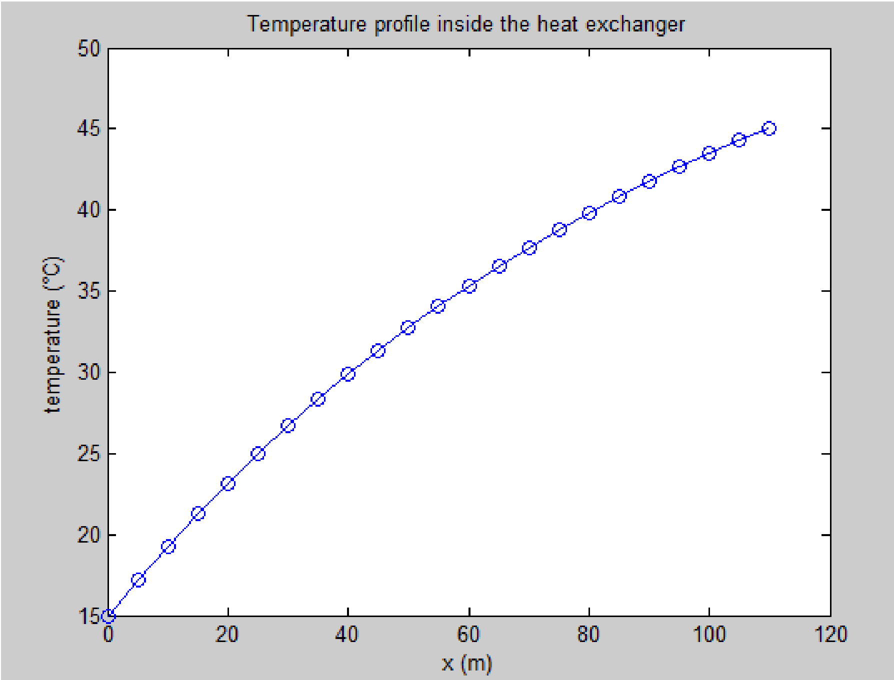

Figure 24: Temperature profile of the water within the heat exchanger.

The result in Comsol Multiphysics is shown in figure 25 in terms of isothermal contours within the DHE and the well and considering the surrounding. The maximum temperature of the system -when the depth is equal to 46 m- is reached within the groundwater basin (59,2°C) because of the influence of the surrounding hot terrain. Moving closer to the DHE, the temperature decreases: then, if we consider the arrow surface, the direction of the total heat flux is given and is oriented from the terrain to the DHE.

Figure 26 represents the convergence plot: because of the experimental measurement of the groundwater temperature, the convergence is reached very quickly, after 3 iterations.

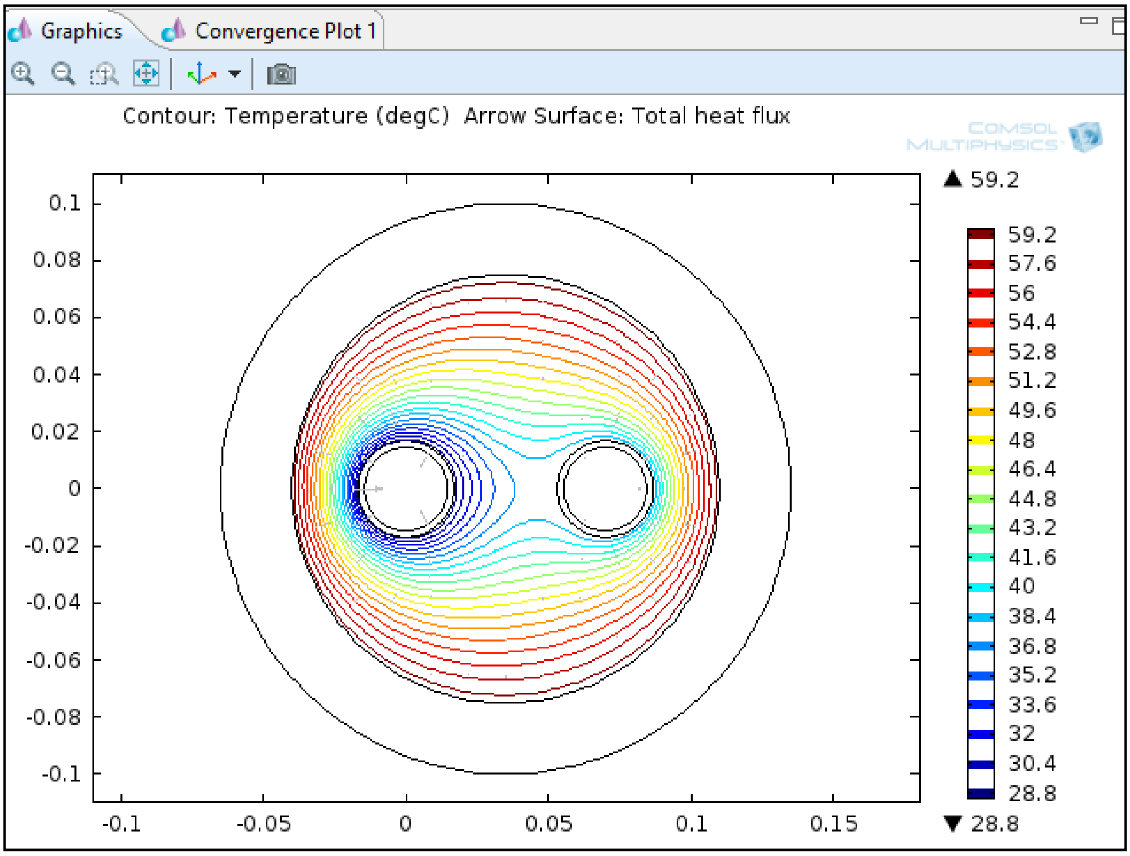

Figure 25: Isothermal contours on the DHE surrounding.

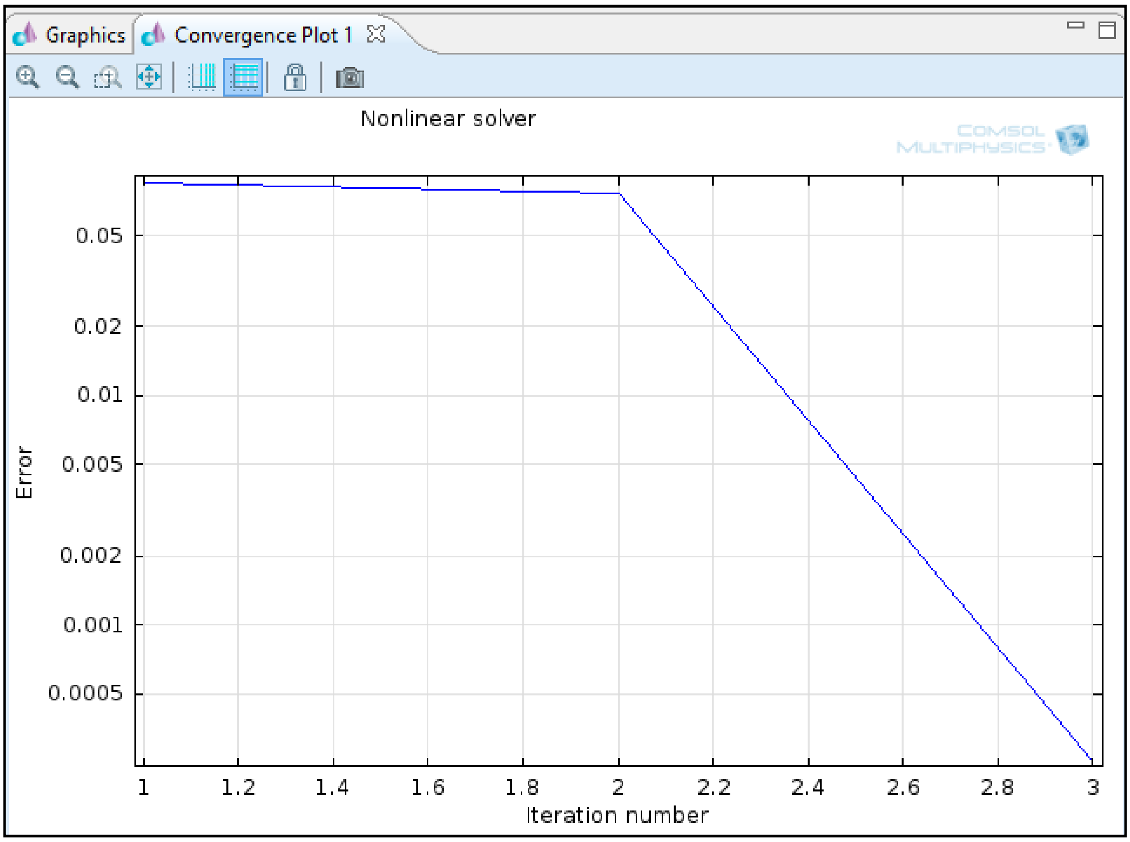

Figure 26: Convergence plot.

2.5 Conclusion

The research investigated the use a DHE for heating purposes in the Province of Viterbo, Central Italy, calculating the amount of withdrawable heat in Matlab and the heat transfer in the surrounding of the DHE in Comsol Multiphysics.

The mathematical modelling in MATLAB led to evaluate the withdrawable heat from a DHE in a low-enthalpy geothermal plant using an iterative approach to determine those parameters related to convective motion within the system. Once the obtainable heat is known and according to the specific thermal needs, the system can be used for heating purposes by means of radiant floors, requiring very limited working temperatures (generally 40°C).

It is important to underline that the implemented model can be successfully used in those areas where shallow thermal ground basins occur and if their temperature is close to 60°C. Furthermore, the investigation highlighted the importance of exploiting local available renewable sources, as shown in Lei and Dai (2015).

Since the model was created from measurements *in situ*, future improvements may be reached by the validation with more case studies.

Besides, considering that the simulation in Comsol Multiphysics was carried out using geometrical parameters, other situations –different in terms of material, boundary conditions- may be rapidly solved. More horizontal sections can be further analysed by developing a Thermal Response Test, which is commonly used for measuring the ground thermal conductivity and the thermal resistance R [Acuna, 2013]. The TRT method was first used by (Mogensen, 1983) and then by (Eskilson *et al.,* 1987) and (Claesson and Hellström, 1988) and (Gehlin, 2002). The reliability of this method as compared to laboratory core tests was demonstrated by Liebel (2012) [Acuna, 2013].

CHAPTER 3
CASE STUDY 2: THERMAL BEHAVIOUR OF EXTERNAL OPAQUE ENCLOSURES IN EXISTING BUILDINGS

3.1 Aim of the investigation

The updated version of the Energy Performance of Buildings Directive (EPBD) has been recently published by the European Commission and focuses on the need of Energy Efficient Retrofitting (EER) in existing buildings.

EER is aimed at reducing the total energy demand, simultaneously ensuring the required levels of occupants' thermal comfort, and encompasses several actions, such as the installation of thermal insulation, limitation of thermal bridges, and use of mechanical ventilation with heat recovery [Zhao and Magoulès, 2012; Terés-Zubiaga *et al.*, 2013; De Rosa *et al.*, 2014].

Thus, the investigation presents the possible retrofitting actions on opaque enclosures and thermal bridges for an existing public building in Italy, considering the steady state approach and following the current national regulations. In order to evaluate the improvement given by the specific EER, a simulation of the heat transfer through the building envelope is carried out both for the external wall and thermal bridges during winter and summer.

The present chapter encompasses two different papers and shows some unpublished results:

- Carlini M, Allegrini E, Zilli D, Castellucci S. Simulating heat transfers through the building envelope: A useful tool in the economical assessment. Energy Procedia 2014; 45: 395-404 (available on www.scopus.com);
- Carlini M, Allegrini E, Zilli D. Simulating building thermal behaviour: the case study of the School of the State Forestry Corp. Submitted and accepted by Energia Procedia.

3.2 Introduction

Buildings account for approximately 40% of energy consumption in the European Union (EU), 63% of which is attributed to the residential sector. Thus, it has become a relevant environmental issue, especially if we consider that buildings constitute a major pollution source: CO_2 from residential buildings represents the fourth largest source of greenhouse gases (GHG) emissions in the EU, contributing to 10%. The average energy consumption in Europe has recently reached 200 kWh/m^2/year [Kolaitis *et al.*, 2013; Foucquier *et al.*, 2013; Stazi *et al.*, 2013; Marique *et al.*, 2014].

Reducing the energy demand and exploiting Renewable Energy Sources (RES) represent a reachable target in the built environment so that building sustainability is a fundamental tool to provide healthy and comfortable indoor conditions, limiting the impacts on Earth's natural resources. Since the majority of existing structures were built before energy efficiency was a concern at all and most of them will be in function at least until 2025, retrofitting the existing building stock has a large potential for improving energy performance and decreasing pollutant emissions [Kapsalaki *et al.*, 2012; Martin *et al.*, 2012; Hang *et al.*, 2013].

Moreover, energy renovations have positive implications and benefits not only in GHG emissions reduction and energy savings, but also in social and financial aspects, e.g. fuel poverty. The role and importance of energy efficiency has been also underlined by the Directive 2012/27/EU, which establishes a common framework of measures for achieving the Union's 2020 headline targets and requires each Member State to identify reference case studies for minimum energy performance. Furthermore, since buildings owned by public bodies represent a considerable share of the building stock, renovation strategies need to be investigated for this sector. This becomes even more important if we consider that the average efficiency of public bodies' buildings is 50%, where the amount of primary energy losses reaches 6,5 Mtep (figure 27) [Mazzarella and Piterà, 2013; Stazi *et al.*, 2013].

Energy saving regulations originated in cold climates, where the fundamental concern is to reduce the winter energy consumption for space heating and to prevent heat loss through the building, having a stationary behaviour during the year. Thus, following the European trend, Italy set limits for stationary and periodic parameters in new constructions or when renovating existing buildings, as laid down by the Legislative Decree 192/05 and its subsequent directives [Stazi *et al.*, 2013].

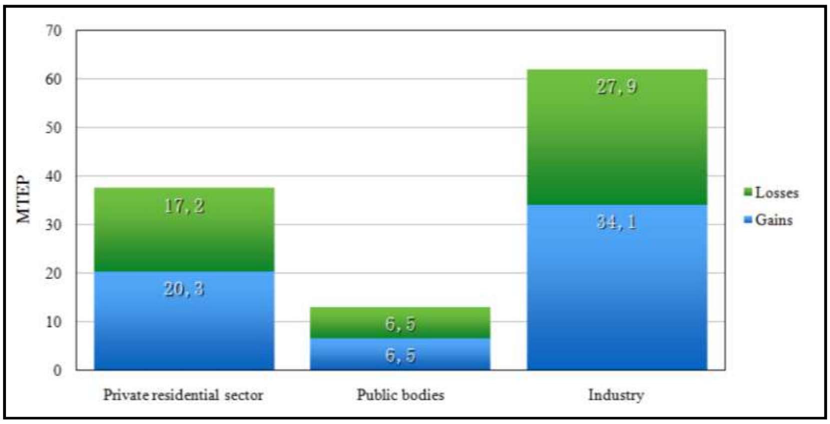

Figure 27: Share of losses and gains in the private buildings, public bodies' buildings and industry [Mazzarella and Piterà, 2013].

Energy-efficient measures are increasingly implemented in all the EU Member States, leading to establish many regulations for assessing building energy performances and the thermal properties of the building envelope elements. Most European standards address building behaviour with specific regard to the heating demand aspect or provide limits for the thermal transmittance. The latter has therefore become a common indicator for defining the thermal quality of the building shell and the steady-state heat transmission can be seen as the main reference, although it neglects the ability of materials in storing and releasing heat over time (i.e. the dynamic characteristics related with the so called inertia effect). The thermo-physical properties of the building envelope may be distinguished into two groups, depending on the type of heat transfer mechanism. The overall heat transfer coefficient and the transparency ratio belong to the first category, while the latter encompasses time lag and decrement factor [Stazi *et al.*, 2013].

3.3 Material and methods

3.3.1 Physical models to simulate building thermal behaviour

Different physical models are used to describe the building thermal behaviour depending on their specific needs, including space heating, ventilation, air conditioning systems, occupants behaviours, use of RES, and financial aspects. The physical building performance is based on the solving of the heat transfer differential equations, which can be written in terms of the energy conservation law and taking into account the conduction through the walls, the convection, the longwave and shortwave radiation, and the ventilation [Foucquier *et al.*, 2013].

A large number of numerical software products are nowadays available to solve such physical problems, both in stationary and dynamic conditions. The steady state approach is commonly used to assess the building energy performance and leads to long-term analyses of different scenarios thank to their fast calculations. Thus, the present investigation implements the stationary approach, although a considerable limitation occurs since the inertia of the building envelope is completely neglected. However, since the aim of the analysis is to consider extreme temperature conditions, the effect of unsteady elements - namely outdoor climatic variability and indoor heat production- can be neglected in the simulation [Foucquier *et al.*, 2013].

The building thermal models are divided into three different typologies, namely the multizone, the zonal and CFD methods: each one has its own application depending on the specific problem. The present research involves the use of the first approach, which is based on the following assumption: each building zone is a homogeneous volume with uniform state variables and may be approximated to a node that is described by a unique temperature, pressure, etc. (figure 28). A node may represent a room or the exterior of the building itself or a load. This technique is capable to describe the behaviour of a multiple zone building in a very limited computational time and is particularly useful in evaluating the energy consumption and the time evolution of temperature within a room [Foucquier *et al.*, 2013].

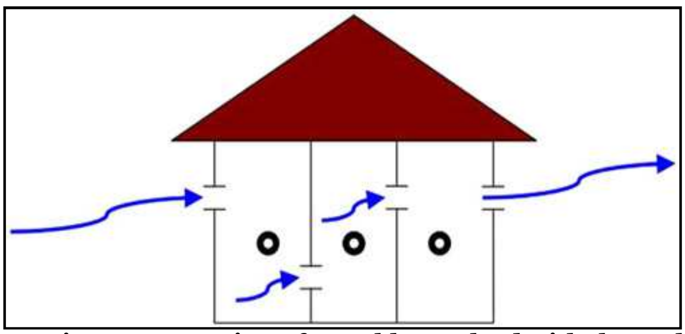

Figure 28: Schematic representation of a problem solved with the multizone method [Foucquier *et al.*, 2013].

3.3.2 Description of the case study

The existing structure is a multi-storey building owned by the School of the State Forestry Corp in Sabaudia (Central Italy, Province of Latina), containing offices, bedrooms, kitchens, and rooms. It was built at the beginning of 1950s and will be renovated in those areas within the red rectangle in the floor plan shown in figure 29 and including the buildings denoted with the capital letters E, F, and G. General data on the building and its conditioned space and volume are given in tables 5 and 6.

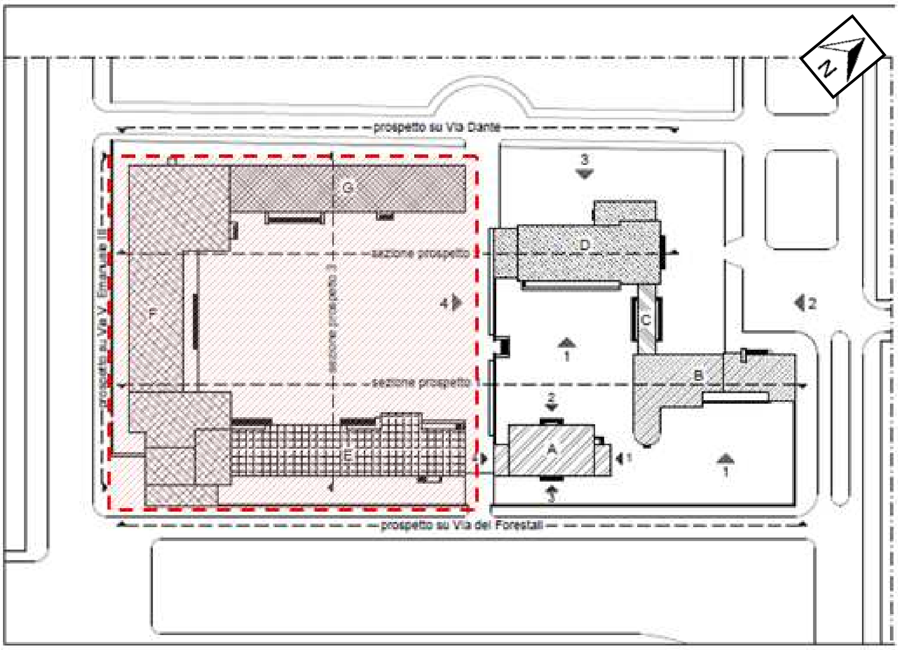

Figure 29: Plan of the existing building and buildings to be renovated.

Figure 30: View of the building F from Via Vittorio Emanuele II [Google Maps].

Figure 31: View of the building E from Via dei Forestali [Google Maps].

Figure 32: View of the building G from Via Dante [Google Maps].

Use class	Residential
Category of use classes	E.1 according to the Presidential Decree 412/93
Latitude/Longitude	41,3001 N/ 13,0317 E
HDD	1171 according to the Presidential Decree 412/93
Duration of the heating period	November 15 – March 31
Number of heating days	136
Climatic zone	C according to the Presidential Decree 412/93

Table 5: General data on the building.

Floor area	1833 m²
Gross conditioned space	3766 m²
Net conditioned space	2636 m²
Conditioned volume	11 006 m³
Ratio S/V	0,5 1/m

Table 6: Conditioned space and volume.

The building consists of 17 typologies of single or double glass windows with aluminium frame. The overall thermal transmittance of the transparent enclosures is calculated according to the analytical method reported in UNI 10077:2008 and varies depending on the considered typology. Following the above mentioned regulation, the thermal transmittance of a single window can be calculated as:

$$Uw = \frac{U_g \cdot A_g + U_f \cdot A_f + \Psi_g \cdot I_g}{A_g + A_f} \tag{3.1}$$

The minimum thermal transmittance of the different windows is 3,36 W/m²/K and the maximum value is equal to 6,22 W/m²/K. The total dispersion surface towards the external environment accounts for 5498 m², of which the vertical dispersion represents the most significant amount, consisting of 2785 m² (51%).

The external walls are made of solid brick masonry without any insulation cover, while the internal walls are made of 12 mm-thick bricks and 2 mm of internal and external plaster. The roof consists of concrete elements with a waterproof layer and the tiles are finished with majolica. The thermal transmittance of opaque elements is calculated according to UNI EN ISO 6946:2008 and is given by the following expression:

$$U_{wall} = \frac{1}{R_{si} + \sum_{i=1}^{m} \frac{s_i}{\lambda_i} + \frac{1}{C} + R_a + R_{se}} \tag{3.2}$$

According to Eq. 3.2, the thermal transmittance of the internal wall and roof are equal to 1,921 and 1,967 W/m²/K respectively. Since the aim of the research is to investigate the thermal behaviour of the external opaque enclosures, the thermophysical properties are given in table 7, leading to the calculation of the total thermal transmittance of the whole layer which is 1,433 W/m²/K. It has to be noted that R_{si} and R_{se} depend on the type of flux (horizontal, descendant or ascendant) and are related to the convective motion and radiation. The calculation was carried out according to the following assumptions: horizontal heat flux through the wall, surface emissivity equal to 0,9 and radiation and convective coefficients were evaluated considering 20°C for R_{si} and 10°C for R_{se} (table 7).

	s (m)	λ (W/m/K)	R (m^2K/W)
R_{si}			0,13
Internal plaster	0,02	0,700	0,029
Brick	0,14	0,590	0,237
Stones and mortar	0,08	0,900	0,089
Brick	0,14	0,590	0,237
External plaster	0,02	0,700	0,029
R_{se}			0,04

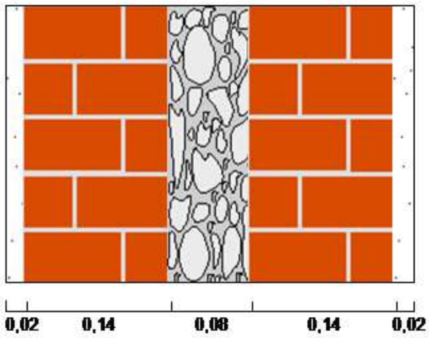

Table 7: Thermophysical properties of the external wall [Zilli, 2014].

The energy audit of the building was carried out in MC11300, a commercial software complying with the requirements laid down by the Comitato Termotecnico Italiano (CTI) and national regulations, and led to the Energy Performance Certificate (EPC).

The EPC was first introduced by the European Directive 2002/91 and is meant as the amount of energy actually consumed or estimated to meet the different needs associated with a standardised use of the building itself, which may include heating, hot water heating, cooling, ventilation and lighting. This amount shall be reflected in one or more numeric indicators which have been calculated taking into account insulation, technical and installation characteristics, design and positioning in relation to climatic aspects, solar exposure and influence of neighbouring structures, own-energy generation and other factors, including indoor climate, that influence the energy demand [European Directive 2002/91].

The above-mentioned regulation was repealed by the European Directive 2010/31 with effect from 1 February 2012. Since buildings account for 40% of total energy consumption in the Union and the sector is still expanding, Member States shall ensure that all new buildings occupied and owned by public authorities are nearly zero-energy buildings, by 31 December 2020 and 31 December 2018 respectively. In more detail, a “Nearly Zero-Energy Building” (NZEB) is referred to a very high energy performance structure as determined in accordance with Annex I. A very limited amount of energy required should be covered -to a very significant extent- by energy from renewable sources, especially on-site or nearby [European Directive 2010/31].

The European Directive 2012/27 establishes a common framework of measures for promoting energy efficiency within the Union in order to ensure the achievement of the Union's 2020 20% headline target on energy efficiency and to pave the way for further energy efficiency improvements beyond that date [European Directive 2012/27] .

With specific regard to Italy, the concepts of energy savings in buildings, rational utilisation of energy and sustainable use of RES were introduced by the National Law 10/91. In the recent years, the legislative framework has been further developed and still changing in order to comply with the above-described European Directives. The following national regulations must be taken into account to carry out the EPC:

- Legislative Decree 192/05 on energy efficiency of buildings;
- Legislative Decree 311/06 which encompasses corrections and integrations to the Legislative Decree 192/05;
- Presidential Decree 59/09 which enforced Legislative Decree 192/05;
- National guidelines for energy performance set by the Ministerial Decree 26/06/2009;
- UNI TS 11300;
- Ministerial Decree 22/11/2012, including corrections and integrations to the Ministerial Decree 26/06/2009.

Recently, the Legislative Decree 63/13 has been adopted, modifying some parts of the previous regulations: until a new calculation methodology is not available, the previous regulation (namely Legislative Decree 192/05) must be followed. In more detail, the EPC is given on a scale from A^+ - the most efficient homes - to G - the most energy consuming one. Accordingly, several indicators were calculated for the present case study, namely EP_{DHW}, EP_W, and EP_{GL} of the whole building following the quasi-stationary approach and for two different scenarios:

a) *asset rating*, which is based on standard weather conditions and building use (referred to as "EX ANTE STD");
b) *tailored rating*, which is based on the measured energy use and takes into account how the building itself is managed and used. Monthly

energy and thermal consumptions are available for 2010, 2011 and the first semester of 2012 and show that the standard values coming from a) exceed real consumptions up to 35%. Thus, in order to correct the asset rating, the occupancy of the building was considered and led to calculate the number of heating days (corresponding to 100 instead of 136 as it is in the asset rating). The number of heating hours was modified and assumed equal to 10. The different scenarios belonging to b) are denoted by the two letters "TR" and are referred to the current situation of the building ("EX ANTE TR") and to the suggested Energy Saving Opportunity ("ESO TR").

Table 8 shows the EPC for the building in the different scenarios: three ESOs are taken into account, involving the installation of an external insulation cover of different thickness, 8, 10, and 12 cm respectively. The external thermal insulation leads to several advantages in the existing building, such as the reduction of the thermal bridges, an appropriate thermo-hygrometric behaviour of the wall and a significant increase of the thermal inertia. Although the internal insulation is less expensive, it is not recommended in the present study in order to avoid useful volume reduction and to totally eliminate thermal bridges (e.g. window-wall, window-floor).

As it can be easily seen in table 8, ESO 1, 2, and 3 improve the building energy efficiency, reducing EP_{GL} up to approximately 50% if compared to "EX ANTE STD" and 28% if we consider "EX ANTE TR". Moreover, the use of the smallest thickness of insulation in ESO1 permits to improve the energy class of the building, from G to F, because of the EP_{W} reduction, which still occurs in ESO 2 and 3. With regard of EP_{DHW}, the value does not change in the different ESOs since they do not consider the installation of a new heat generator or the use of RES to produce thermal energy and domestic hot water. The different value of EP_{DHW} in "EX ANTE STD" and "EX ANTE TR" is due to the number of occupants and the correction of the number of heating days.

The most adequate thickness of insulating material was chosen considering the specific technical requirements, reported in Annex 1 of the Ministerial Decree 28 December 2012 and defining the limit values to access national incentives. The supporting measures provide different thresholds, depending on the climatic zone (tables 9 and 10).

Scenario	Description	EP_{DHW}	EP_{W}	EP_{GL}	EPC
EX ANTE STD		3,146	35,356	38,502	G
EX ANTE TR		2,28	27,003	29,285	G
ESO 1 TR	8 cm insulating material	2,28	19,057	21,338	F
ESO 2 TR	10 cm insulating material	2,28	18,710	20,992	F
ESO 3 TR	12 cm insulating material	2,28	18,466	20,748	F

Table 8: Energy class of the building.

Climatic area	Opaque enclosures
A	U ≤ 0,45 W/m² K
B	U ≤ 0,34 W/m² K
C	U ≤ 0,28 W/m² K
D	U ≤ 0,24 W/m² K
E	U ≤ 0,23 W/m² K
F	U ≤ 0,22 W/m² K

Table 9: Energy class of the building.

ESO	Thermal transmittance	Limit value according to Ministerial Decree 28 December 2012
ESO 1	0, 299 W/m² K	0,28 W/m² K
ESO 2	0,249 W/m² K	0,28 W/m² K
ESO 3	0,214 W/m² K	0,28 W/m² K

Table 10: Comparison between the thermal transmittance of the ESOs with the limit values (climatic area: C).

Since ESO 1 does not comply with the mandatory limit value, this solution cannot be taken into account as a feasible option to access incentives and to improve the thermal behaviour of the existing building. Moreover, it can be easily seen in table 10 that U in ESO 2 is less than the limit value for thermal transmittance of opaque enclosures, hence representing a possible solution. However, although ESO 2 reduces the thermal transmittance up to 83% if compared with the current situation, whereas ESO 3 reaches a decrease of 95%, the latter can be neglected because of economic reasons. Indeed, a smaller thickness leads to major cost savings. The thermal conductivity of the material in ESO 2 is equal to 0,036 W/m/K.

3.3.3 The simulation in Comsol Multiphysics

In order to better understand how heat transfers affect the specific building envelope, a simulation in Comsol Multiphysics environment was carried out since the software represents an efficient tool facilitating all the steps in the modelling process. The Module Heat Transfer was used and involved the following stages:

- selection of the space dimension, namely 3D for the thermal bridges and 2D for the external wall;
- drawing the geometry of the problem after defining parameters in the Global Definition branch, as shown in table 11. The geometry consists of 5 or 6 domains depending on whether we consider the existing structure (figure 33) or the future improvement by adding the insulation thermal layer (figure 34);
- choice of the material and its thermophysical properties, following table 7;
- selection of the physics, namely heat transfer in solids solving the Eq. (1.7), and definition of the boundary conditions in order to solve the differential equation;
- meshing the control volume, following the physical-controlled mesh with normal size (figure 35);
- results visualization in terms of temperature and maximum and minimum values on the surface.

Parameters	Numerical value	Definition
L_w	0,114 m	width of the external wall
L_pl	0,02 m	width of external and internal plaster
L_lm	0,08 m	width of the limestone/mortar
L_ins	0,1 m	width of the thermal insulation
H_w	0,50 m	height of the wall

Table 11: Parameters in the geometry and boundary conditions.

The simulation was carried out both for winter and summer conditions, with or without the insulation thermal layer, "ante operam" and "post operam" respectively. It involved a vertical section of the external opaque enclosure, as shown in figures 33 and 34.

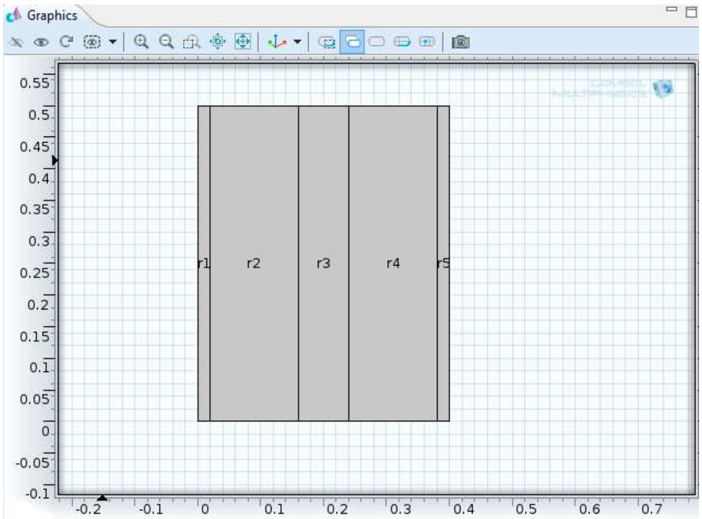

Figure 33: Geometry of the external wall in Comsol Multiphysics (current situation).

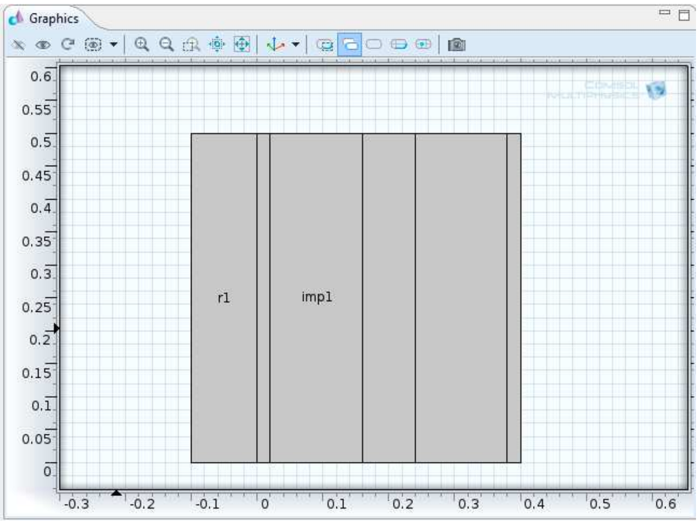

Figure 34: Geometry of the external wall in Comsol Multiphysics when adding an insulation thermal layer.

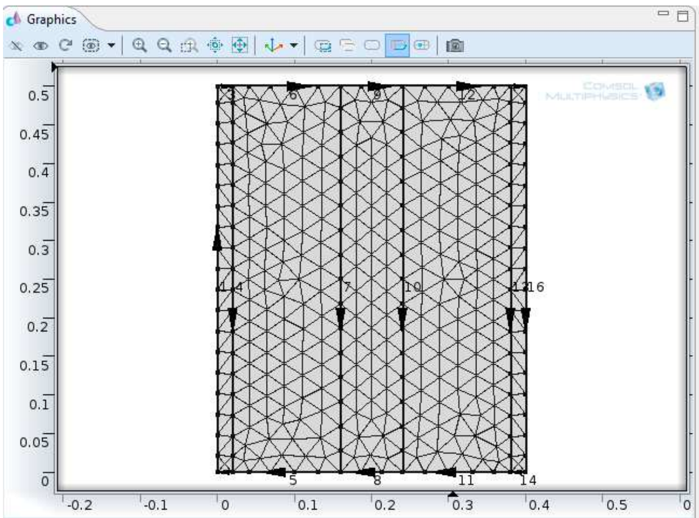

Figure 35: Meshing phase.

With regard to the boundary conditions, the upper and bottom of the wall were considered as "open boundary", thus leading to parallel isothermal contours within the wall. Since the internal and external wall surfaces are both subject to convective motion and thermal radiation, the internal and external convective heat flux and radiative heat flux need to be included, according to UNI EN 6946:2008. The parameter h_ci depends on the direction of the heat flux (horizontal, ascendant or descendant) and h_ce is related to the wind speed which is generally assumed equal to 4 m/s and is calculated as:

$$h\_ce = 4 + 4 \cdot v \tag{3.3}$$

The parameters h_ri, h_re, h_ri_summ, and h_re_summ were evaluated by interpolation and following the values given in table 12:

T_m (°C)	h_r (W/m²/K)
-10	3,72
0	4,16
10	4,63
20	5,14
30	5,69

Table 12: Radiative coefficient according to UNI EN 6946:2008.

Considering the use class of the building and complying with the Presidential Decree 412/93, the set point for the indoor temperature is given by 20 °C in winter and 26 °C during summer. Both values ensure thermal comfort within the built environment. With specific regard to the outdoor conditions, the external air temperature is assumed equal to 2°C in winter according to UNI 5364 and to 33 °C during summer following UNI 10339.

Furthermore, since the thermal behaviour in summer requires the knowledge of the solar radiation during the day, this parameter for the specific location was calculated according to the procedure reported in UNI 10349:

$$I_{\varphi,T} = I_{\varphi,R1} + \frac{I_{\varphi,R2} - I_{\varphi,R1}}{\varphi_{R2} - \varphi_{R1}} \cdot (\varphi - \varphi_{R1}) \tag{3.4}$$

Figure 36 shows the maximum solar radiation pattern for south-oriented surfaces: the maximum value equal to 475,85 W/m² is reached at 12 and is included in the simulation as a "boundary source" in the wall. Because of the thermal solar radiation, the wall itself becomes a heat source, whose power is the maximum solar radiation which is absorbed and transmitted by the internal materials or towards the outside. The maximum value was considered since it represents the most demanding condition for the cooling system.

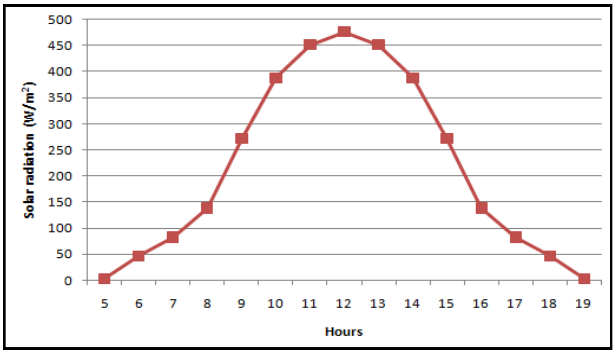

Figure 36: Maximum solar radiation pattern during the day for south-oriented surface.

Parameters	Numerical value	Definition
h_ci	2,5 (W/m²/K)	internal convective heat flux
h_ce	20 (W/m²/K)	external convective heat flux
h_ri_summ	5,47 (W/m²/K)	internal radiative heat flux
h_re_summ	5,69 (W/m²/K)	external radiative heat flux
h_ri	5,14 (W/m²/K)	internal radiative heat flux in winter
h_re	4,25 (W/m²/K)	external radiative heat flux in winter
rad	475 (W/m²)	solar radiation

Table 13: Boundary conditions for solving the differential equation.

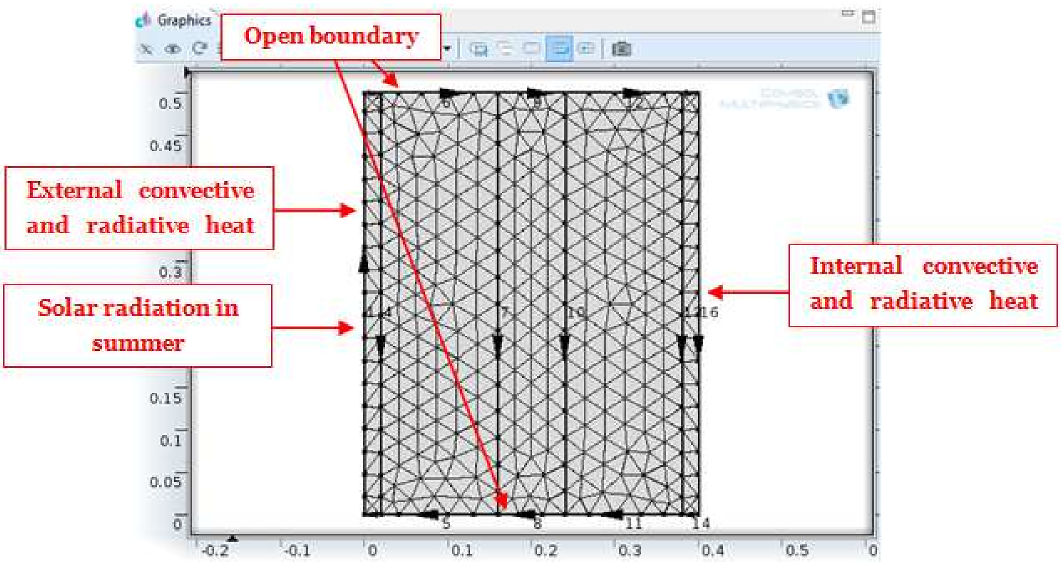

Figure 37:Boundary conditions on the vertical section of the wall.

By default, the differential equations were solved according to the nonlinear method, assuming the minimum damping factor equal to 1e^{-6}. The termination technique followed the tolerance approach, with a maximum number of iterations equal to 50.

Furthermore, the power transmitted through the external wall per unit area was determined with and without the thermal insulation layer following the expression:

$$q_{tr} = U_{tr} \cdot \Delta T \tag{3.5}$$

Thermal bridges and their corrections were also considered in the simulation. According to the International Standard EN ISO 10211:2008, a thermal bridge is a discontinuity regarding the thermo-physical properties of the building envelope, with reference to the thermal resistance, due to material, thickness or shape variation. Their evaluation is crucial because they are enemy number one to almost all measures taken to reduce energy load. They drastically act to reduce the building envelope thermal resistance and hence increase the transmission loads and accordingly jeopardize the beneficial use of thermal insulation [Al-Sanea and Zedan, 2012].

The simulation of the thermal bridges involved a horizontal section of the opaque enclosure.

3.4 Results and discussion

The following graphs show the results given by the simulation in Comsol Multiphysics and describing the phenomenon occurring though the opaque external enclosure: convective motion in the outside and within the internal environment, thermal radiation on the external wall surface heated by the sun during the summer, indoor radiation, and conduction within the wall layers. The simulations were carried out for the cases reported in table 14.

The domain and boundary elements are 644 and 138 respectively in the "ante operam" and reach 796 and 161 in the "post operam". As for the thermal bridges, the mesh consists of 1239 domain elements and 322 boundary elements, reaching 1351 and 370 respectively in the “post operam” calculations. A normal size mesh was chosen in order to speed up the solving time.

Simulation	Description	Solving time
"ante operam_w"	thermal behaviour of the current wall in winter	8 s
"post operam_w"	thermal behaviour of the wall with 10 cm - insulating material in winter	6 s
"ante operam_s"	thermal behaviour of the current wall in summer	4 s
"post operam_s"	thermal behaviour of the wall with 10 cm - insulating material in summer	4 s
"post operam_s_rad"	thermal behaviour of the wall with 10 cm - insulating material in summer in presence of solar radiation	4 s
"ante operam_w_TB"	thermal bridge without correction in winter	8 s
"post operam_w_TB"	thermal bridge with correction in winter	5 s
"ante operam_s_TB"	thermal bridge without correction in summer	8 s
"post operam_s_TB"	thermal bridge with correction in summer	4 s

Table 14: Simulations in Comsol Multiphysics - Heat Transfer Module.

The power transmitted through the wall decreases from 25,794 to 4,482 W/m^2 thank to the thermal transmittance reduction: hence, the insulating material leads to save 82% of the total dispersion towards the outside during the winter.

Figures 38 and 39 show the temperature trend in °C for the current situation and with the insulation layer in winter: it can be seen that the temperature on the interior wall surface reaches a higher value (19,3401 °C) in presence of the insulating material than in the current situation (17,0280 °C). This is due to the fact that a lower heat dispersion from the inside to the outside occurs, thus affecting the temperature values of the external and internal wall surface. The former indeed passes from 2,93634 °C in the "ante operam" to 2,20789 °C in the "post operam": the insulating thermal material in figure 39 acts as a barrier against the heat loss, leading to a colder external wall surface which is not heated anymore from the inside.

Moreover, the temperature of the internal wall surface in figure 39 is closer to the air temperature to ensure occupants' thermal comfort, i.e. 20°C in winter.

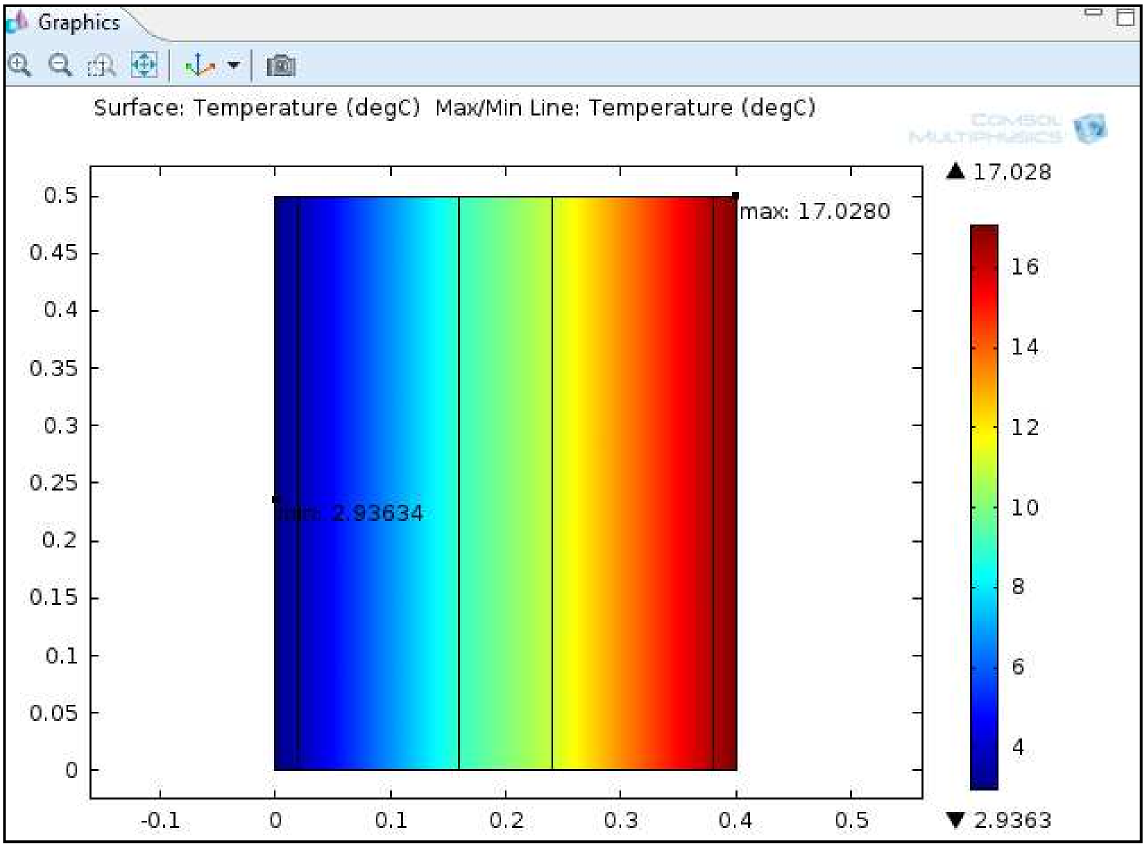

Figure 38: Temperature trend in °C for "ante operam_w".

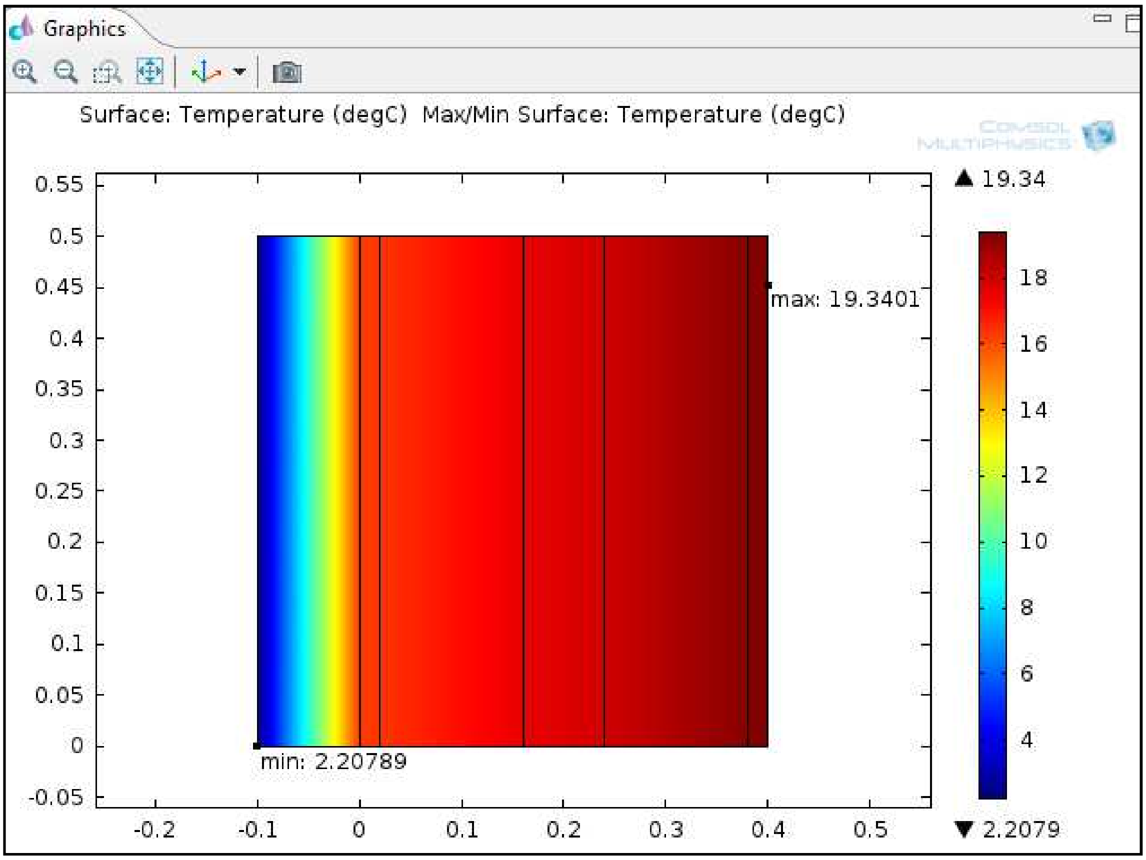

Figure 39: Temperature trend in °C for "post operam_w".

According to ASHRAE, the thermal comfort, that is the condition of the mind in which satisfaction is expressed with the thermal environment, depends on six primary factors: Air Temperature (AT), humidity, air velocity, Mean Radiant Temperature (MRT), clothing level, and metabolic rate. AT and MRT play a fundamental role since they influence the value of the Operative Temperature (OT), which can be calculated as the mean of these temperatures.

According to ASHRAE, MRT is defined as the uniform surface temperature of an imaginary enclosure with which man exchanges the same radiation as in the actual environment. It can be calculated as the weighted average of the surface temperatures of the surroundings, including floor and roof, namely the surface temperature multiplied by the wall area. As a consequence, if the surface temperature of the interior wall increases, MRT, and hence OT, grows, thus reaching a closer value to the comfort zone (figure 40).

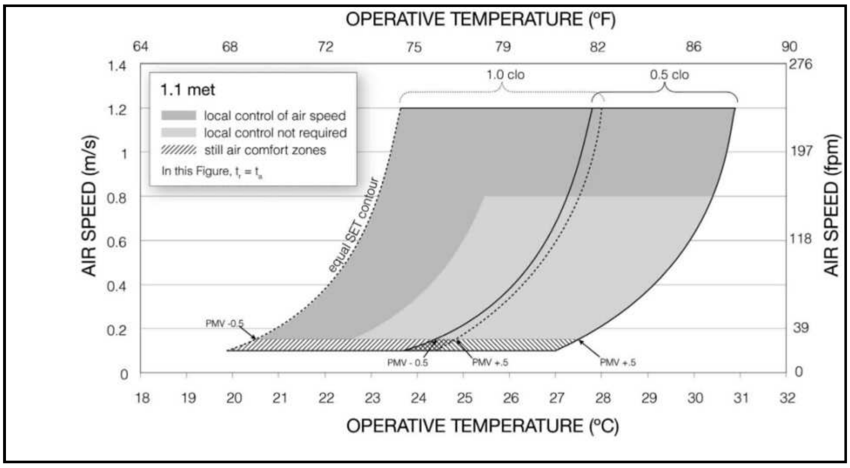

Figure 40: Acceptable range of OT and air speeds for the comfort zone according to Standard 55-2010.

Then, the thermal behaviour of the external wall during the summer is reported (figures 41, 42, and 43). The presence of the external insulation leads to a lower temperature value in the inside (26,2465 °C) than the one in current situation (27,1188 °C). This is due to the fact that the insulating layer reduces the heat penetration though the wall. Moreover, the thermal behaviour is analysed with or without the contribute of solar radiation, in figures 42 and 43 respectively. In case of solar radiation and considering a medium-toned external plaster, the exterior surface reaches 56,3198 °C, thus shifting the temperature value of the interior up to 27,0796 °C.

It has to be noted that solar radiation is considered in the simulation only in summer conditions: in winter indeed, it would cause higher temperatures on the interior wall surface, thus ensuring more thermal comfort than in its absence. The present research investigates the most demanding situation.

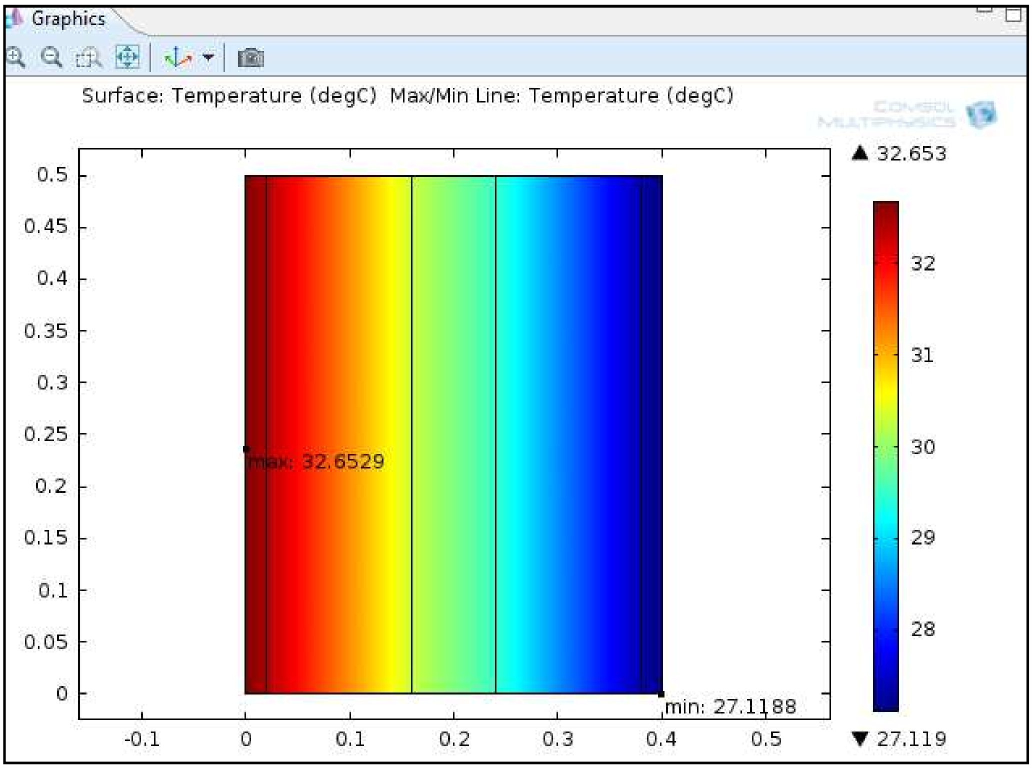

Figure 41: Temperature trend in °C for "ante operam_s".

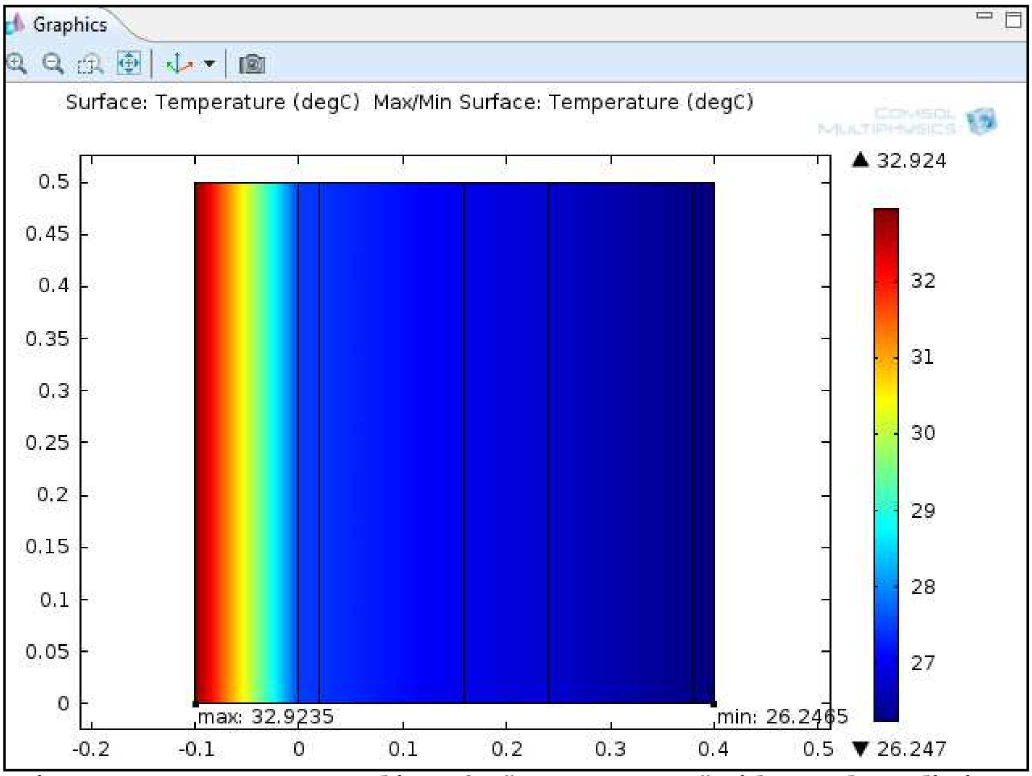

Figure 42: Temperature trend in °C for "post operam_s" without solar radiation.

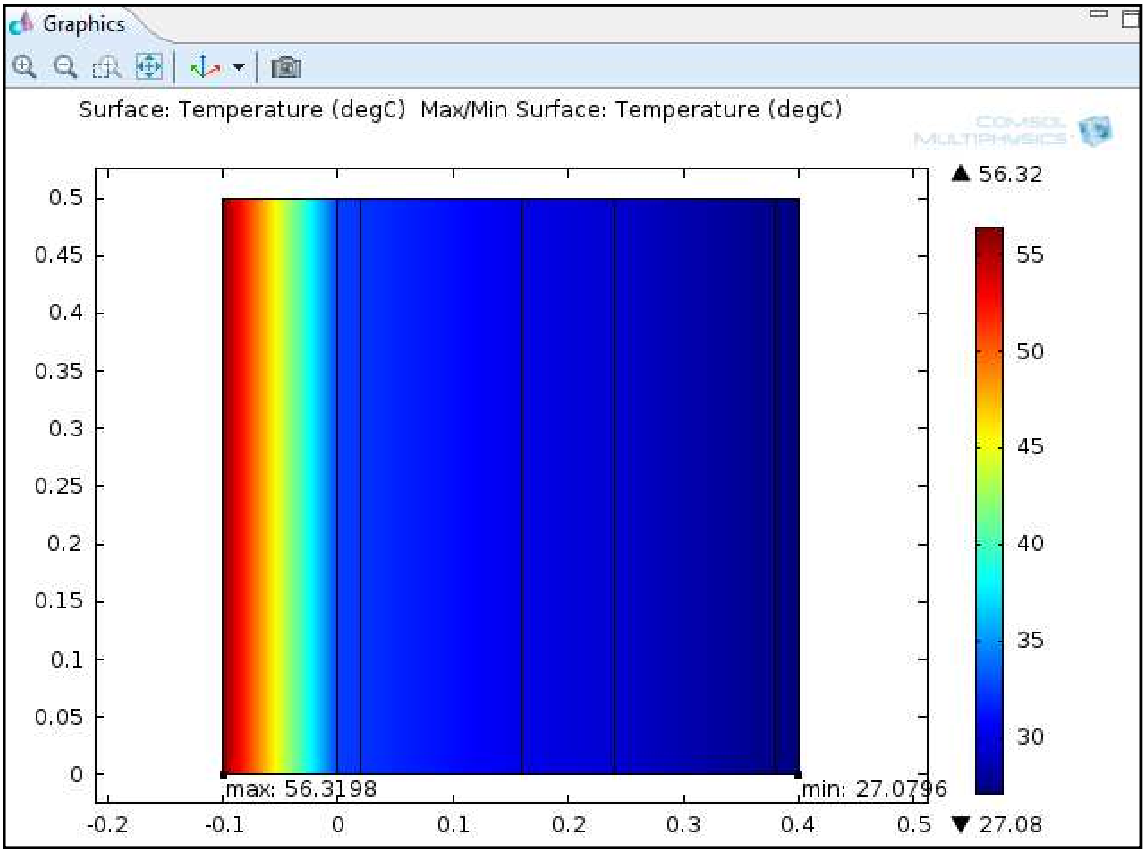

Figure 43: Temperature trend in °C for "post operam_s_rad" in presence of solar radiation.

Figures 44-47 show the temperature trend for a specific type of thermal bridge, that is concrete corner pillar between the external walls. The correction of thermal bridge is carried out by surrounding the corner pillar with insulating material, thus reducing the thermal transmittance. Although condensation effects in mild Mediterranean thermal bridges are limited if compared with those of continental Europe, their correction is still important to reduce winter heat losses and summer heat gains [Evola et *al.*, 2011].

In winter (figures 44 and 45) the maximum temperature value on the interior wall surface is 17,0377 °C in the current situation and 19,2389 °C with the thermal insulation layer. The indoor coldest point is in the corner and passes from 12,810 °C up to 18,006 °C.

As in Theodosiou and Papadopoulos (2011), thermal bridges effects on the cooling load seem to be negligible since the temperature value in the interior corner (28,6641 °C) in the current situation does not strongly vary if compared with the value reached in presence of correction, equal to 26,7958 °C (figures 46 and 47).

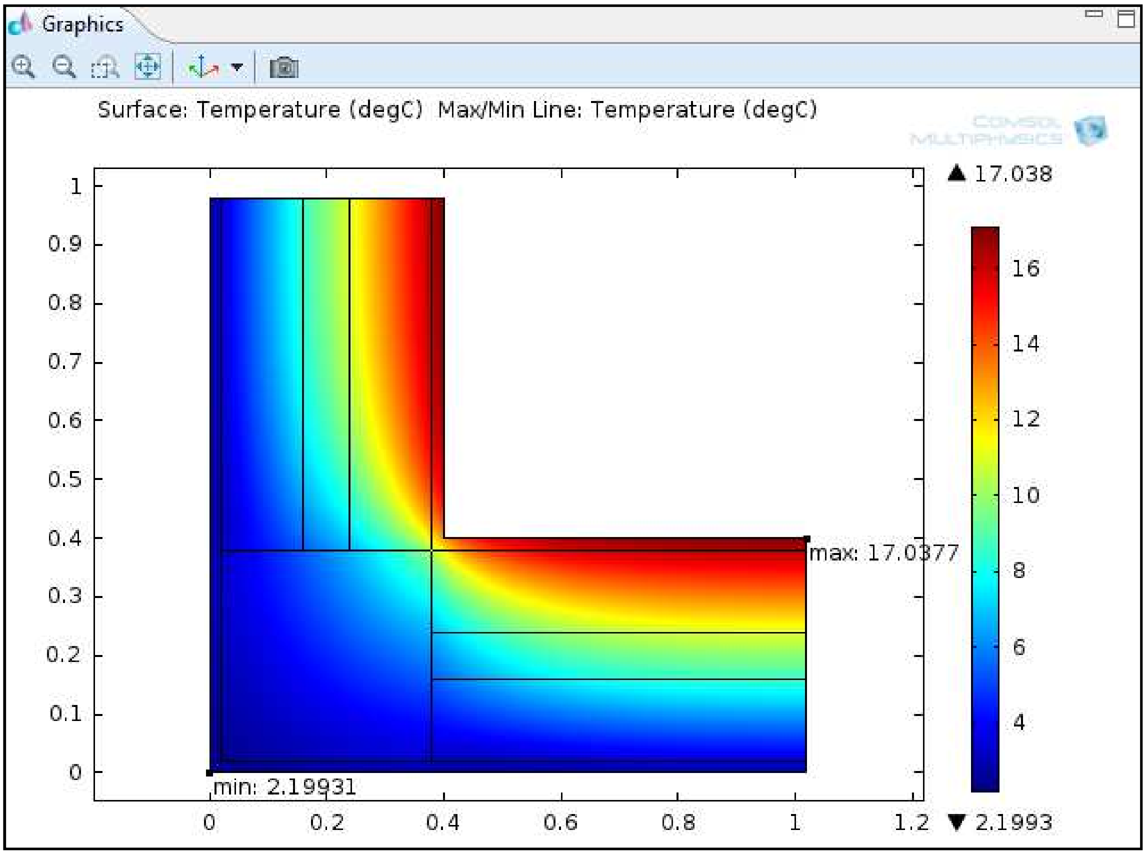

Figure 44: Temperature trend in °C for "ante operam_w_TB".

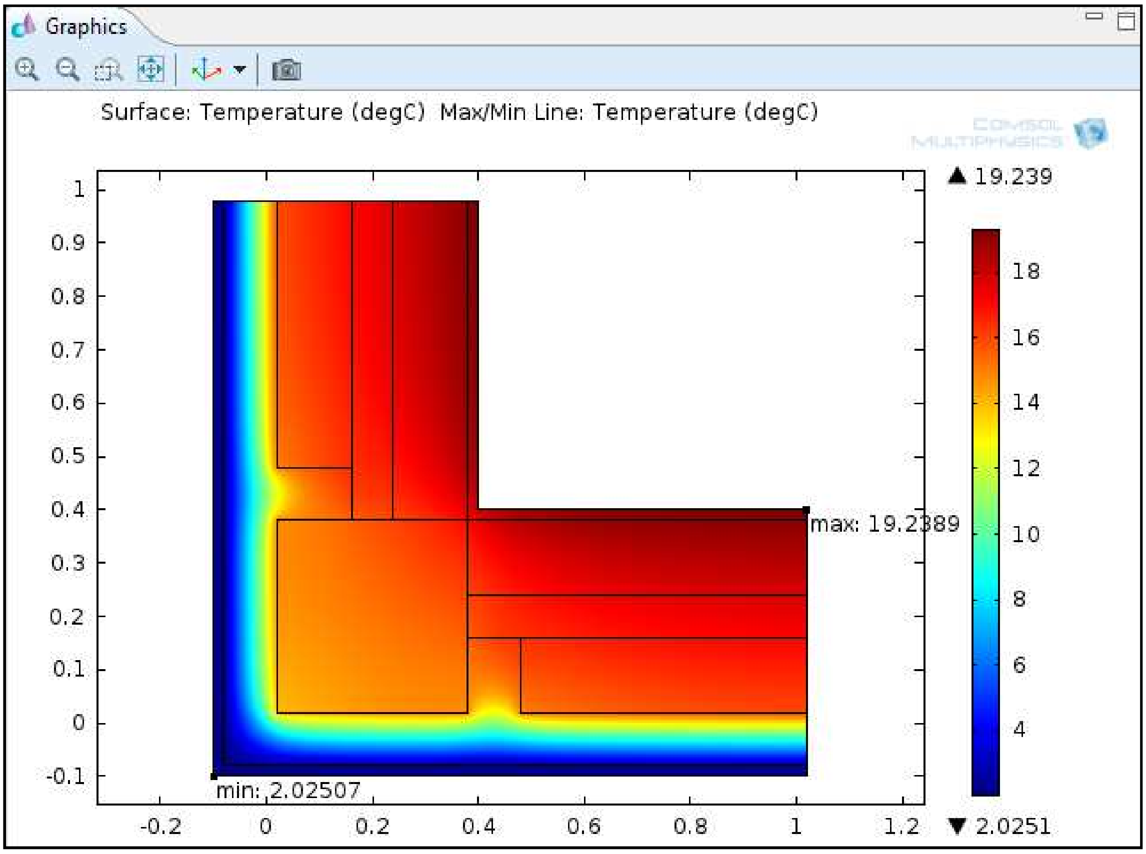

Figure 45: Temperature trend in °C for "post operam_w_TB".

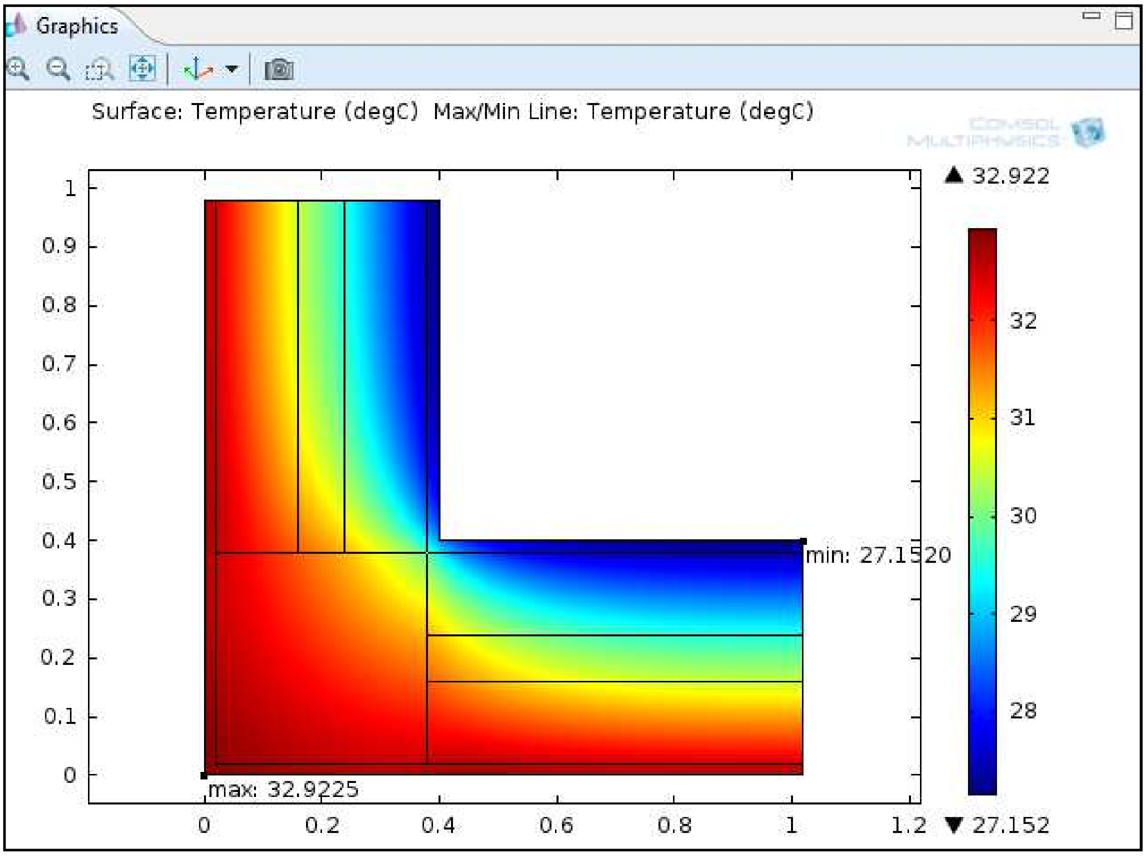

Figure 46: Temperature trend in °C for "ante operam_s_TB".

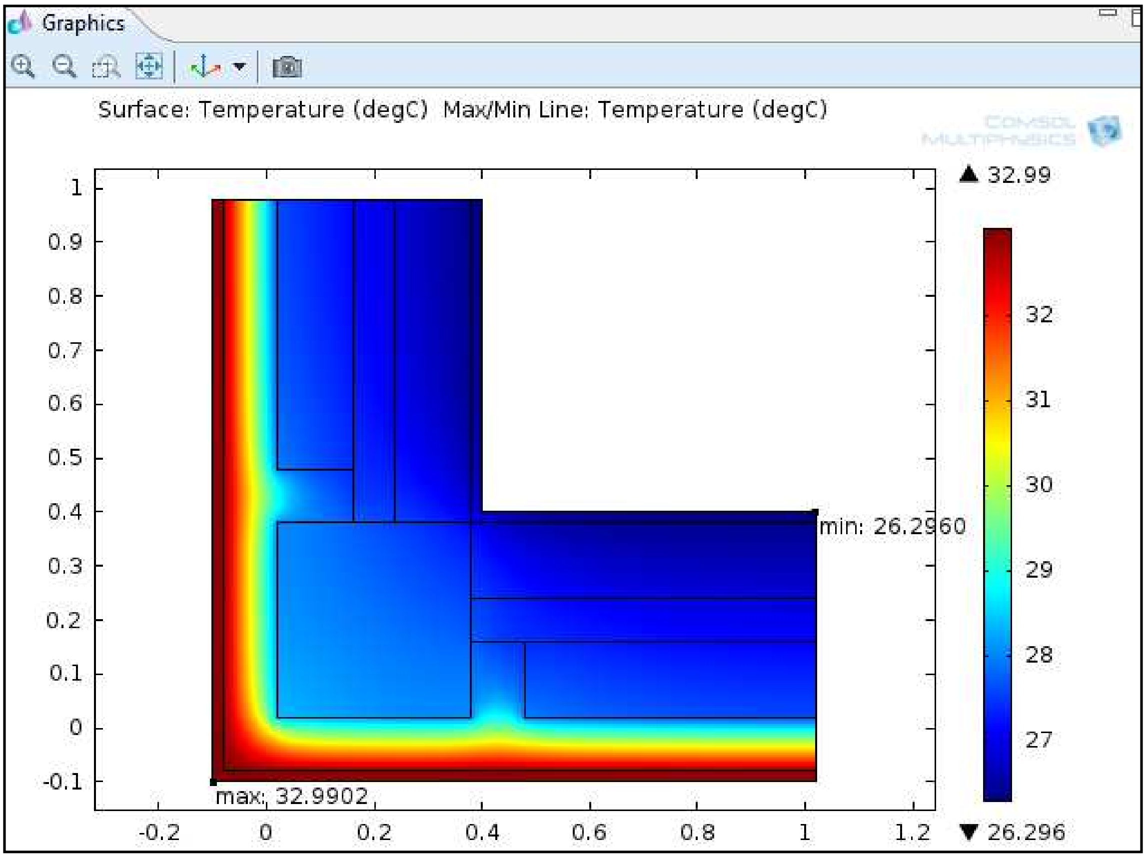

Figure 47: Temperature trend in °C for "post operam_s_TB".

3.5 Conclusion

The investigation presented the possible retrofitting actions on opaque enclosures and thermal bridges for an existing public building located in Italy. EER on the specific public building involves the use of 10 cm-insulating thermal material and leads to reduce the global energy performance indicator for winter heating up to 45% if compared with a standard building use or 28% if we considered the tailored rating approach. This is due to the thermal transmittance reduction, passing from 1,433 to 0,249 W/m²/K.

In order to better understand how heat transfers and the decrease of heat losses affect the building envelope, a simulation in Comsol Multiphysics environment was carried out. The software proved to be an efficient tool facilitating all the steps in the modelling process and having extremely limited solving times and thus avoiding complex hand calculations. Since the simulation was based on the use of parameters defining the geometry and boundary conditions, different case studies –including change of materials, different latitudes, others geometries- may be easily implemented by simply varying those values.

Moreover, the results of the simulation strongly confirm that the insulation cover improves the energy efficiency and the thermal behaviour of the building. Actually, because of the presence of the insulating layer, the interior wall temperature surface reaches a higher value during the winter, ensuring more thermal comfort for the occupants. In summer, the opposite situation occurs, thus reducing the heat gains from the outside and the cooling load.

Besides, the use of a thermal insulating material helps to correct or eliminate thermal bridges, leading to higher temperatures in those parts of corner pillars where condensation or mould may be generated. The temperature increase in the investigated corner has a considerable value in winter, while during the summer it is more limited.

Although the thermal bridges correction is not a profitable practice from an economic point of view as demonstrated in Evola et *al.* (2011) for the mild Mediterranean climate, interesting energy results may be achieved both in winter and summer, decreasing the annual heating and cooling demand.

CHAPTER 4
CASE STUDY 3: IR THERMOGRAPHY FOR GLASSES THERMAL BEHAVIOUR

4.1 Aim of the investigation

From a thermal point of view, windows are considered to be one of the most fragile areas in buildings between the inside and outside. They are integrated within the building envelope, transmitting light and providing a lower resistance to heat flux if compared to opaque enclosures [Catalina *et al.*, 2008; Gloriant *et al.*, 2014].

Nowadays double-glazed windows are the most commonly systems in existing buildings and their energy efficiency is often improved by simply using low-emission coating which reduces radiation heat losses [Mohelnikova, 2009; Gloriant et *al.*, 2014]. Another interesting technical solution is filling the gap between the panes of glasses with absorbing gases, such as Argon instead of air [Ismail et *al*, 2009; Gloriant et *al.*, 2014]. However, researchers and industry are investigating many innovative systems in order to improve the window energy efficiency, such as the use of transparent fins in the gap between the panes in double glazed solutions. This is to limit the convective motion, thus reducing the heat transfer occurring through the window. The ideal window should preserve thermal comfort and hence its thermal performance plays an important role in the building energy consumption [Giorgi *et al.*, 2011; Gloriant *et al.*, 2015].

Since the exact type of window is not known in most existing buildings, the present research investigates the use of active IR thermography -i.e. heating the glass surface- to identify a specific glass, without dismounting it and thus avoiding its breakage or removal. This goal is reached by testing five common glasses and analysing the experimental results in ThermaCAM, both during the glass heating and cooling phase. Then, the glass thermal behaviour is reproduced in FDS and the software output is compared with the IR recorded sequences.

The research activity was carried out during the spring semester, from February to May 2014, at the Institute of Energy Engineering of the Polytechnic University of Valencia, under the guidance of Prof. Rafael Pastor Royo and Prof.

Carolina Aparicio Fernández, and in collaboration with Mr. Eduardo Loma-Ossorio Blanch and Miss Emilie Durrey.

4.2 Introduction: fundamentals on infrared thermal imaging

Structural conditions in buildings can be inspected and monitored in order to be properly managed and this phase represents a fundamental part of their life cycle. The useful service life of structure and infrastructure is extending in the last decades due to cultural, social and economic factors: in this scenario, Non-Destructive Techniques (NDT) are particularly suitable since they do not interfere with the state of asset. Most of NDT can easily detect defections at depths varying in the range between 5 and 100 cm [Cannas *et al.*, 2012].

Infrared thermal imaging –which is often briefly referred to as thermography- has grown rapidly in the last years and is evolving in many fields, from science to industry. Nowadays, it is applied both in research and development. It is fast and remote method and is becoming more widely used among other NDT [Vollmer and Möllmann, 2010; Cannas *et al.*, 2012].

Thermography is an excellent example of visualization technique and helps to visualize the “invisible” effects of physical and chemical processes. Since the method gives spatially resolved surface temperature distribution non-intrusively, even when large gradients occur, this technique has become useful in detecting heat losses, missing or damaged thermal insulation in walls, roofs, thermal bridges, air leakages, and source of moisture. IR thermography can also be successfully employed in building diagnostics that is the determination of the thermo-physical properties of the building envelopes, i.e. opaque and transparent enclosures [Vollmer and Möllmann, 2010; Fokaides and Kalogirou, 2011].

In physics, IR radiation can be described as electromagnetic (EM) waves, which are periodic disturbances that progress in space as a function of time. Figure 48 gives an overview of EM waves, ordered according to their wavelength or frequency: this spectrum consists of a great variety of different waves. With regard to IR imaging, only a small range of the IR spectrum is used. The IR radiation typically falls between wavelengths of 2 ÷ 15 μm, which lies between the visible and the microwave parts of the electromagnetic spectrum. Typically three spectral ranges are defined for infrared thermal imaging (figure 48):

- ✓ the longwave (LW) region: 7 μm ÷ 14 μm;
- ✓ the midwave (MW) region: 3 μm ÷ 5 μm;
- ✓ the shortwave (SW) region: 0,9 μm ÷ 1,7 μm.

The use of thermography is limited to these ranges because of considerations concerning the amount of thermal radiation to be expected, the physics of detectors, and the transmission properties of the atmosphere. Commercial cameras are available for the three ranges [Balaras and Argiriou 2002; Vollmer and Möllmann, 2010].

IR cameras transform the thermal energy radiated from objects in the IR band of the EM spectrum into a visible image where each energy level is represented by a colour or grey level [Cerdeira *et al.*, 2011].

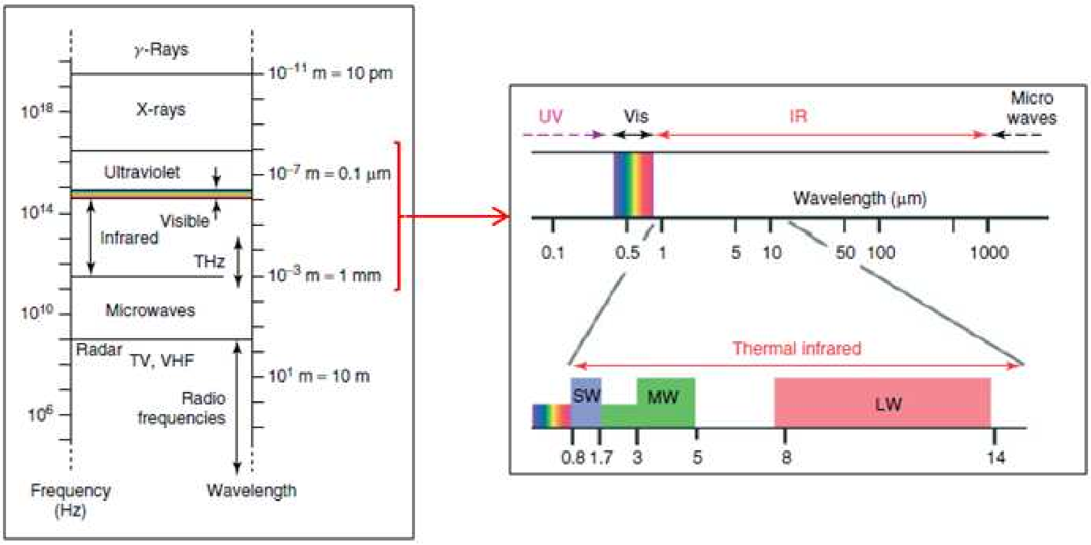

Figure 48: Most common types of EM waves: an overview (on the left) and Infrared and adjacent spectral region (on the right) [Vollmer and Möllmann, 2010].

IR thermography measures the radiant thermal energy distribution emitted from an object's surface, according to the Planck's law. The Stefan-Boltzmann's law converts this radiation into temperature: a precise conversion can be achieved by deeply understanding the various types of heat transfer occurring between object and thermal camera. Figure 49 shows the sketch of the heat transfer processes occurring during a thermographic analysis [Fokaides and Kalogirou, 2011; Asdrubali *et al.*, 2012].

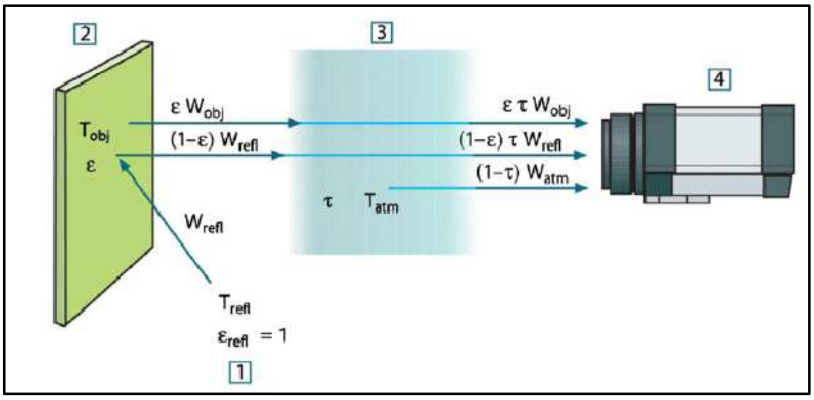

Figure 49: Heat transfer processes in IR thermography [Asdrubali *et al*, 2012].

According to figure 49, the energy balance is given by the following equation:

$$W_{tot} = \varepsilon\tau W_{obj} + (1-\varepsilon)\tau W_{refl} + (1-\tau)W_{atm} \tag{4.1}$$

where W_{refl} depends on the temperature of the objects facing the surface and on the reflective properties of the surface itself. W_{atm} is linked to the air temperature and relative humidity and to the distance between the camera and the surface [Asdrubali *et al.*, 2012].

Assuming that the received radiation power from a blackbody source of temperature on short distance generates a camera output signal that is proportional to the power input by means of a constant, Eq. (4.1) can be rewritten as:

$$U_{obj} = \frac{1}{\varepsilon\tau}U_{tot} - \frac{(1-\varepsilon)}{\varepsilon}U_{refl} - \frac{(1-\tau)}{\varepsilon\tau}U_{atm} \tag{4.2}$$

which is the general measurement formula used in all the FLIR Systems thermographic equipment [FLIR, 2007].

Hence, IR thermography cameras need a series of parameters to take into account, namely object emissivity, reflected temperature, atmosphere temperature, relative humidity, and distance from the object. The emissivity can be determined using black tapes with known emissivity and applying them on the investigated area [Fokaides and Kalogirou, 2011; Asdrubali *et al.*, 2012].

The reflected temperature can be calculated by means of a crumpled piece of aluminium foil fixed on the surface and is given by the average temperature of the foil target, if the IR camera emissivity is set equal to 1 [Asdrubali *et al.*, 2012].

Since the ambient air temperature influences the temperature of the equipment and its performance, an internal compensation is provided. Moreover, it may interfere with the amount of IR radiation emitted from the surface: for example, at very high or extremely low temperatures, IR detection systems become less stable. The phenomenon can also be influenced by wind too: in case of high values, heat transfer from the surface will be enhanced and higher convective heat losses can reduce the surface temperature. Windy conditions should be avoided. Distance effect and the angle of vision also affect data collection since the resolution of the camera decreases with distance. Each point on the thermographic image corresponds to a specific area of the subject surface and hence increasing distance means that each image point must represent a larger surface area. The emitted radiation is averaged and detail is lost. Viewing an object at an acute angle presents less information than one taken at right angles [Balaras and Argiriou 2002].

IR imaging can be divided into two different approaches, depending on whether the inspected area is in thermal equilibrium or not [Vollmer and Möllmann, 2010].

In most applications, the investigation is carried out passively: the camera observes a scene and detects the thermal radiation emitted from the objects. Considering the thermal radiation from the surroundings, a thermal contrast in an image is observed if temperature differences to ambient temperature occur. Thus, the method is called passive, that is the existing temperature distribution of the object scene is analysed without any additional heat flow to the object. Temperatures do not change as a function of time or at least not very much [Vollmer and Möllmann, 2010].

If we consider building inspections, temperature varies due to heating from inside, while the external walls are cooled by the surrounding area. Such passively recorded images may visualize inner structural details of the building itself: surface temperature differences occur because of the spatial variation of the heat flow according to the different thermal properties of the materials or constructions. However, there are situations where temperature differences are not present or are not sufficiently strong or the thickness of the object envelope may be too limited for identifying the structural elements below the surface. In order to detect structural details, active methods are needed. They are based on heating or cooling the surface to be investigated. It is a non-stationary temperature gradient inside the structure, affecting the observable surface temperature distributions [Vollmer and Möllmann, 2010].

As a consequence, active thermography can be seen as a non-steady-state or dynamic thermography. In this case, the transient heat flow on sample surface will causes transient anomalies in the surface temperature distribution [Vollmer and Möllmann, 2010].

4.3 Materials and methods

As aforementioned, the glasses are tested by active IR thermography, that is heating the glass surface by a heater device. The heating and cooling phases are recorded by an IR thermal camera and the sequence is then analysed using the software ThermaCAM.

An IR thermal imager is a device that creates an image of thermal patterns and is calibrated in order to measure the emissive power of surfaces in an area at various temperature ranges. The emitted IR radiation is focused by means of lens into a detector and the electrical response signal is then converted into digital picture. The latter shows different colours corresponding to various temperature levels of the surface. The most commonly used equipment is an IR camera [Balaras and Argiriou 2002].

Several software products can be then used to analyse the thermographic images in the post processing phase, quantifying the differences in temperature. Hence, this technology allows the user to see surface temperatures in any object, resulting from the heat transfer by conduction within the object itself up to its surface, and to assess the amount of radiated heat according to an estimation of its temperature surface [Balaras and Argiriou 2002].

4.3.1 Description of the IR camera FLIR P640

A FLIR thermal camera was employed in the present investigation activity. FLIR Systems was established in 1978 and its activity is concentrated in the design, manufacturing and marketing of thermal imaging systems for a wide variety of commercial and industrial applications. Here are the technical specifications of the model FLIR P640 [Flir, 2007]:

Parameters	Value
Field of view	24 x 18 ° / 0, 3 m
IR resolution	640 x 480 pixels
Spectral range	7, 5 ÷ 13 μm
Thermal sensitivity	55 mK at 30 °C
Object temperature range	-40 ÷ 500 °C
Accuracy	± 2 °C
Operating conditions	-15 ÷ 50 °C
Storage temperature range	-40 ÷ 70 °C
Weight	1,7 kg
Size	120 mm x 145 mm x 220 mm

Table 15: Technical specifications of the camera FLIR P640 [Flir, 2007].

Figure 50 is a detailed image taken from the left view of the thermal camera. (1) represents the infrared lens, whose surface cannot be touched by the user: if this happens while installing or removing them, they need to be cleaned according to the instructions in the user's manual. In order to protect the lens from dust or fingerprints, a lens cap can be used. (2) is the digital camera, whose focus can be adjusted by the user rotating it clockwise or counter-clockwise. The digital camera aperture controls how much light enters the camera itself: in case of low light conditions, it is advisable to increase the aperture. On the opposite, when bright light conditions occur, the aperture should be decreased, leading to a higher aperture number. Note that the aperture can be increased or decreased by rotating the ring clockwise or counter-clockwise respectively if you look at the front of the digital camera lens [Flir, 2007].

The camera has a laser pointer (3): when it is on, an 80 mm- laser dot can be seen above the target. Since the laser beam can cause eye irritation, it cannot be looked directly. The laser pointer can be covered by its protective cap. A laser button (5) has the function to turn on or off the laser pointer: the user needs to push and hold it in the former, or release it in the latter case. The lamp for the digital camera is placed in (4). The user defined button (6) can be configured in order to reach one of the following functions: take a digital photo; switch between current and reference image; switch between colour and grayscale palette; go to the next palette or invert the palette; manual adjust; image gallery. In order to open the display, the release push button (8) needs to be pushed. The viewing angle of the display can be adjusted by the user to make the working position as comfortable as possible [Flir, 2007].

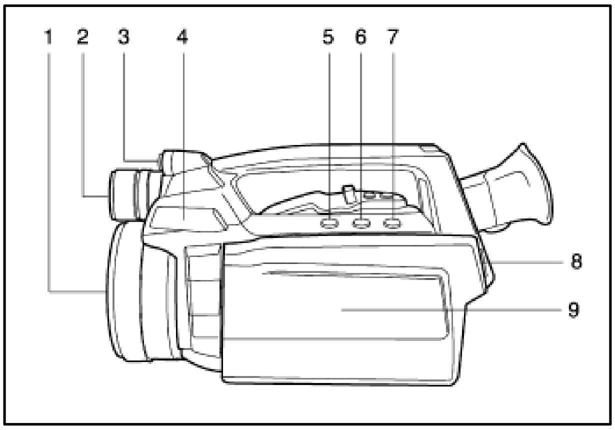

Figure 50: View of the thermal camera from the left [Flir, 2007].

Figure 51 (left) shows the view of the thermal camera from the right. In order to preview or save an image, the button (1) has to be pushed and released: in the second case, the operation needs to last more than one second. The user can preview an IR image or digital photo before saving it to an SD memory card. In the preview mode, the image can be also manipulated. When saving the image, you can specify the folder giving a default work destination [Flir, 2007].

When an image is in live mode, the auto/manual button (2) has the function to switch between auto-adjust and manual mode by pushing it. If an image calibration is required, the button has to be pushed and hold. When an image is in preview or recall mode, the first operation can be carried out. The focus of the image can be adjusted in both cases by means of the focus button (3) [Flir, 2007].

The handle of the camera is represented by (4). Moreover, the angle of the camera grip (7) can be adjusted by simply rotating it clockwise or counter clockwise. (8) is the hand strap in order to work in the most comfortable position [Flir, 2007].

Figure 51 (right) shows the view of the camera from the rear. The components (3), (4), (5), and (6) are the release button for lid to connector compartment, the lid for connector compartment, the lid for the composite video connector, and the lid for power connector respectively. The battery condition LED indicator is placed in (7), while the battery is located in (8). The joystick (12) has the function to navigate in menus and dialog boxes by moving it up/down or left/right, to change values or to select choices [Flir, 2007].

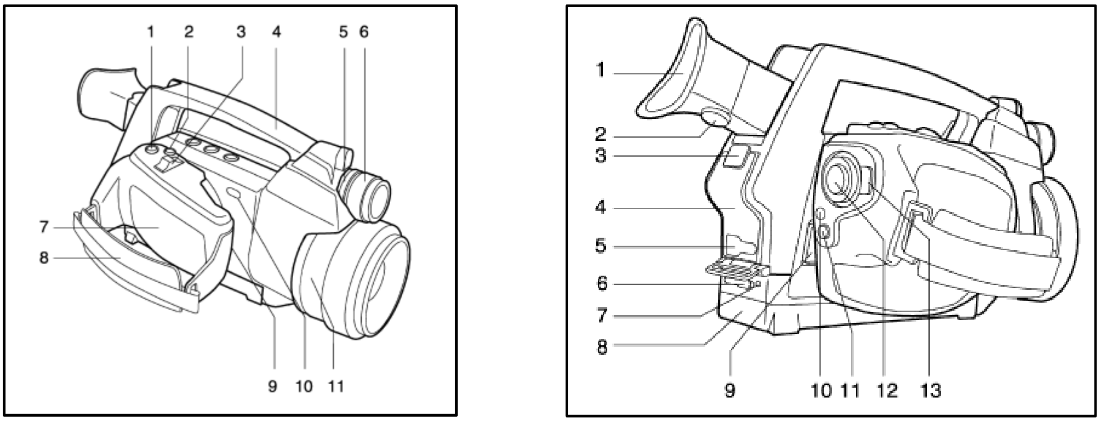

Figure 51: View of the thermal camera from the right (left) and from the rear (right) [Flir, 2007].

The mode selector includes (figure 52):

- ✓ the camera mode to analyse and save IR images (1);
- ✓ the archive mode to view saved images and video clips (2);
- ✓ the program mode to save images automatically (3);
- ✓ the setup mode to set up the camera (4);
- ✓ the video mode to record non radiometric video clips (5);
- ✓ the sequence mode to record radiometric IR sequences (6);
- ✓ information mode (7).

To go to the mode selector, the Mode button to the right of the joystick needs to be pushed.

Toolbox, indicators and important features are shown in figure 53 (left). (1) and (2) are the mode and image mode indicator respectively, while (3) and (4) are the toolbox tabs and toolbox of the image. The general information field is located in (5); the SD memory card indicator is represented by (6), also showing the amount of free space on it. As a warning, the indicator will turn yellow and then red as the amount of free space decreases. (7) is the system time and (8) is the power indicator. (10) is system date the camera uses [Flir, 2007].

Several external devices can be connected to the camera, such as an external USB (1, figure 53, right), a computer in order to move images and files to and from the camera (2, figure 53, right), a computer for recording infrared sequences at high speed (3, figure 53, right), and a video monitor to the camera (4, figure 53, right).

Figure 52: Mode selector [Flir, 2007].

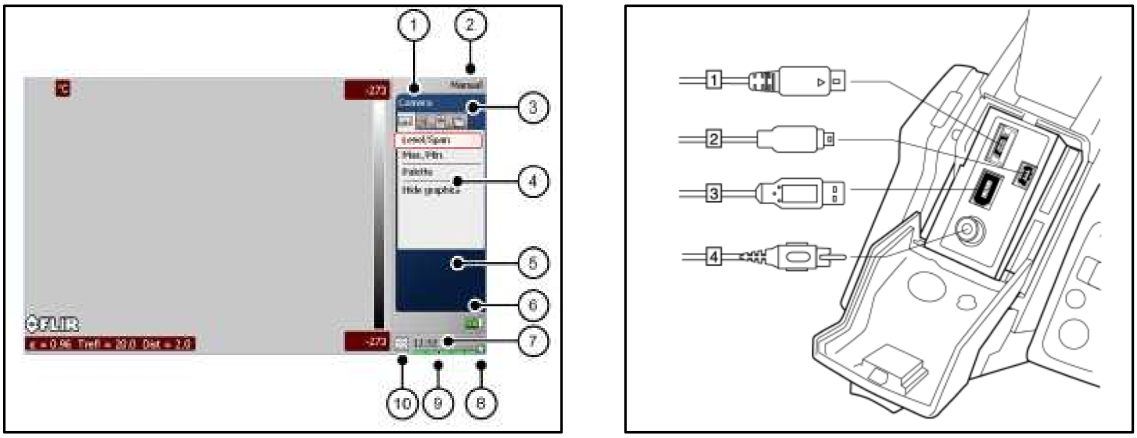

Figure 53: Toolbox and indicators (left) and Connecting devices (right) [Flir, 2007].

4.3.2 The IR images postprocessing: ThermaCAM

The IR images postprocessing is performed by means of ThermaCAM Researcher 2.10 Pro software developed by Flir. It is real-time measurement and analysis software and digitally stores and retrieves static and real-time IR images, live IR digital video sequences, dynamic high speed events and data directly from the FLIR IR camera [www.flir.com].

An extensive temperature analysis can be carried out by the user thank to several measurement functions, including isotherms, spot, line and area measurements, and custom formulas. Moreover, line profiles and histogram charts can be created. Object parameters, such as emissivity, distance, reflected temperature, can be modified, even after an image or sequence has been stored to disk [Flir, 2007].

Figure 54 is an example of a typical image in ThermaCAM. The toolbar in the upper part (1) allows the user to work within the file by means of the common operations, e.g. to open, save, create, copy and/or print a new or the current session. The element (2) is to have information on the limit temperatures of the scale, namely minimum and maximum temperatures. These values can be varied by simply dragging the indicators in the bar (3). By clicking on the button (4), the scale auto adjustment is activated and the indicators will move to a new position. The rectangle (5) includes the name of the file, and all the buttons to start, stop, pause, and step forward or backward the sequence. The lateral bar (6) allows the user to add a flying spotmeter, a cursor or a line, a box area, a circle or a polygon, and an isotherm. The pan and the zoom button are also available [Flir, 2007].

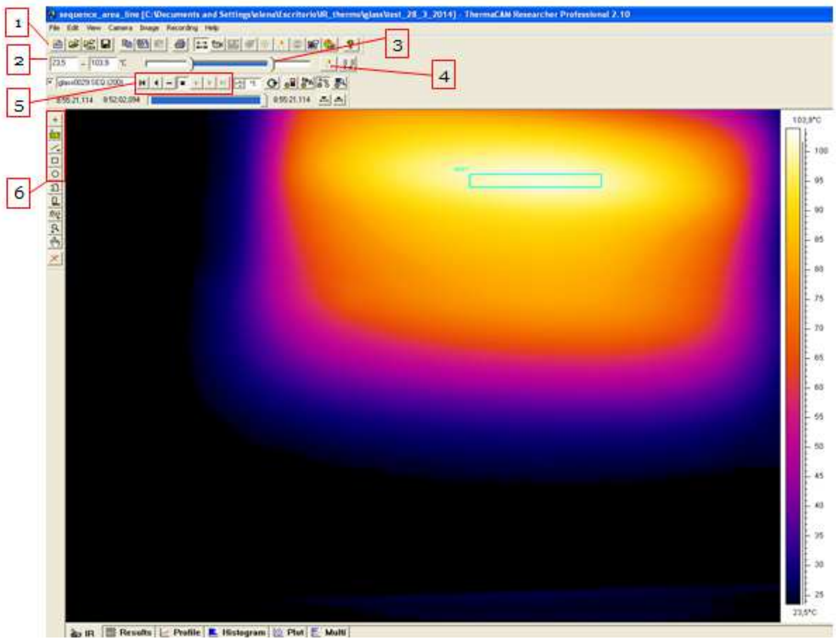

Figure 54: Screenshot in ThermaCAM.

Different settings –such as image, scale, object parameters, analysis, unit and text comment- can be modified by the user, as shown in figure 55: for instance, if "object parameters" is chosen, several properties can be varied, e.g. emissivity, reflected temperature, atmospheric temperature, and relative humidity.

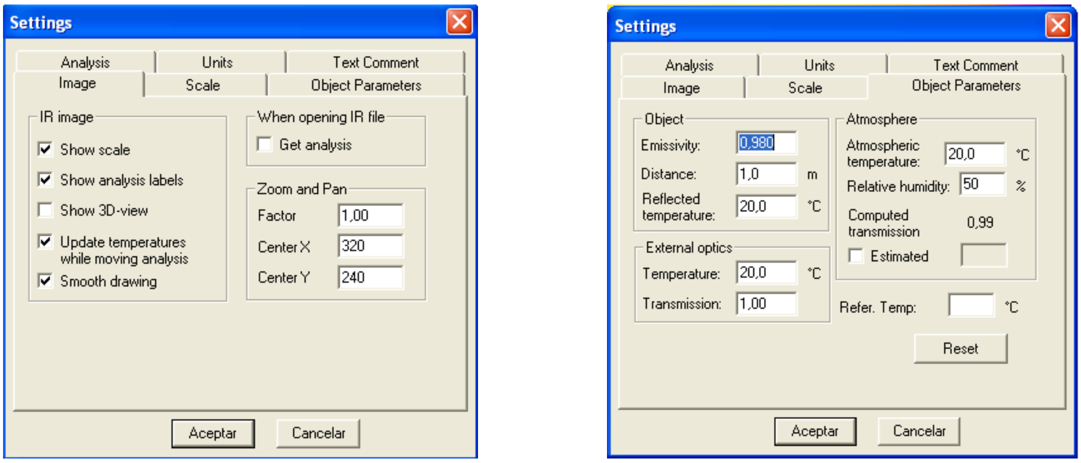

Figure 55: Image settings.

For a single or more spots on the image, a plot function can be added: the temperature pattern in time can be visualised by the user in the Plot box. The data can be saved as .irp (Internet Researcher Project) file and exported into Excel. With regard to box areas or line, several trends can be chosen: minimum, maximum, and average temperatures and minimum and maximum difference in temperature. An example is shown in figure 56 (left). The profile temperature in the spatial coordinate can be visualised in the Profile box (figure 56, right).

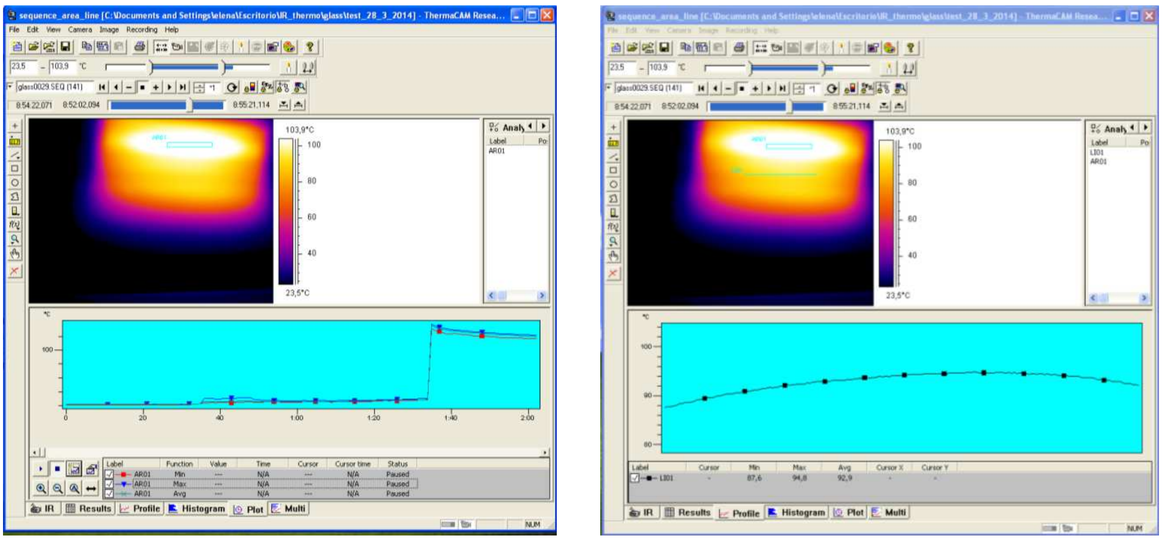

Figure 56: Temperature plot in a box area (left) and along a line (right).

4.3.3 Description of the heater device and glasses

In order to heat the glasses, the heater device shown in figures 57 and 58 is used: its nominal power is 1500 W when the three light bulbs are working. The investigation is aimed at analysing the thermal behaviour of 5 different commercial glasses, which are commonly used in residential buildings in Spain (table 16) and named as "glass" plus a number from 0 up to 4. Glass 0 was bought in a shop in Valencia: no technical information about its thermal properties is available. Glasses 1, 2, 3, and 4 are built by Saint-Gobain and sold in Valencia by Cristaleria Chornet: the most important thermal parameters for glasses 1, 2, 3 and 4, are given in their technical sheet and are calculated by means of the software Calumen II and following EN 410-2011 and 673-2011 standards (table 17).

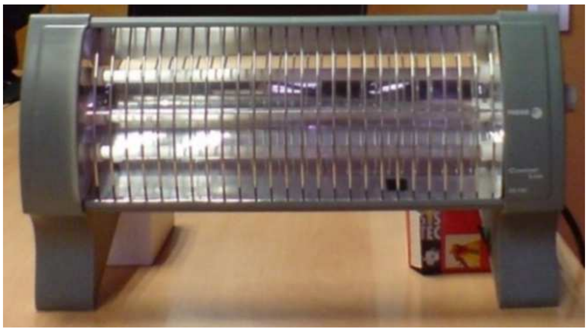

Figure 57: Heater device Fagor, Model CZ 150.

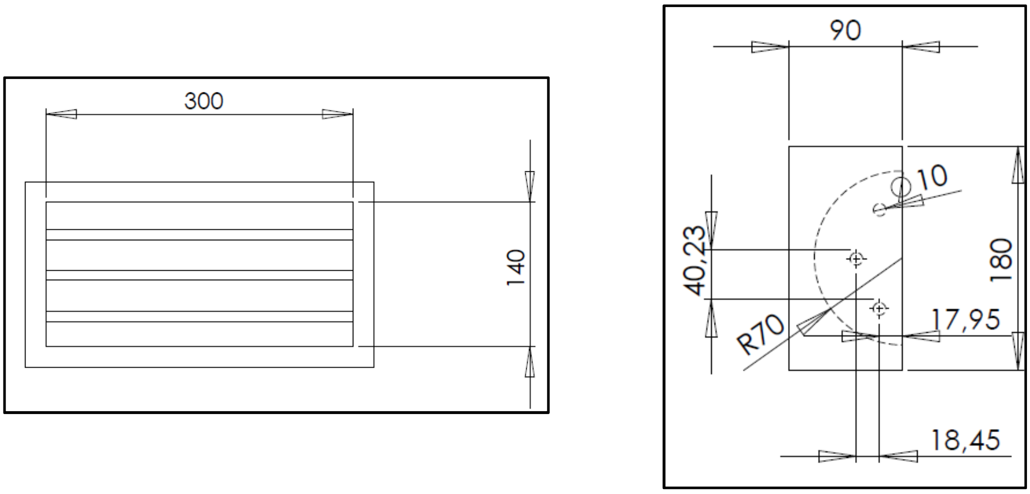

Figure 58: Size of the heater device : frontal (on the left) and lateral (on the right) view (All the dimensions are in mm).

Type of glass	Size (cm x cm)	Width (mm)	Weight (kg/m²)
Glass 0	50 x 50	5	-
Glass 1	50 x 50	4 -12 -4	20
Glass 2	50 x 50	4 -12 -4	20
Glass 3	50 x 50	4 -12 -4	20
Glass 4	50 x 50	4 -12 -4	20

Table 16: Size and weight of the glasses.

Type of glass	1st glass	Gap	2nd glass	Layer	Thermal Transmittance [W/(m² x K)]
Glass 1	Planilux 4 mm	Air	Planilux 4 mm	-	2,8
Glass 2	Planilux 4 mm	Air	Planilux 4 mm	Planitherm Ultra on the 2nd glass	1,6
Glass 3	Planilux 4 mm	Air	Planilux 4 mm	Planitherm 4S on the 1st glass	1,6
Glass 4	Planilux 4 mm	Argon 100%	Planilux 4 mm	Planitherm 4S on the 2nd glass	1,2

Table 17: Glass characteristics.

Figure 59: Glass 0.

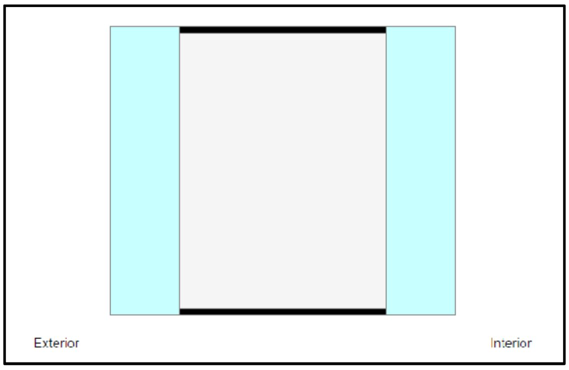

Figure 60: Glass 1 and position of the treated layer.

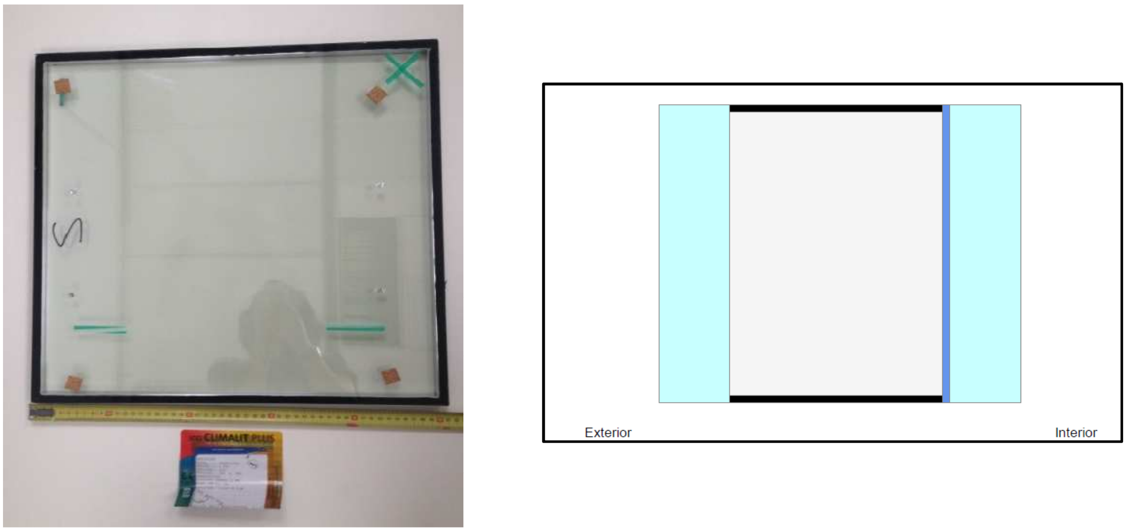

Figure 61: Glass 2 and position of the treated layer.

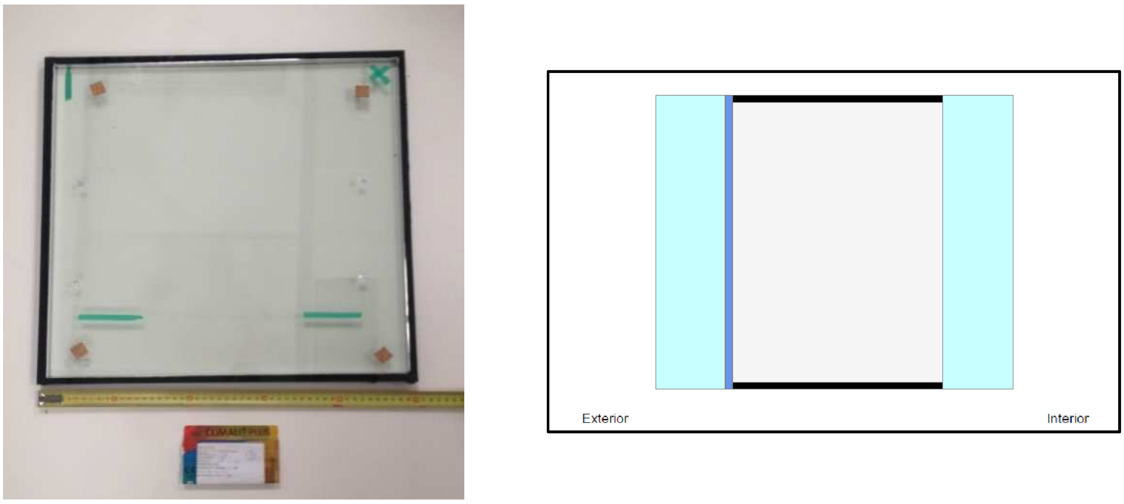

Figure 62: Glass 3 and position of the treated layer.

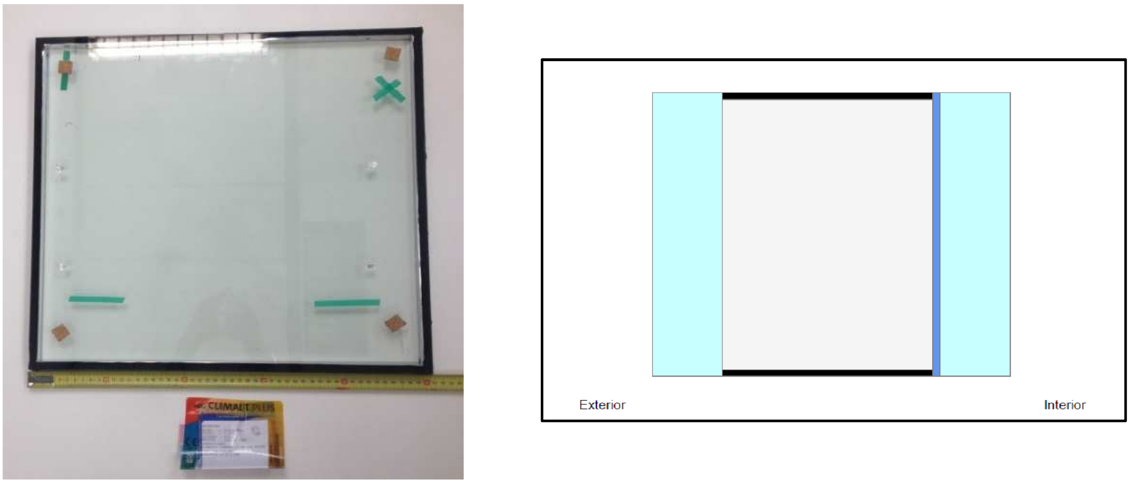

Figure 63: Glass 4 and position of the treated layer.

4.3.4 The first experimental set-up and preliminary results

In the first experimental set-up, the equipment consisted of a thermo-camera, a heater device to heat the glass surface, and the glass to test (figure 64). The tests were carried out in indoor conditions. Both heater and glass were placed on a table, according to two different configurations (figure 65):

- ✓ **C**amera – **G**lass – **H**eater (CGH): the glass is placed between the camera and the heater and is heated on the back side. Since limited temperatures were expected on the glass surface facing the camera, its temperature range was set up to -40 ÷ 120 °C;
- ✓ **C**amera – **H**eater – **G**lass (CHG): the heater is placed between the camera and the glass and the latter is heated on the front side. Since high values of temperature may occur in this case, the temperature range of the camera was set up to 0 ÷ 500 °C.

Figure 64: The first experimental set-up.

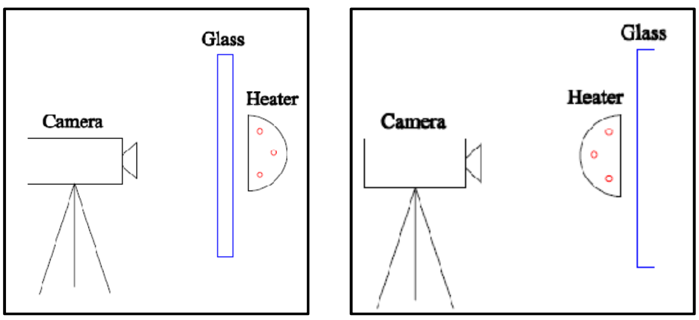

Figure 65: Different configurations of the test: CGH (left) and CHG (right).

Both sides of the glass –with and without a small piece of cork we used as reference, and named as “side a” and “side b” respectively- were tested (figure 66, left): the heating phase lasted 60 seconds for each glass and the recording duration was equal to 200 seconds, in order to appreciate the cooling effects after the heater removal. The steps are listed below:

- ✓ turn on the heater at t = 0 (up to 1500 W, with the three light bulbs on);
- ✓ place the heater close to the glass and wait 60 seconds;
- ✓ remove the heater and continue recording until t = 200 seconds.

Several tests on glasses 1, 2, 3, and 4 were carried during three days, from the 26th to the 28th of March 2014, for both configurations, as shown in table 18. The value entered with (*) means that the glass broke up during the heating phase. This problem occurred for glasses 2 and 4: this is probably due to the fact that the glass was not at environmental conditions and too hot after the previous test. In more detail, glass 2 (**) broke up in the second test (figure 35, right). Glass 0 was tested on the 12th of March 2014 for a shorter heating period (30 seconds) and a limited recording duration that is 119 seconds. Moreover, it was tested on one side, placing the heater on its rear side (CGH configuration) because no difference exists between the two sides of the glass.

Figure 66: Side "a" and "b" of the glass (left) and glass 2 after breaking (right).

Type of glass	Configuration	Sequence name: Side (a)	Sequence name: Side (b)
Glass 1	CGH	0023	0019
	CHG	0033	0028
Glass 2	CGH	0024	0020
	CHG	0031 -(**)	0027
Glass 3	CGH	0026	0021
	CHG	0029	0032
Glass 4	CGH	(*)	0018
	CHG	(*)	(*)

Type of glass	Configuration	Sequence name
Glass 0	CGH	0007

Table 18: Number of tests.

Image code	Heating phase (s)		Recording duration (s)
	Start (s)	**End (s)**	
0007	9	40	119
0018	54	122	124
0019	27	87	200
0020	32	92	200
0021	36	96	200
0023	40	100	201
0024	43	103	200
0026	17	77	200
0027	32	92	200
0028	43	103	200
0029	36	96	200
0031	47	103	186
0032	17	77	200
0033	40	100	200

Table 19: Heating phase and recording duration for glasses 0, 1, 2, 3, and 4.

Here are some preliminary results for glass 0, 1, and 3 describing the temperature pattern within the rectangular area represented in the IR image at the beginning and end of the heating phase. The thermal trend is given for the average, minimum and maximum values within the considered area. If we compare figures

67, 68, and 69, it can be easily seen that the pattern has a different shape depending on the type of configuration we are looking at. Glasses 1 and 3 show a similar trend during the heating and cooling phase. A pick is reached after removing the heater in both cases: this is due to the fact that the heater is placed between the glass and camera and the surface temperatures on the glass cannot be measured during the heating phase. Once we remove it, the camera instantly records the increase in temperature. Glass 0 shows the temperature growth from the beginning since we are testing the configuration CGH. Glasses 2 and 4 are not shown because of their breakage. For sake of synthesis, only results related to side (a) are reported:

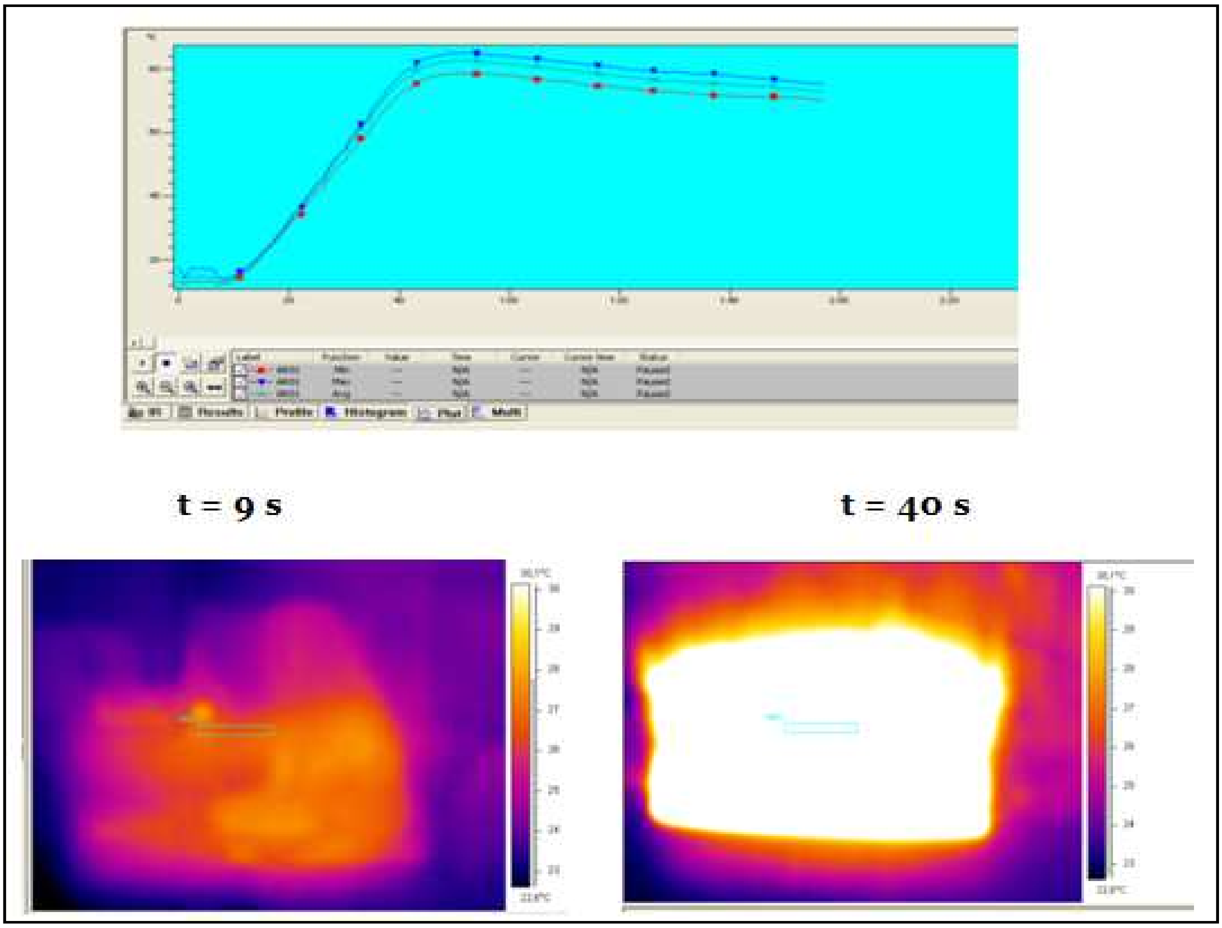

Figure 67: Thermal trend in the rectangular area (minimum, average and maximum values) and IR images at the beginning and end of the heating phase for configuration CGH for Glass 0.

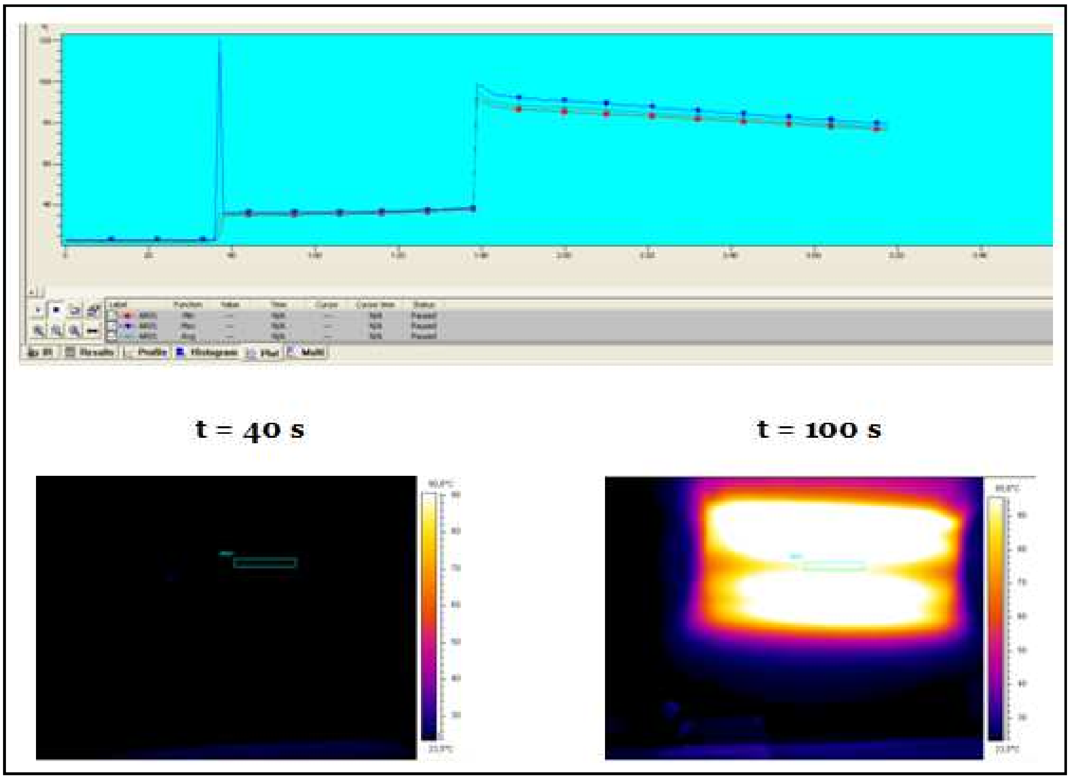

Figure 68: Thermal trend in the rectangular area (minimum, average and maximum values) and IR images at the beginning and end of the heating phase for configuration CHG for Glass 1.

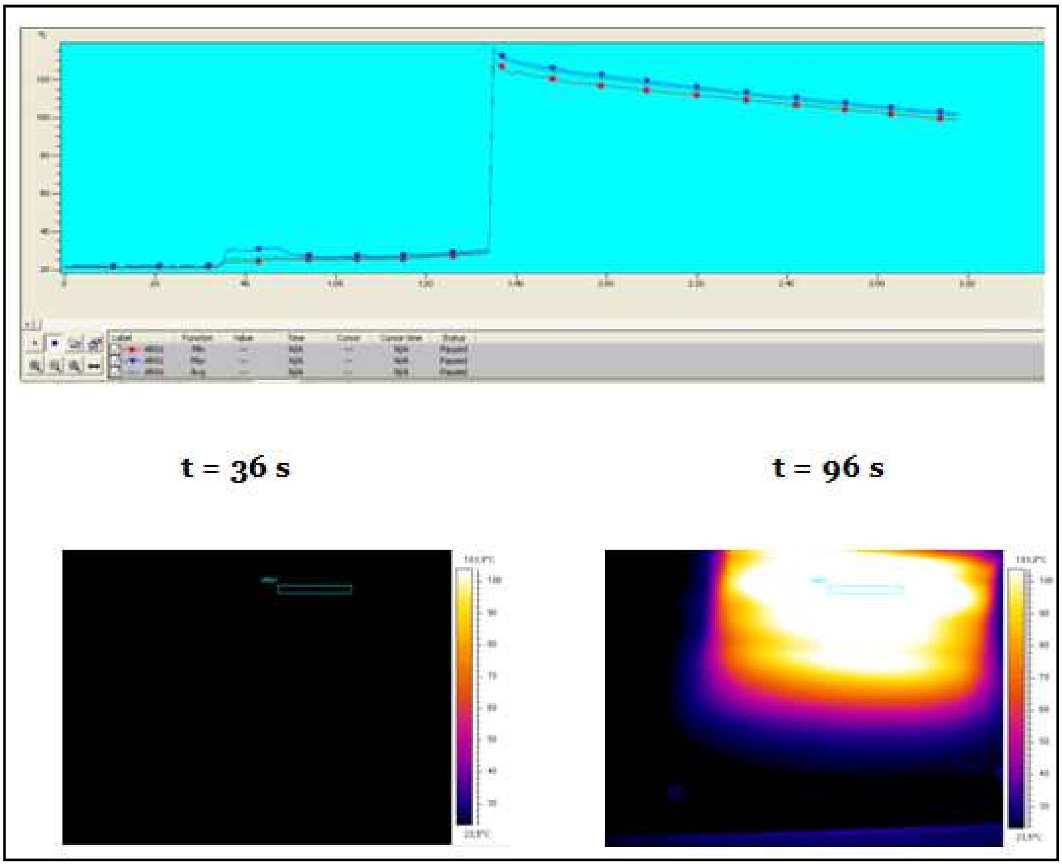

Figure 69: Thermal trend in the rectangular area (minimum, average and maximum values) and IR images at the beginning and end of the heating phase for configuration CHG for Glass 3.

4.3.5 The second experimental set-up

During the tests we carried out in the first experimental set-up, some critical aspects emerged and needed to be carefully improved:

- ✓ the heater was placed in front or on the rear side of the glass manually and did not have any support to ensure its stability during the heating phase. This led to a non-perfect positioning: in some cases the heater was not correctly and horizontally collocated in the centre of the glass, as it can be seen in figures 68 and 69. Moreover, the heater was not always placed in the same position, thus affecting the areas we compared in ThermaCAM. No reference was used to define the heater position on the glass surface;
- ✓ the heater was heated before being located close to the glass: this time was not the same in all the tests. Different temperatures may be reached on the surface, depending on the pre-heating period of the heater itself;
- ✓ the glass was held manually and hence its position was not always vertical and fixed during the glass heating phase;
- ✓ no reference was used to exactly locate the camera at the same position and distance from the heater;
- ✓ the recording duration was limited and could not help to properly analyse the cooling phase. The latter seems to last more than 200 seconds because of the glass capacity to store and slowly release heat.

As a consequence, the above-described procedure was improved in order to obtain more comparable and reliable results, simultaneously reducing errors and uncertainties in evaluating the surface temperature of the glass and some thermal properties to be introduced in the dynamic simulation.

The second experimental set-up is placed in the laboratory of Constructions in the School of Building Engineering, at the Polytechnic University of Valencia. The equipment includes the camera, the heater, and the different glasses (figure 70). Three wooden supports were built in the laboratory of the Energy Engineering Institute: two are used to host the glass (figure 71), while one supports the heater device (figure 72).The supports, the heater, and the glasses are placed on a table during the test. Moreover, the position and distances between the elements of the system are always known thank to a metric tape pasted on the edge of the table (figure 71, left).

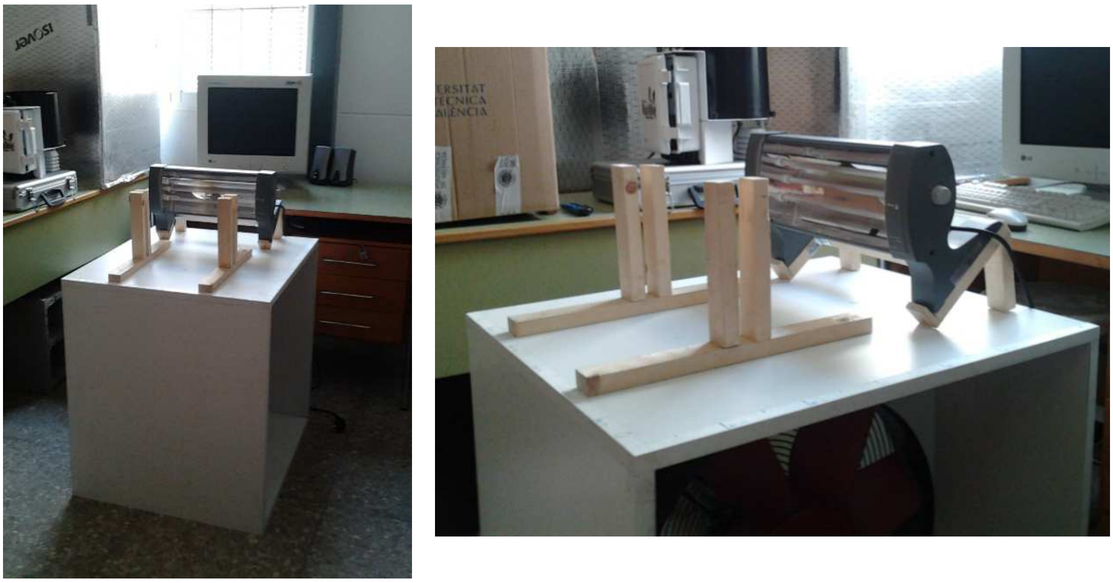

Figure 70: The second experimental set-up: the location.

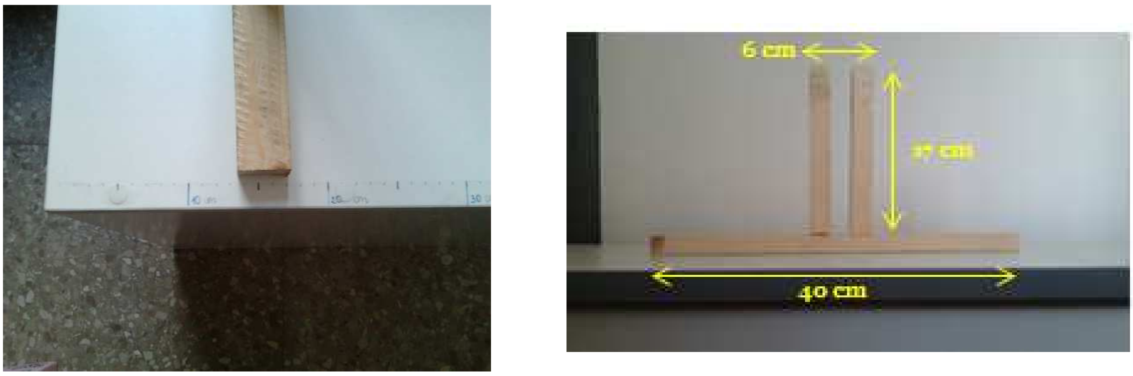

Figure 71: The second experimental set-up: reference on the table (left) and wooden support for glasses (right).

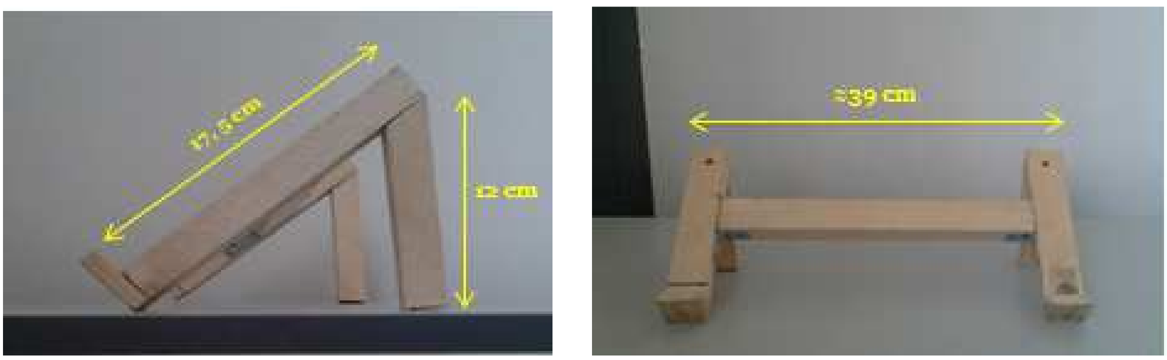

Figure 72: The wooden support for the heater device: front (left) and lateral (right) view.

The camera was equipped with a plastic foil around its lens to avoid surrounding reflections on the glass surface (figure 73), which occurred in some tests, as it can be seen in figure 67 (left). Its position was defined by simply pasting three green sticks on the floor, at the bottom of the tripod (figure 74).

Figure 73: Plastic foil around the camera lens.

Figure 74: Green sticks on the floor.

Two bricks were placed below the heater so that it was always perfectly centred. In order to place all the elements in the same position on the table, reference sticks were used, i.e. green or red ones for the configuration CGH and CHG respectively. The glass sides were distinguished by writing the symbols “X” and “L” on their surfaces. An aluminium foil was located close to the glass during the tests to measure the reflected temperature of the surface (figures 75 and 76).

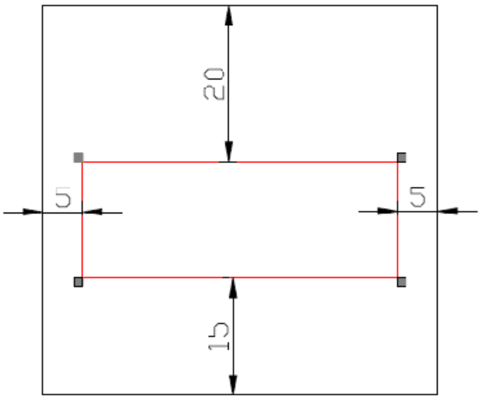

Figure 75: Distance of the heater (red) from the glass edges and aluminum sticks (grey) to define the heater position on the glass surface. All dimensions are in cm.

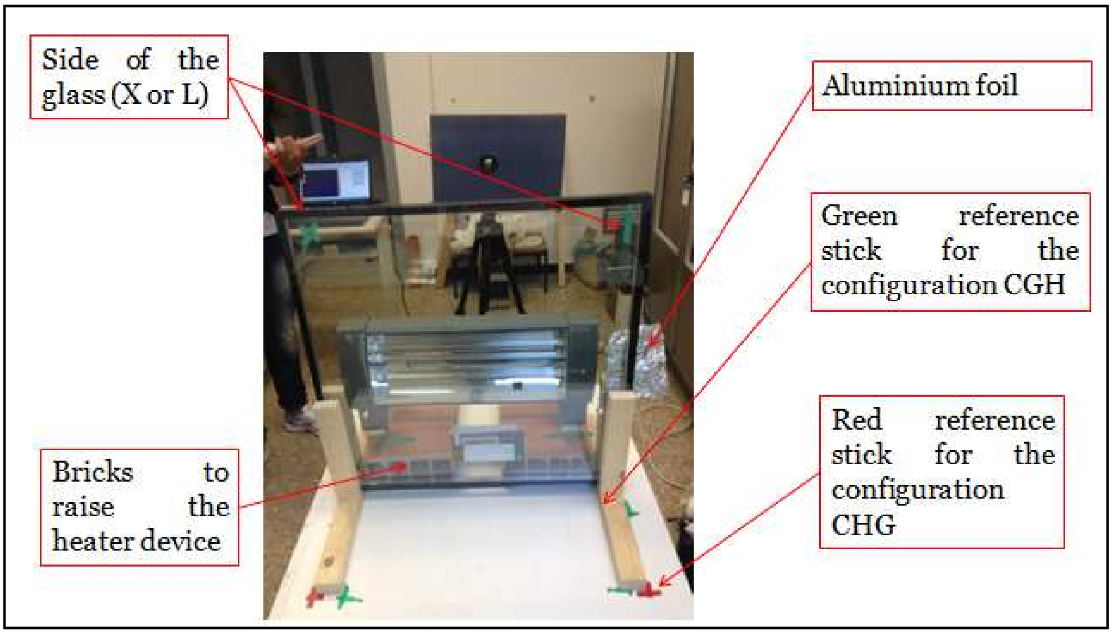

Figure 76: Reference sticks in the second experimental set-up.

The tests followed the below-listed steps:

- ✓ at t =0, the heater is turned on and simultaneously the recording phase starts (the glass is already placed in its correct position);
- ✓ after 10 seconds, the heater is placed in direct contact with the glass and the heating phase lasts 30 seconds;
- ✓ after 30 seconds of heating, the heater is removed and switched off;
- ✓ the recording phase lasts until a number of seconds equal to the sum of 600 seconds plus the time representing the heating phase of the heater (approximately 10 seconds).

Several tests on glasses 0, 1, 2, 3, and 4 were carried during two days, from the 24th to the 25th of April 2015, for both configurations and the IR sequences are named as *daymonth_glassnumberside*. Table 20 shows the details of the test held on the 24th of April for the configuration CGH.

Sequence code	Heating phase		Recording duration (s)
	Start (s)	**End (s)**	
2404_glass0x	12	42	612
2404_glass1x	12	43	613
2404_glass2x	12	43	612
2404_glass3x	13	43	613
2404_glass4x	11	43	605
2404_glass0L	12	42	612
2404_glass1L	12	42	612
2404_glass2L	13	44	613
2404_glass3L	12	44	612
2404_glass4L	12	42	613

Table 20: Tests for glasses 0, 1, 2, 3, and 4 in the CGH configuration (side X and L).

In order to analyse the thermal behaviour of the glass during the heating and cooling phase, two different approaches were used, namely considering points (called *method I*) and a rectangular area (called *method II*) on the glass surface.

According to *method I*, eight spots (SP01, SP02,..., SP08) - approximately every 5 cm- were placed on the glass surface in the IR image in ThermaCAM, defining a line where the temperature trend can be studied during the whole sequence. They are at the same height from the bottom, as it can be seen in the y coordinate of figures 77-81, and are located within the rectangular area delimited by the aluminium sticks, for both sides X and L. Moreover, they are in front of the central light bulb of the heater device. In each spot located on the IR image, the value of temperature is known for each second of the recording phase: thus, the number of temperature values vary from a minimum of 605 for the test 2404_glass4x up to 614 for the test 2504_glass2L . To give an example of the huge number of data, consider the glass 0x and its eight spots: in this case, each spot has 612 temperature values, leading to a total number of 612 x 8, i.e. 4896 values. Similar consideration occurs for the other glasses.

Since a large number of data was available, it was necessary to find a way to compare the different tests on the glasses in one graph. Thus, in each test (which means for each glass), the temperature difference between the current and the initial value for the spot with the highest temperature was calculated every second, defining the thermal pattern during the heating and cooling phase. The position of the spots in every glass is given in figures 77-81 (side X) and the thermal pattern is shown in figure 82. Side L is not reported for sake of synthesis, having the same coordinates of the spots.

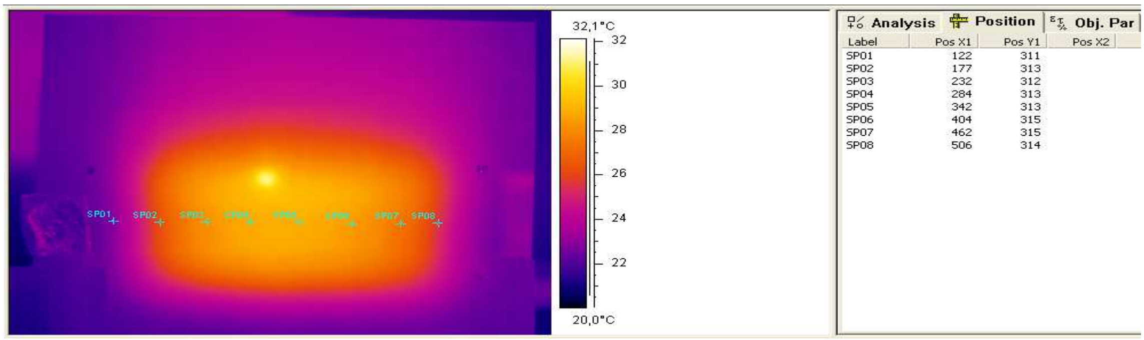

Figure 77: Position of the spots on glass 0 (CGH).

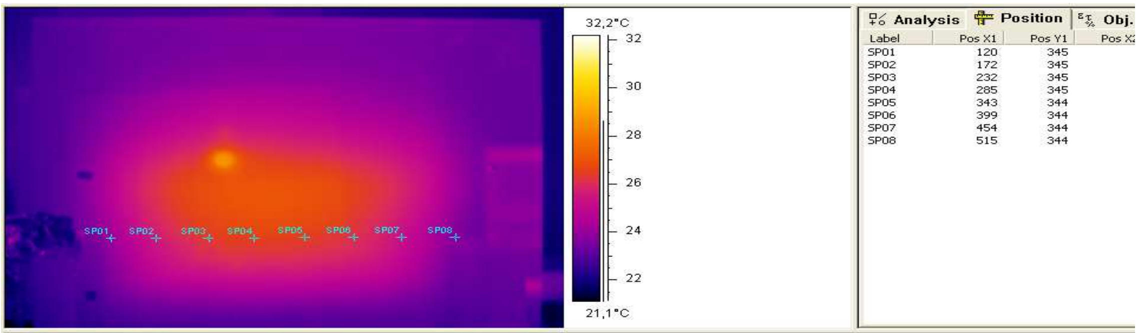

Figure 78: Position of the spots on glass 1 (CGH).

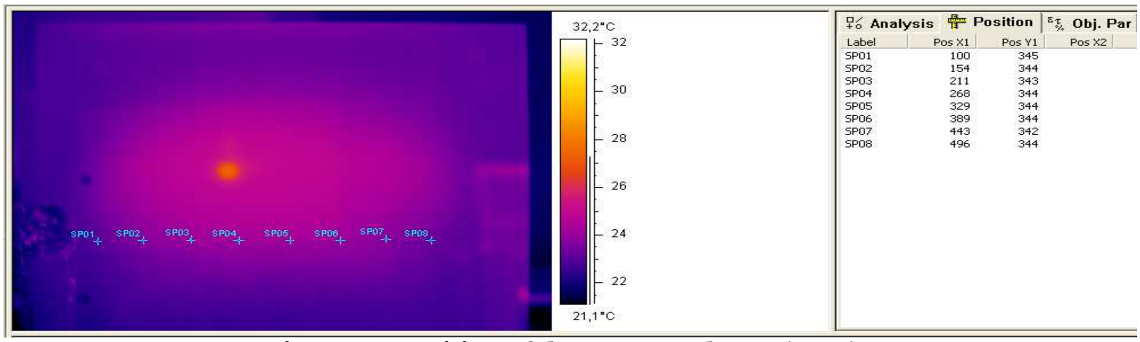

Figure 79: Position of the spots on glass 2 (CGH).

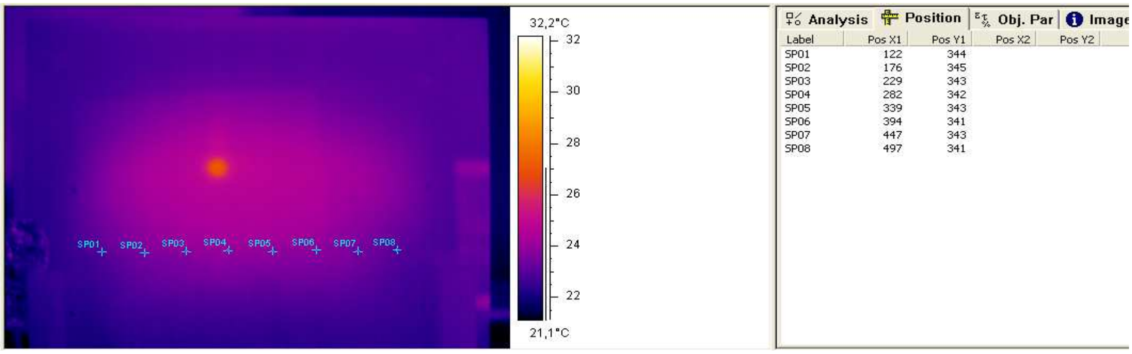

Figure 80: Position of the spots on glass 3 (CGH).

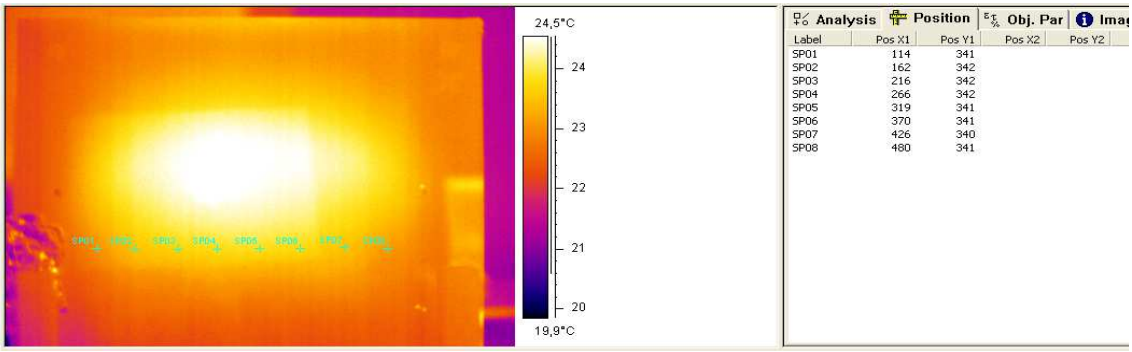

Figure 81: Position of the spots on glass 5 (CGH).

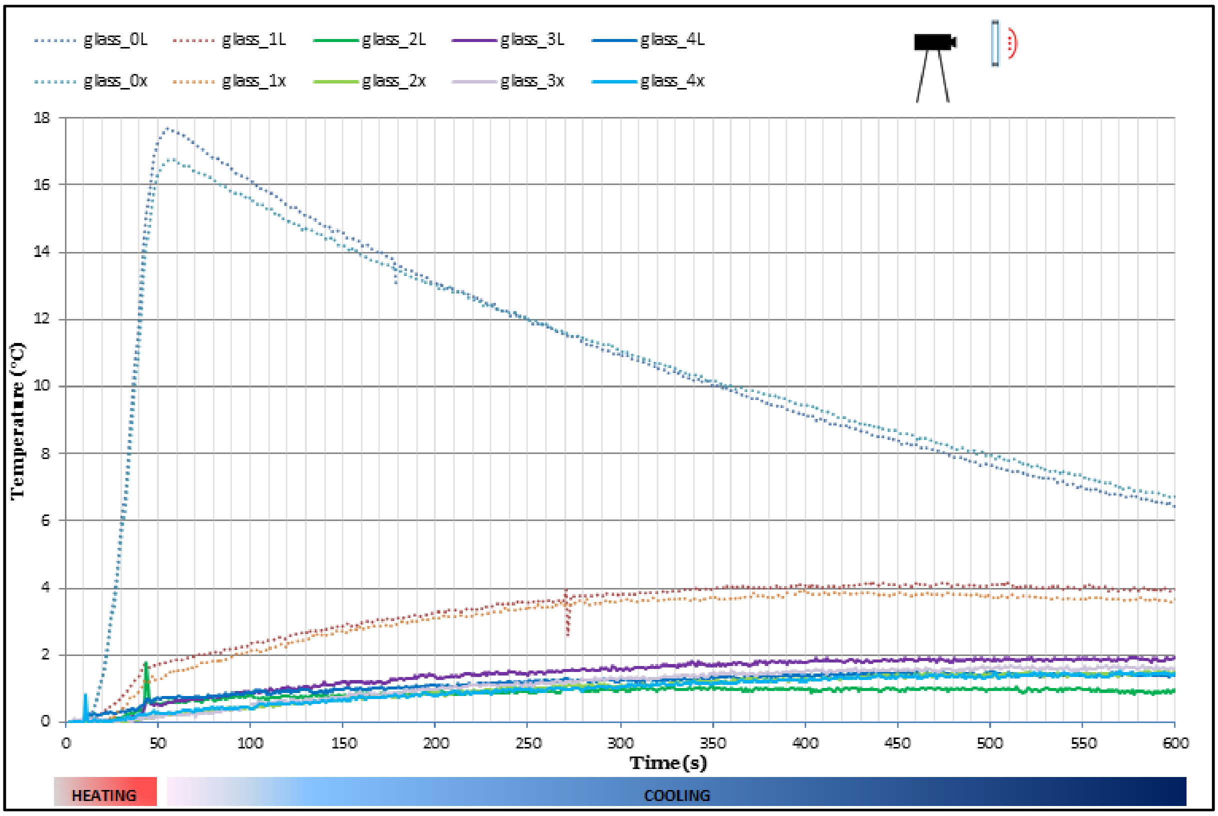

Figure 82: Temperature trend for method I in the configuration CGH.

The temperature trend in figure 82 clearly shows the different behaviour between the conventional glass (0) and double panes glasses (1, 2, 3, and 4): the temperature in glass 0 increases strongly during the heating phase and, after removing the heater, decreases until the end of the heating phase (blue and light blue dots in figure 82). In glasses 1, 2, 3, and 4, when removing the heater, the temperature still grows, which is due to the fact that they store heat because of the gas (air or argon) gap. Moreover, the test clearly shows the difference between glass with and without a treated layer: glass 1 (orange and red dots in figure 82) reaches higher temperatures during the cooling phase than the other types. This phenomenon may be caused by the fact that the treated layer does not allow the heat to go through the glass and thus a lower value of temperature is reached on the glass surface. Moreover, in case of glass 4, where the gap between the two panes is filled with Argon, the heat cannot pass because of its insulating properties.

The same results were given by *method II*, testing the glass in the CGH configuration. In this case, the area having the edge on the aluminim sticks was considered. The height and large average of the rectangular area are 165 and 449 cm respectively.

For sake of synthesis, only side X is reported (figures 83-87). The thermal pattern is shown in figure 88: the approach takes into account the average temperature within the rectangle and the trend is given by the difference of the average temperature between the current and initial value, starting from t = 0.

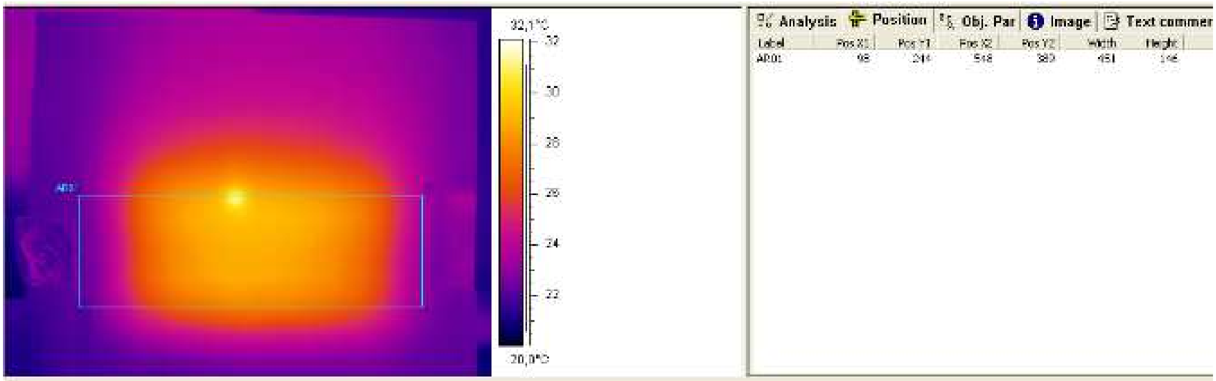

Figure 83: Position of the area on glass 0 (CGH).

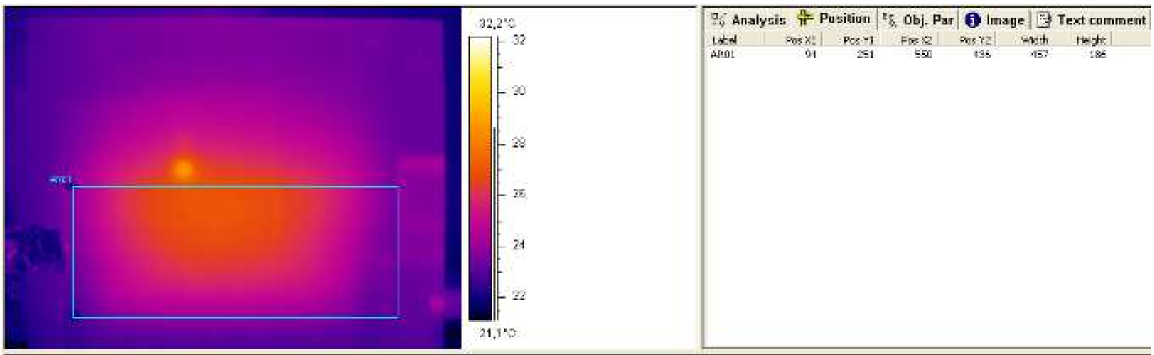

Figure 84: Position of the area on glass 1 (CGH).

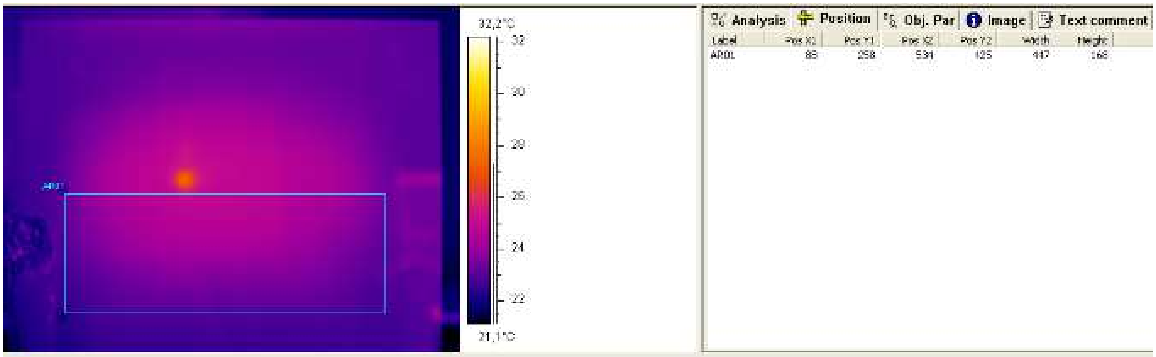

Figure 85: Position of the area on glass 2 (CGH).

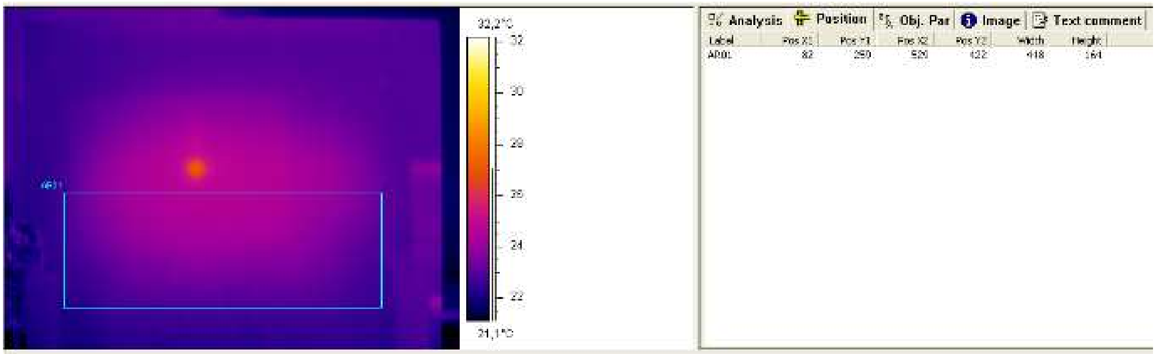

Figure 86: Position of the area on glass 3 (CGH).

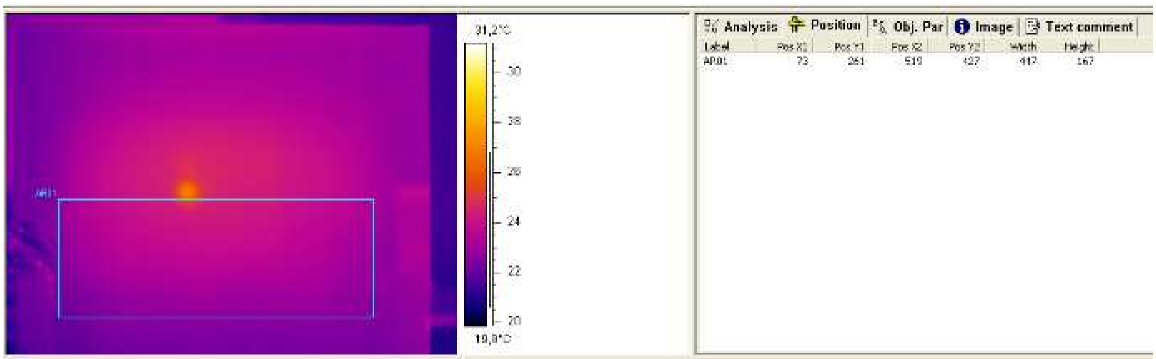

Figure 87: Position of the area on glass 4 (CGH).

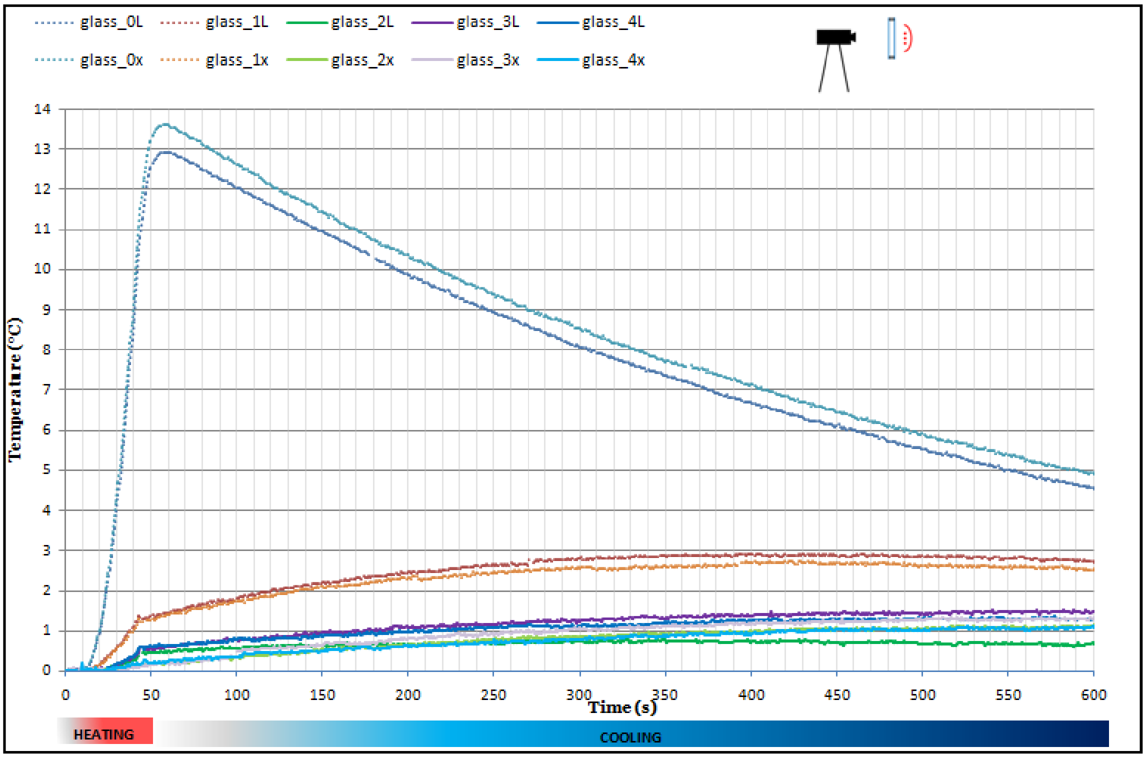

Figure 88: Temperature pattern within the rectangular area (method II, CGH).

If we consider the temperature average trend of the area on the glasses surface and zoom in the range 22-28°C, the graph of figure 89 is given. The untreated layer of the glasses 2, 3, and 4 reaches higher temperatures on the side facing the camera and when the heater is in the configuration CGH, i.e. behind the glass. This is due to the fact that the heat passes through the glass, without finding any barrier. As a consequence, L side is the one without any thermal treatment. On the opposite, side X represents the low emissivity (E) layer, since limited temperatures are reached.

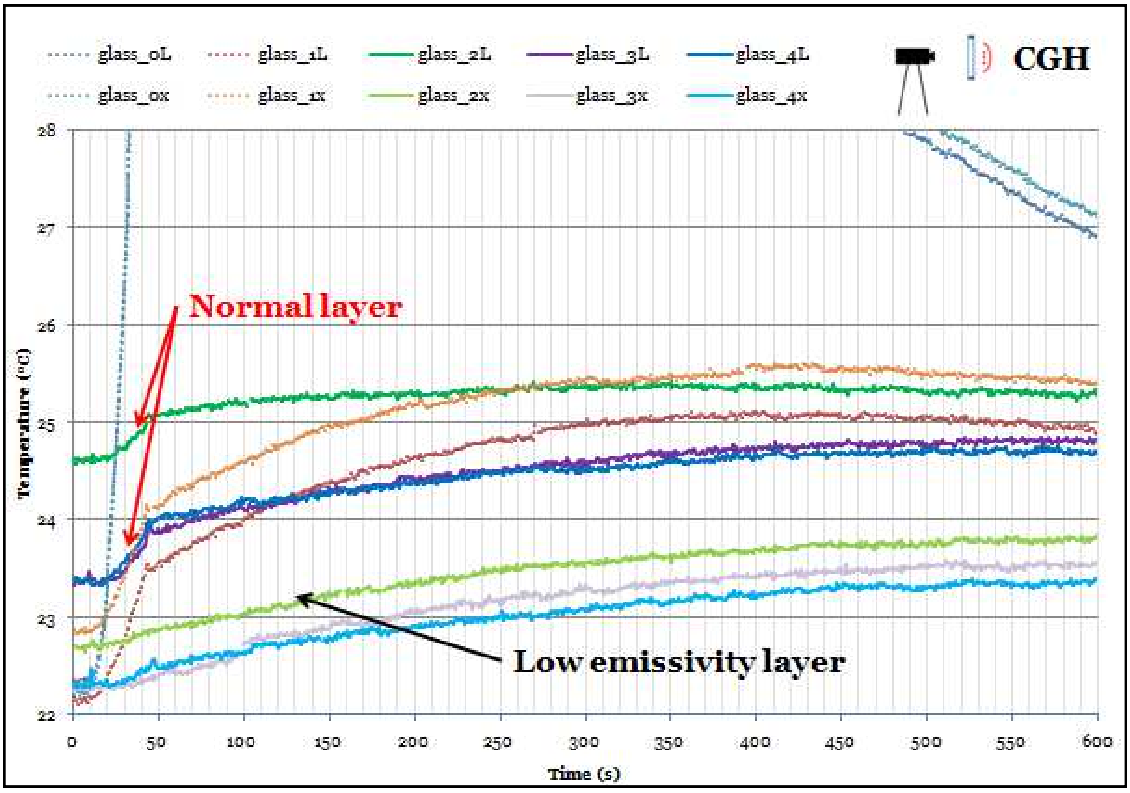

Figure 89: Normal and low emissivity layers.

Table 21 shows the details of the test held on the 25th of April for the configuration CHG and the methods I and II were used to analyse the IR sequences in ThermaCAM. Nevertheless, in both cases the experimental results did not underline the typical behaviour of a specific glass and made it impossible to recognise them, as in the CGH tests (figure 90 and 91).

Sequence code	Heating phase		Recording duration (s)
	Start (s)	End (s)	
2504_glass0x	12	42	612
2504_glass1x	11	42	611
2504_glass2x	11	42	611
2504_glass3x	11	42	611
2504_glass4x	12	43	612
2504_glass0L	12	42	612
2504_glass1L	12	42	612
2504_glass2L	13	43	614
2504_glass3L	12	43	612
2504_glass4L	11	42	611

Table 21: Tests for glasses 0, 1, 2, 3, and 4 in the CHG configuration (side X and L).

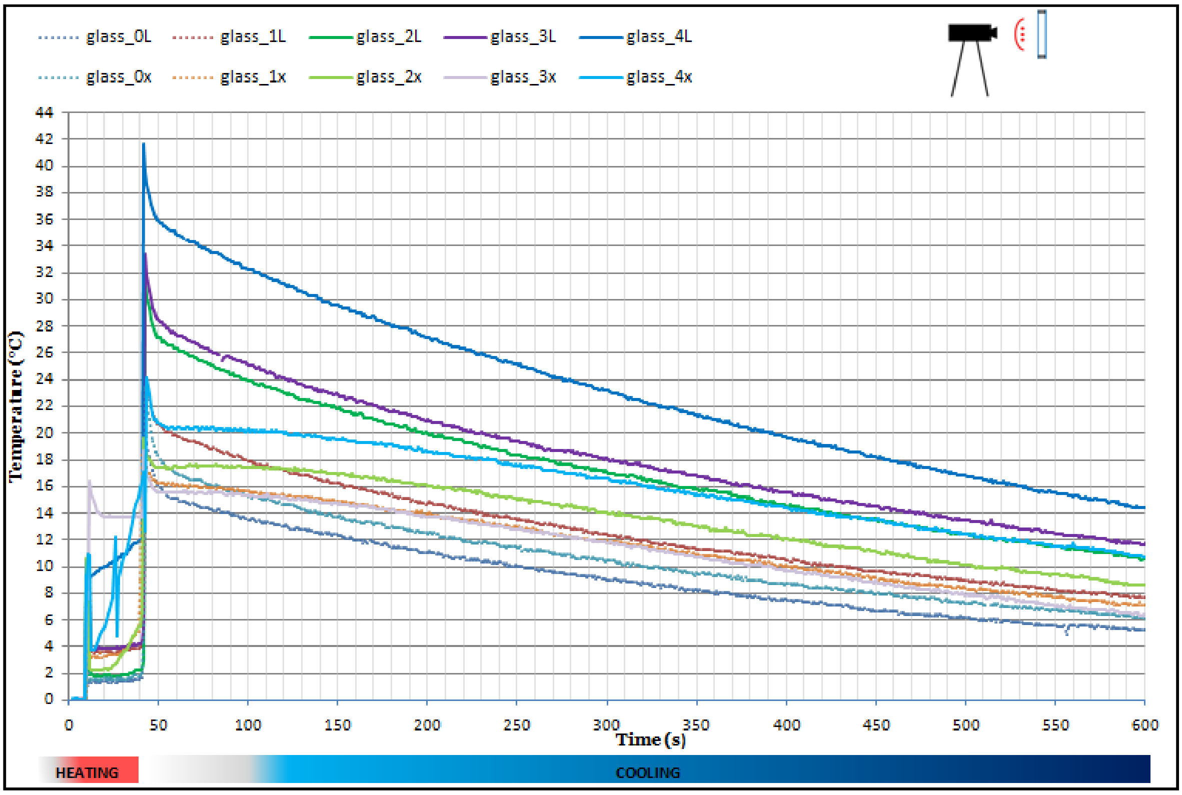

Figure 90: Temperature pattern in method I, CHG.

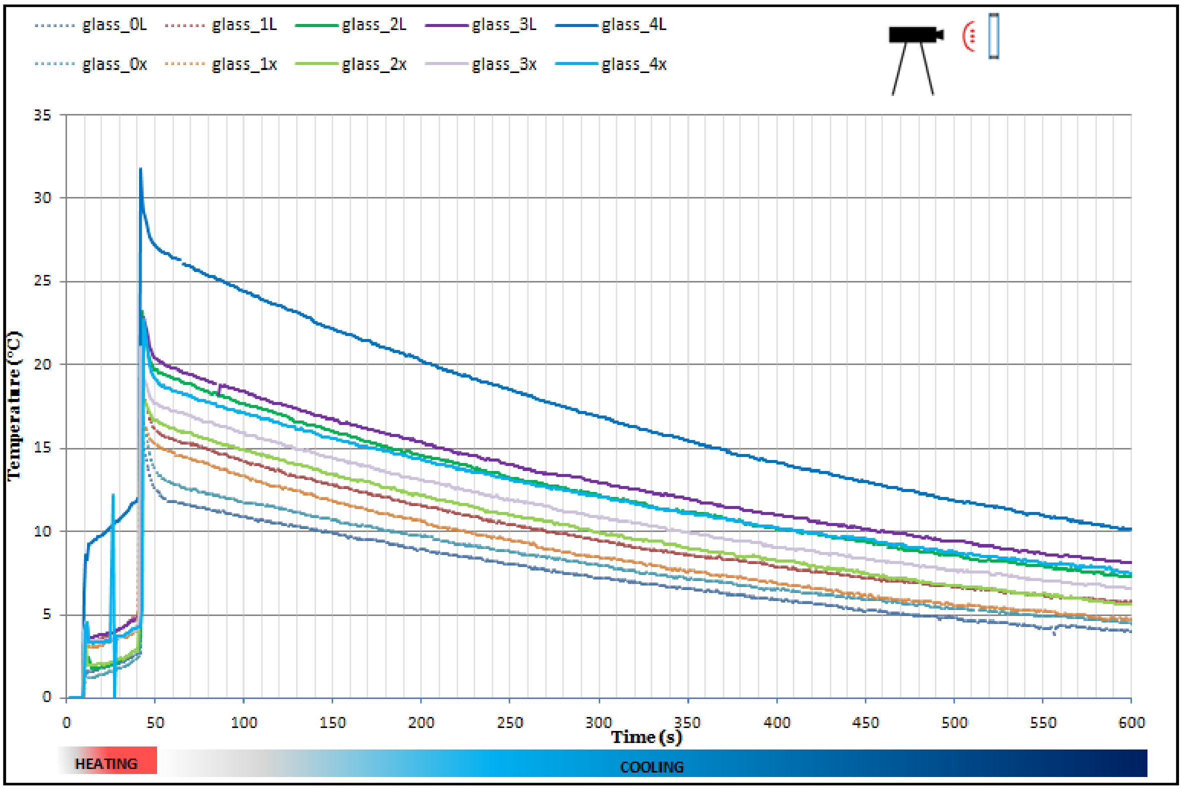

Figure 91: Temperature pattern within the rectangular area (method II, CHG).

A second attempt (table 22) with the configuration CHG was carried out on the 8th of May, but the same results as the previous test occurred (figures 92 and 93).

Sequence code	Heating phase		Recording duration(s)
	Start (s)	End (s)	
0805_glass0x	12	42	612
0805_glass1x	13	43	613
0805_glass2x	12	42	613
0805_glass3x	13	44	613
0805_glass4x	12	42	613
0805_glass0L	12	42	613
0805_glass1L	12	42	613
0805_glass2L	12	42	613
0805_glass3L	13	43	613
0805_glass4L	12	42	613

Table 22: Tests for glasses 0, 1, 2, 3, and 4 in the CHG configuration (side X and L).

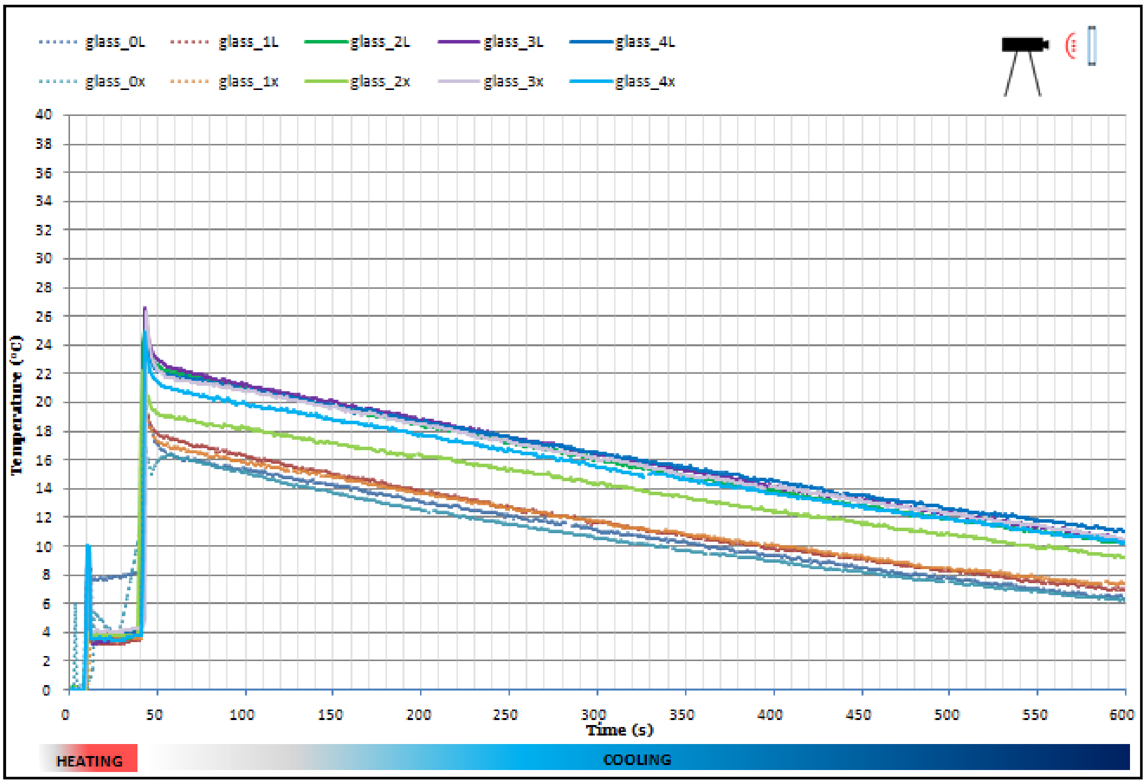

Figure 92: Temperature trend for method I in the configuration CHG.

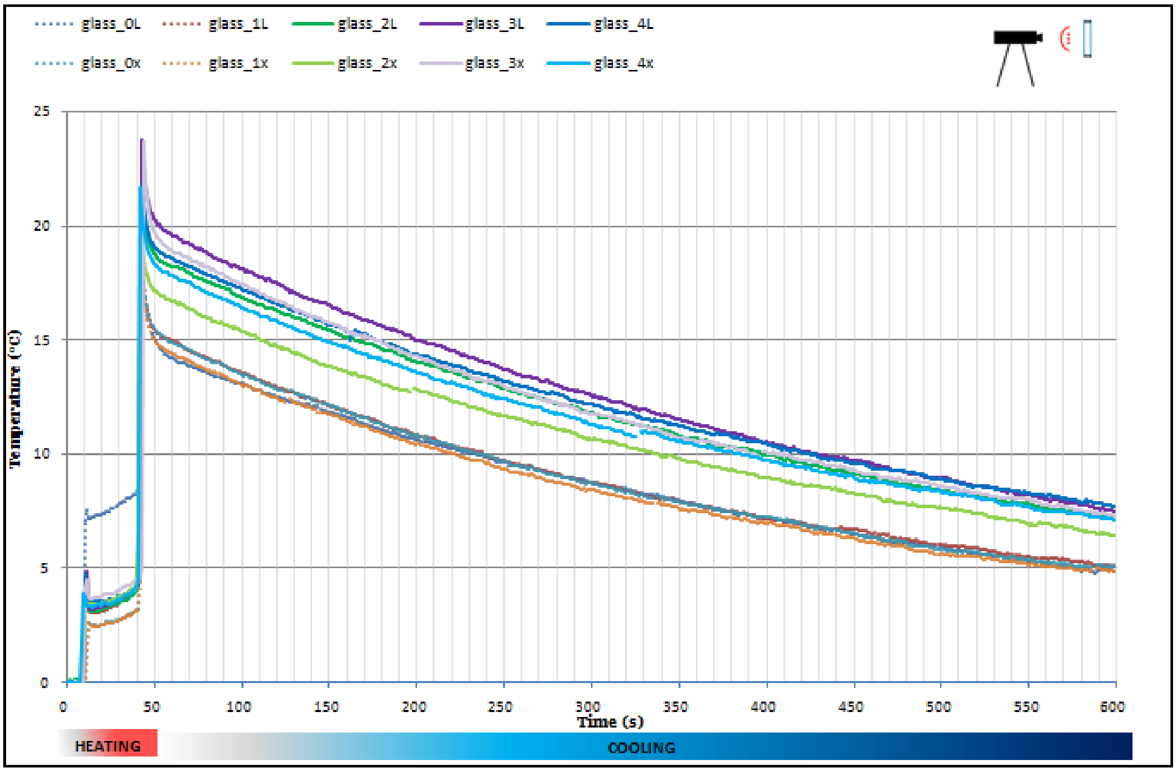

Figure 93: Temperature pattern within the rectangular area (method II, CHG).

However, during this test an IR sequence was recorded for the heater device too in order to study its thermal behaviour and to determine the temperature trend during the heating phase. This is to have temperature information on the heat source for the modelling in FDS. The temperature range of the camera was set to 0-500 and 300-1500 °C to check the maximum values (table 23). Since the heater device has three light bulbs, its thermal characterization is reached by locating three rectangular areas -AR01, AR02, and AR03- on their positions and by recording their average temperature evolution in ThermaCAM (figure 94). Since AR01 and AR03 are at the height of the upper and bottom light bulb and have the same distance from the external edge of the heater (17, 95 cm according to figure 75), the temperature trend is given for AR01 only. AR02 is located in front of the central light bulb. As it is shown in figure 95, the average temperature evolution in time for AR01 and AR02 is extremely similar.

Sequence code	Recording duration (s)
heater_0_500	46
heater_300_1500	

Table 23: Test for the heater device.

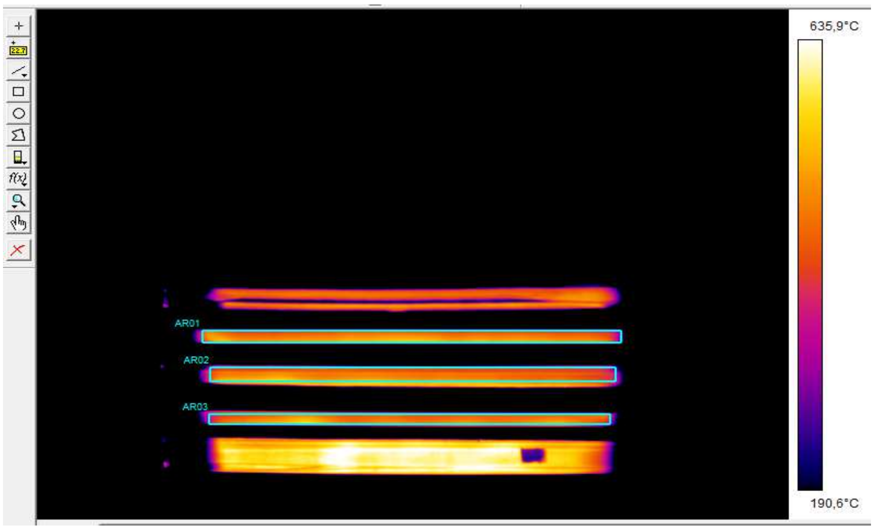

Figure 94: IR image of the heater device.

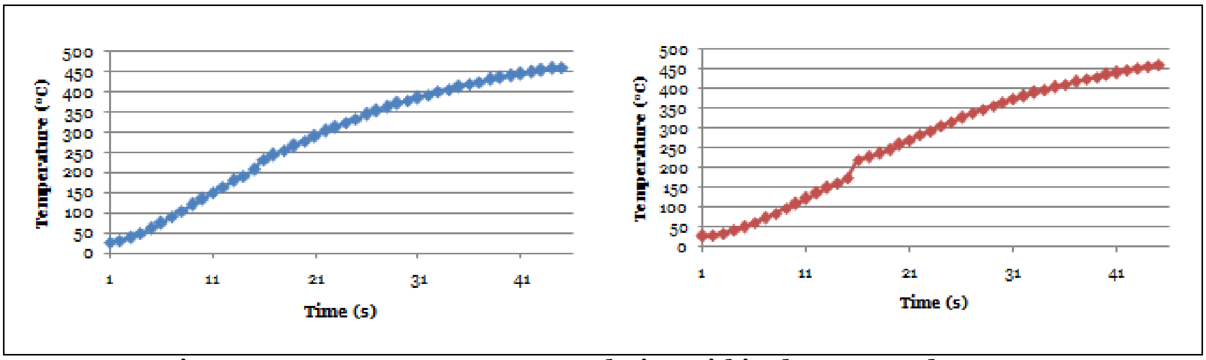

Figure 95: Average temperature evolution within the rectangular areas, AR01 (left) and AR02 (right).

Consequently, the comparison of the results in the CHG configuration did not lead to distinguish the different types of glass by simply considering eight spots in method I or a rectangular area in method II. Another approach was needed in order to find interesting and remarking results to be compared with FDS output. This goal was successfully reached after a detailed image analysis on the recorded IR sequences and taking into account the instant corresponding to the end of the heating phase. This choice is due to the fact that at that moment the maximum temperature is reached in all the glasses.

Two different horizontal lines on the glass surface were identified, namely LI01 and LI02, in front of the upper and central light bulb respectively (figure 96). Figure 97 shows the temperature profile along them at the end of the heating phase: since the upper light bulb is closer to the glass, i.e. to LI02, a higher temperature trend is recorded (red line in figure 97). Thus, the line LI01 does not correspond to the maximum values of surface temperature.

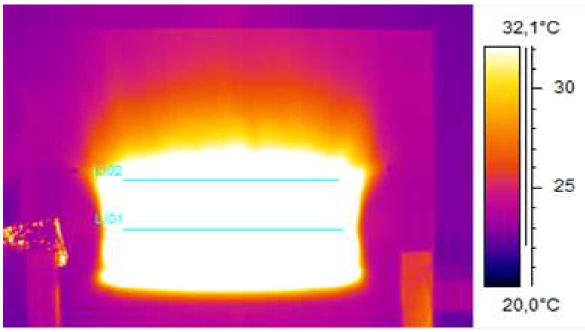

Figure 96: IR image at the end of the heating phase.

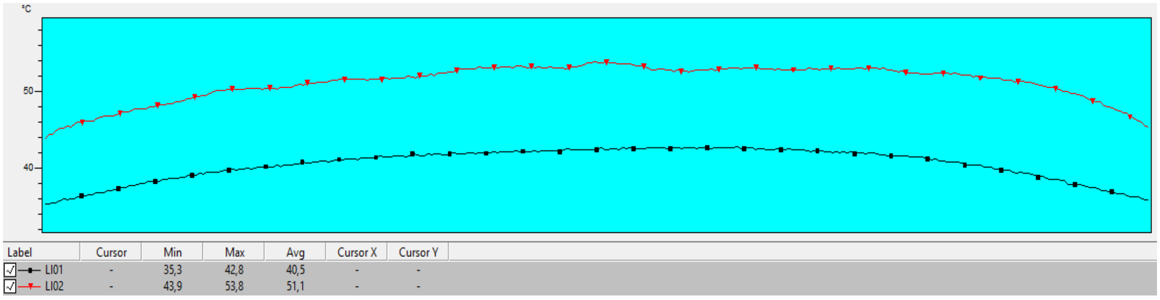

Figure 97: Temperature profile for LI01 and LI02 at the end of the heating phase.

Three different vertical lines on the glass surface were then identified, namely LI03 (blue line in the middle of the glass), LI04 (green line on the left), and LI05 (red line on the right), as shown in figures 98 and 99. Although the temperature profiles do not strongly differ, LI03 reaches the highest peaks.

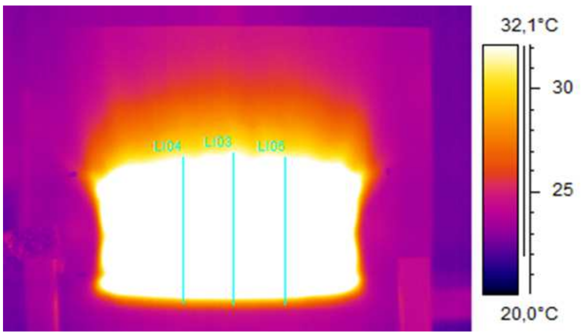

Figure 98: IR image at the end of the heating phase.

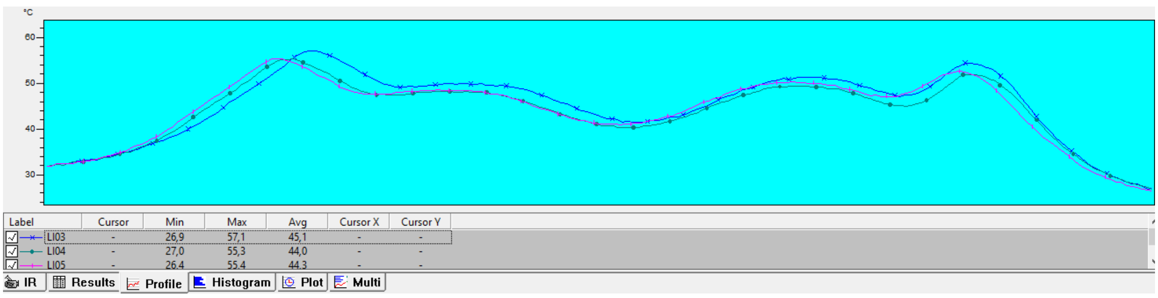

Figure 99: Temperature profile for LI03, LI04, and LI05 at the end of the heating phase.

Focusing the attention on LI03, it can be seen in figure 100 that the thermal profile at the end of the heating phase shows two different picks (1 and 3) and a hollow (2). This behaviour is due to the position of the three light bulbs (figure 103). During the cooling phase (figure 101), the hollow (2) becomes less evident: this behaviour is due to the fact that the heating comes from the bottom and goes up because of convective motion, as reported in figure 103. At the end of the cooling phase (figure 102), the temperature on the top (1) still has the highest value, since it is closer than the central one and receives heat by radiation, conduction and convection too. Temperature differences between (1), (2), and (3) becomes limited in this case.

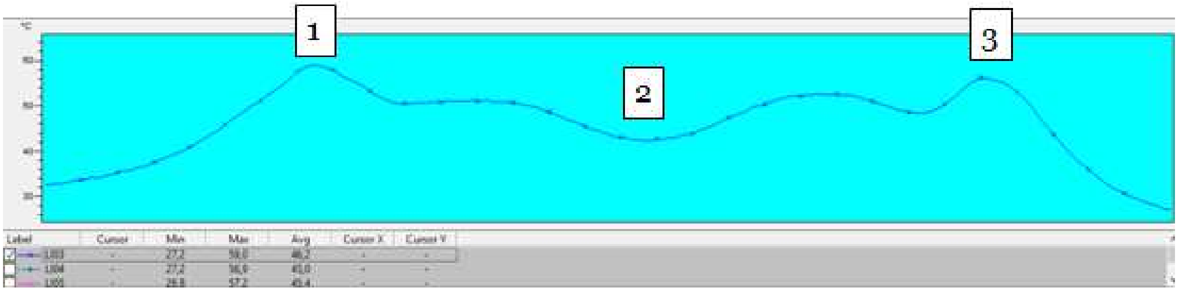

Figure 100: Temperature profile for LI03 at the end of the heating phase.

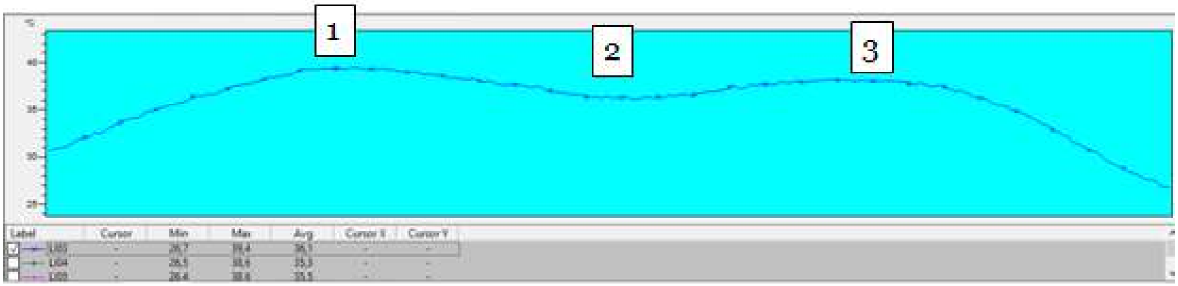

Figure 101: Temperature profile for LI03 during the cooling phase.

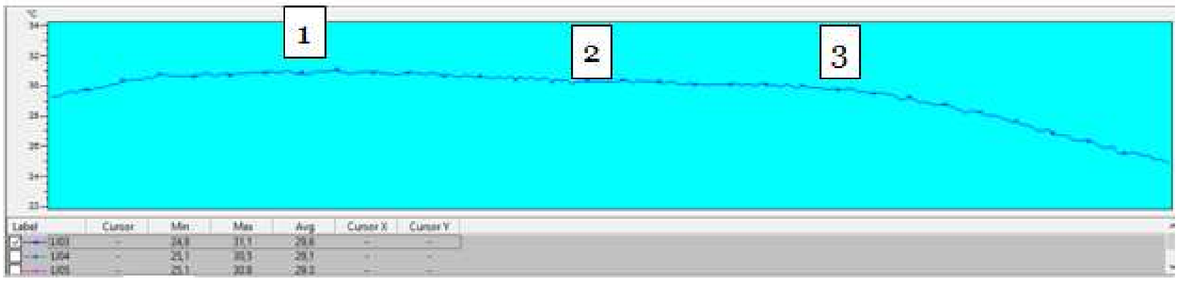

Figure 102: Temperature profile for LI03 at the end of the cooling phase.

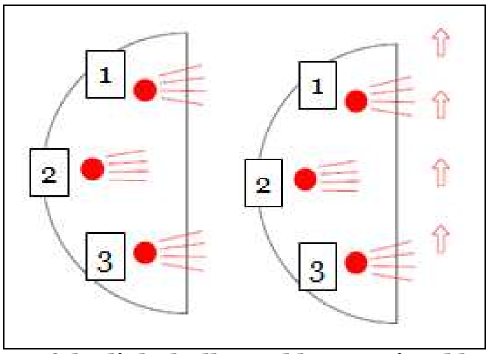

Figure 103: Position of the light bulbs and heat emitted by the heater device.

Therefore, in order to compare the experimental results in ThermaCAM and the output generated by FDS, the following elements were chosen: LI01, which is the vertical line in the middle of the glass; LI02, which the horizontal line on the glass surface in front of the upper light bulb; SP03, which is the spot at the intersection of the two lines (figure 104). The position of these elements is given for glass 0, 1, and 4 in figures 105-107, whereas glass 2 and 3 are not reported since their thermal behaviour in CGH and CHG configuration shows very limited differences if compared to glass 4 (see figures 82, 88, 89).

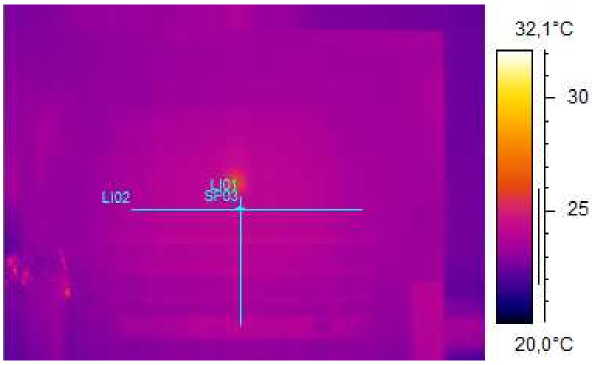

Figure 104: Elements to compare experimental and simulated results.

Figure 105: Position of the elements on glass 0.

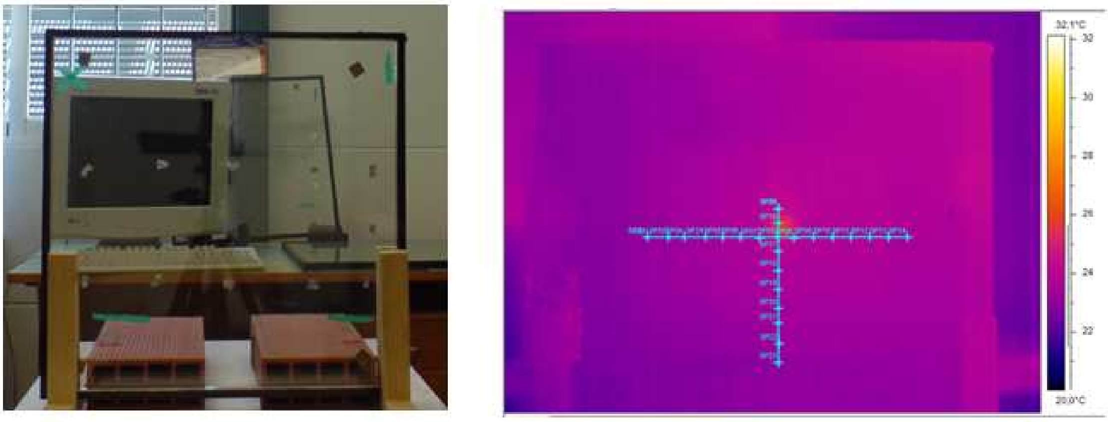

Figure 106: Position of the elements on glass 1.

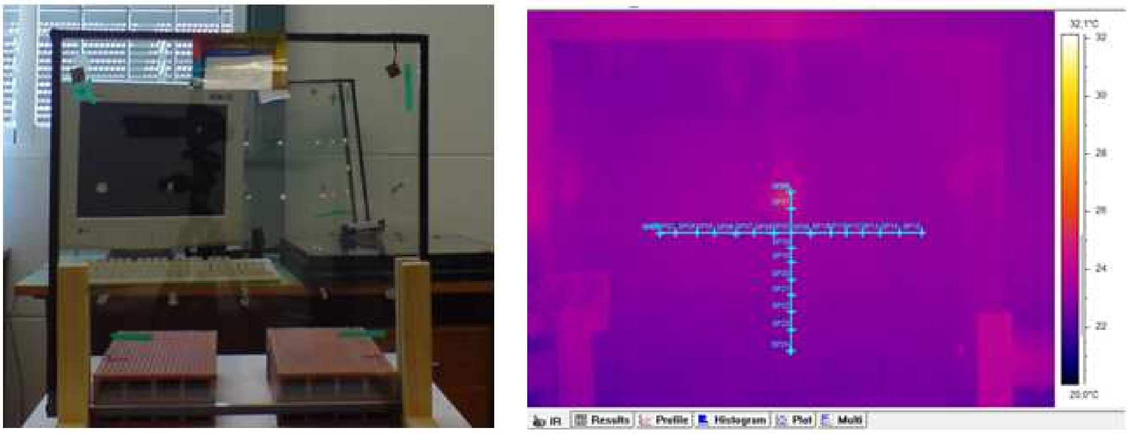

Figure 107: Position of the elements on glass 4.

4.3.6 The simulation in FDS

The glasses thermal behaviour during the IR sequences -both in the heating and cooling phase- was then reproduced in FDS. After entering the lines to read the input file (4.3) and the information for the simulation time and the initial temperature value (4.4) , the size of the mesh was defined (4.5):

&HEAD CHID='glass0_temp_4mesh_vert', TITLE='test1' (4.3)

&TIME T_END = 612 /
&DUMP NFRAMES = 612, MASS_FILE=.TRUE. /
&MISC TMPA=22.0/ (4.4)

&MESH IJK= 24 , 27 , 135 , XB= 0.000 , 0.096 , -0.120 , 0.015 , -0.120 , 0.420 /

&MESH IJK= 24 , 27 , 135 , XB= 0.000 , 0.096 , 0.015 , 0.150 , -0.120 , 0.420 /
&MESH IJK= 24 , 27 , 135 , XB= 0.000 , 0.096 , 0.150 , 0.285 , -0.120 , 0.420 /
&MESH IJK= 24 , 27 , 135 , XB= 0.000 , 0.096 , 0.285 , 0.420 , -0.120 , 0.420 /
(4.5)

The mesh boundaries of the control volume were then identified by the coordinates XMIN, XMAX, YMIN, YMAX, ZMIN, and ZMAX and positioning the table where the glass is located on ZMIN and naming it as "SUPPORT". The remaining mesh boundaries were considered as "OPEN" (4.6):

&VENT MB='XMIN', SURF_ID='OPEN' /
&VENT MB='XMAX', SURF_ID='OPEN' /
&VENT MB='YMIN', SURF_ID='OPEN' /
&VENT MB='YMAX', SURF_ID='OPEN' /
&VENT MB='ZMIN', SURF_ID='SUPPORT' /
&VENT MB='ZMAX', SURF_ID='OPEN'/ (4.6)

The geometry of the heater device was defined by the instruction OBST and by defining the position of the three light bulbs. The heater device appears when t=timer1 (4.7) and is removed from the simulation after 30 seconds, which is the duration of the heating phase, namely when SETPOINT = 30,0 (4.9). The temperature of the light bulbs was defined by RAMP ID, giving a specific value every 3 seconds in order to reproduce the graph in figure 95 and to model their temperature trend during the heating phase (4.8).

&OBST XB= 0.052 , 0.060 , 0.000 , 0.300 , 0.080 , 0.088 , SURF_ID = 'heater', DEVC_ID='timer1' /
&OBST XB= 0.036 , 0.044 , 0.000 , 0.300 , 0.120 , 0.128 , SURF_ID = 'heater', DEVC_ID='timer1' /
&OBST XB= 0.052 , 0.060 , 0.000 , 0.300 , 0.160 , 0.168 , SURF_ID = 'heater', DEVC_ID='timer1' / (4.7)

&SURF ID='heater' , TMP_FRONT= 1000 , RAMP_T='TRad' , COLOR='RED' /
&RAMP ID='TRad',T= 0 ,F=0.161 /
&RAMP ID='TRad',T= 1 ,F=0.161 /
&RAMP ID='TRad',T= 3 ,F=0.205 /

&RAMP ID='TRad',T= 6 ,F=0.252 /

&RAMP ID='TRad',T= 9 ,F=0.288 /

&RAMP ID='TRad',T= 12 ,F=0.321 /

&RAMP ID='TRad',T= 15 ,F=0.350 /

&RAMP ID='TRad',T= 18 ,F=0.374 /

&RAMP ID='TRad',T= 21 ,F=0.396 /

&RAMP ID='TRad',T= 24 ,F=0.415 /

&RAMP ID='TRad',T= 27 ,F=0.431 /

&RAMP ID='TRad',T= 30 ,F=0.445 /

&RAMP ID='TRad',T= 31 ,F=0.022 / (4.8)

&DEVC XYZ=0.0,0.14,0.0, ID='timer1', SETPOINT= 30.0, QUANTITY='TIME', INITIAL_STATE=.TRUE. / (4.9)

The OBST instruction was used to define the geometry of the glasses too, more precisely (4.10) for glass 0, (4.11) for glass 1, and (4.12) for glass 4:

&OBST XB= 0.080 , 0.084 ,-0.100 , 0.400 ,-0.100 , 0.400 , SURF_ID = 'CRISTAL' /

&OBST XB= 0.096 , 0.100 ,-0.100 , 0.400 ,-0.100 , 0.400 , SURF_ID = 'CRISTAL' / (4.10)

&OBST XB= 0.080 , 0.084 ,-0.100 , 0.400 ,-0.100 , 0.400 , SURF_ID = 'CRISTAL' /

&OBST XB= 0.096 , 0.100 ,-0.100 , 0.400 ,-0.100 , 0.400 , SURF_ID = 'CRISTAL' /

&OBST XB= 0.084 , 0.096 , -0.100 , 0.400 , 0.396 , 0.400 , SURF_ID = 'ENCLOSURE' /

&OBST XB= 0.084 , 0.096 , -0.100 , 0.400 , -0.100 , -0.096 , SURF_ID = 'ENCLOSURE' /

&OBST XB= 0.084 , 0.096 , -0.095 , -0.100 , -0.096 , 0.396 , SURF_ID = 'ENCLOSURE' /

&OBST XB= 0.084 , 0.096 , 0.395 , 0.400 , -0.096 , 0.396 , SURF_ID = 'ENCLOSURE' / (4.11)

&OBST XB= 0.080 , 0.084 ,-0.100 , 0.400 ,-0.100 , 0.400 , SURF_ID = 'CRISTAL' /
&OBST XB= 0.080 , 0.084 ,-0.100 , 0.400 ,-0.100 , 0.400 , SURF_ID = 'CRISTAL' /
&OBST XB= 0.096 , 0.100 ,-0.100 , 0.400 ,-0.100 , 0.400 , SURF_ID = 'CRISTAL' /
&INIT XB= 0.084 , 0.096 ,-0.095 , 0.395 ,-0.096 , 0.396 , MASS_FRACTION(1)=1 /, SPEC_ID = 'ARGON' /
&SPEC ID='ARGON' , MASS_FRACTION_0=0.1 , MW=40. /
&OBST XB= 0.084 , 0.096 , -0.100 , 0.400 , 0.396 , 0.400 , SURF_ID = 'ENCLOSURE' /
&OBST XB= 0.084 , 0.096 , -0.100 , 0.400 , -0.100 , -0.096 , SURF_ID = 'ENCLOSURE' /
&OBST XB= 0.084 , 0.096 , -0.095 , -0.100 , -0.096 , 0.396 , SURF_ID = 'ENCLOSURE' /
&OBST XB= 0.084 , 0.096 , 0.395 , 0.400 , -0.096 , 0.396 , SURF_ID = 'ENCLOSURE' / (4.12)

The object surfaces were characterized by SURF ID, having information about colour (RGB), material (MATL_ID), and thickness of the metal back part of the heater device, the glass and the wooden table (4.13). Then, the material itself was given its thermal properties through the command MATL ID: the case of the glass is shown in (4.14).

&SURF ID = 'metal'
RGB = 192,192,192
MATL_ID = 'STEEL'
THICKNESS = 0.001 /
&SURF ID = 'metal2'
RGB = 192,192,192
MATL_ID = 'STEEL'
TRANSPARENCY = 1.0
THICKNESS = 0.005 /
&SURF ID = 'CRISTAL'

RGB = 120,120,170
MATL_ID = 'GLASS'
BACKING = 'EXPOSED'
TRANSPARENCY = 0.5
THICKNESS = 0.005 /
&SURF ID ='SUPPORT'/
RGB = 165,42,42
MATL_ID = 'WOOD' (4.13)

&MATL ID = 'GLASS'
FYI = 'Engineering toolbox'
CONDUCTIVITY = 1.00
SPECIFIC_HEAT = 0.75
DENSITY = 2500
EMISSIVITY = 0.85 / (4.14)

Monitoring planes to check the values of temperature, velocity, and density were added within the control volume (4.15). Furthermore, the temperature on the glass surface is controlled and recorded by positioning sensors through the command DEVC (4.16).

&SLCF PBY= 0.15 ,QUANTITY='TEMPERATURE' /
&SLCF PBY= 0.15 ,QUANTITY='VELOCITY' ,VECTOR=.TRUE. /
&SLCF PBY= 0.15 ,QUANTITY='DENSITY' / (4.15)

&BNDF QUANTITY='WALL_TEMPERATURE' /
&DEVC XYZ= 0.060 , 0.040 , 0.164 , QUANTITY='WALL TEMPERATURE' , ID='TR01' , IOR= 1 / &DEVC XYZ= 0.044 , 0.040 , 0.124 , QUANTITY='WALL TEMPERATURE' , ID='TR02' , IOR= 1 /

&DEVC XYZ= 0.060 , 0.040 , 0.084 , QUANTITY='WALL TEMPERATURE' , ID='TR03' , IOR= 1 /
&DEVC XYZ= 0.060 , 0.140 , 0.164 , QUANTITY='WALL TEMPERATURE' , ID='TR11' , IOR= 1 /
&DEVC XYZ= 0.044 , 0.140 , 0.124 , QUANTITY='WALL TEMPERATURE' , ID='TR12' , IOR= 1 /

&DEVC XYZ= 0.060 , 0.140 , 0.084 , QUANTITY='WALL TEMPERATURE' , ID='TR13' , IOR= 1 /
&DEVC XYZ= 0.060 , 0.240 , 0.164 , QUANTITY='WALL TEMPERATURE' , ID='TR21' , IOR= 1 /
&DEVC XYZ= 0.044 , 0.240 , 0.124 , QUANTITY='WALL TEMPERATURE' , ID='TR22' , IOR= 1 /
&DEVC XYZ= 0.060 , 0.240 , 0.084 , QUANTITY='WALL TEMPERATURE' , ID='TR23' , IOR= 1 / (4.16)

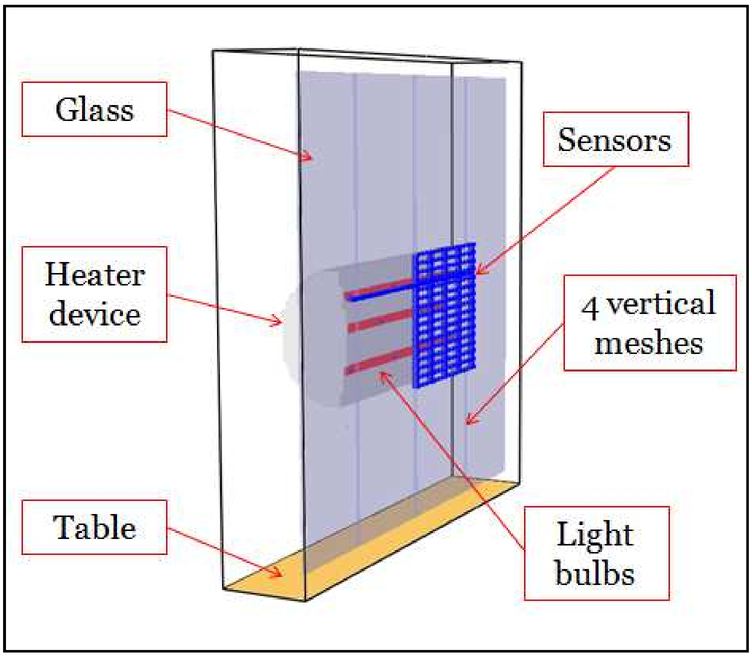

Figure 108: Simulation in FDS.

Since FDS can be run from the command prompt on a single or multiple computers, the parallel calculation was chosen to speed up the solving time. The control volume was divided into smaller elements by the meshing operation and considering 1, 2, 4, 8, and 16 meshes, as in figure 109. The mesh optimization analysis showed that adopting 1, 2 or 4 meshes led to the same temperature profile (figure 110), but the solving time strongly decreases passing from 1 to 4 vertical meshes (table 24).

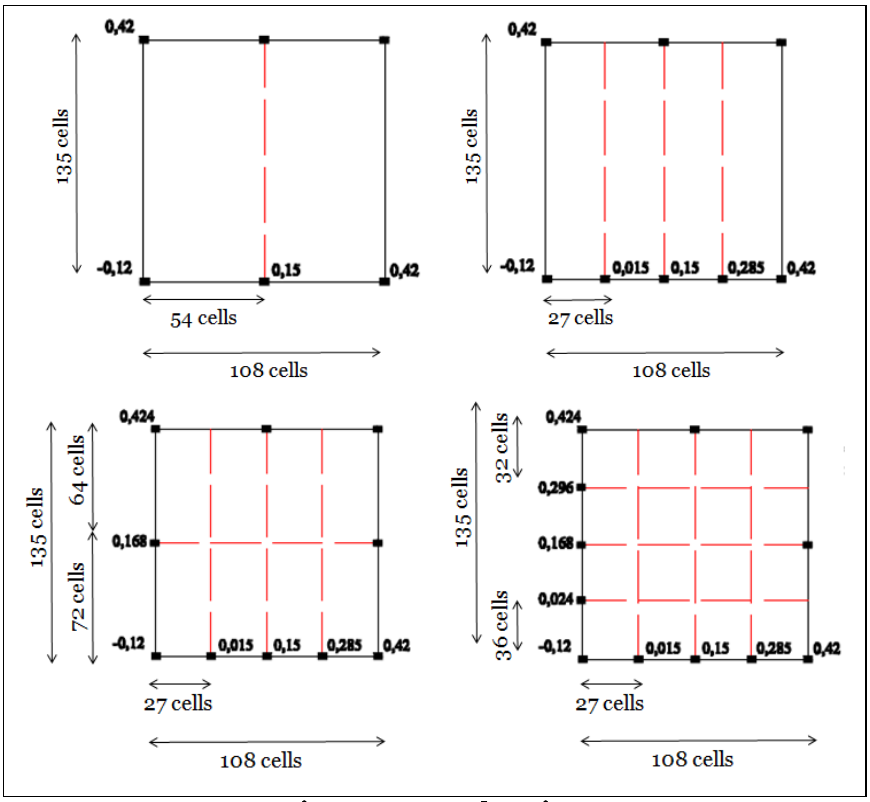

Figure 109: Meshes size.

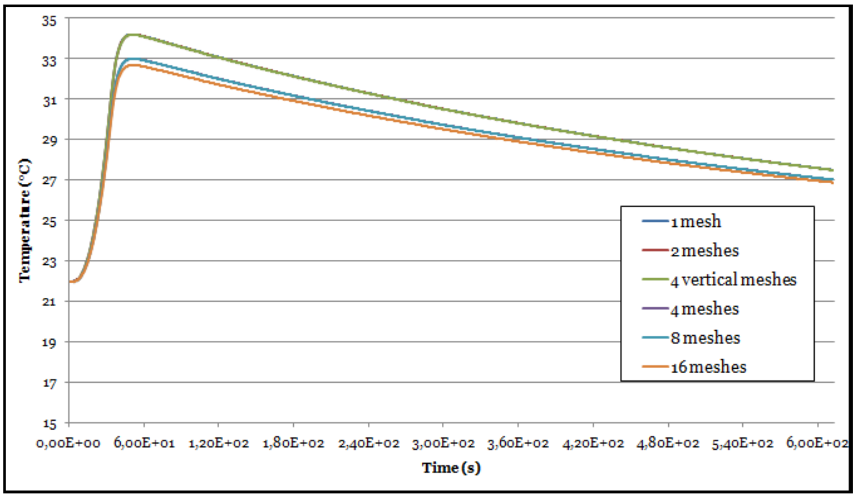

Figure 110: Meshing optimization.

Mesh	Solving time
1 mesh	$14^h\ 45^m$
2 meshes	$13^h\ 47^m$
4 meshes	$6^h\ 30^m$
4 vertical meshes	$4^h\ 30^m$
8 meshes	$1^h\ 42^m$
16 meshes	$1^h\ 1^m$

Table 24: Solving time for different meshes size.

4.4 Results and discussion

The following graphs compare the experimental results in ThermaCAM and the output generated by FDS along the spatial coordinate both for the horizontal and vertical lines (LI01 and LI02) at three different instants:

- at the end of the heating phase corresponding to t = 30 s in FDS, since the heater is positioned at the beginning of the simulation, and to t = 43 s in ThermaCAM, i.e. after its removal;
- in the middle of the cooling phase, namely when t = 286 s in FDS and t = 300 s in ThermaCAM;
- at the end of the cooling phase, which means t = 598 s in FDS and 612 s in ThermaCAM.

The spatial coordinate is given by 60 sensors along the horizontal line in FDS and by 14 spots in ThermaCAM. The number of spots was increased if compared to the previous approaches in order to reach a more accurate description of the thermal behaviour.

Then the results for the spot SP03 at the intersection between the horizontal and vertical lines are shown: the graph represents the thermal trend in time, during the whole heating and cooling phase.

The results are given for glasses 0, 1, and 4. With regard to glass 0, it can be seen that the experimental and simulated curves show a very similar shape in the horizontal line (figure 111), whereas the hollow in the trend appears to be less evident in the vertical line if we compare FDS with ThermaCAM (figure 112). Moreover, the temperature differences on the horizontal line in the middle and at the end of the cooling phase (green and red curve in figure 111) do not reach more than 2-3°C. Comparing the blue curves, the difference becomes 4°C.

As for figure 112, the green and red trends do not differ more than 3°C, although at the beginning of the simulation a lower value is given: this depends on the environmental temperature set in the simulation (TMPA). The peak values of the blue lines need to be improved since they occur at different spatial coordinate, although the value difference is 5°C.

Concerning figure 113, it can be seen that, when removing the heater, the temperature peak reached in FDS is lower than the one recorded in ThermaCAM and the difference is approximately 7°C, which decreases as far as the cooling phase continues, leading to a final difference of 1°C. This probably depends on the thermal properties of the glass, since literature values were used in this case.

With regard to glass 1, the same considerations as glass 0 occur. Although the temperature at the beginning of the simulation is closer to the experimental value, the blue line in figure 114 reaches a higher value in the experimental graph, whose difference with the simulated output is 6°C. However, it has to be noted that the temperature peaks on the vertical line correspond at the same spatial coordinate, leading to a better result than those in glass 0 (figure 115).

Although the shapes of the red, green, and blue lines are quite similar (figures 117 and 118), glass 4 shows the highest temperature differences between simulated and experimental results, reaching 11°C (figure 119). In order to improve these results in FDS and better describe the glasses thermal behaviour, specific equations in Fortran may be introduced while programming. This would lead to take into account the presence of a low-E layer and thermal transmittance.

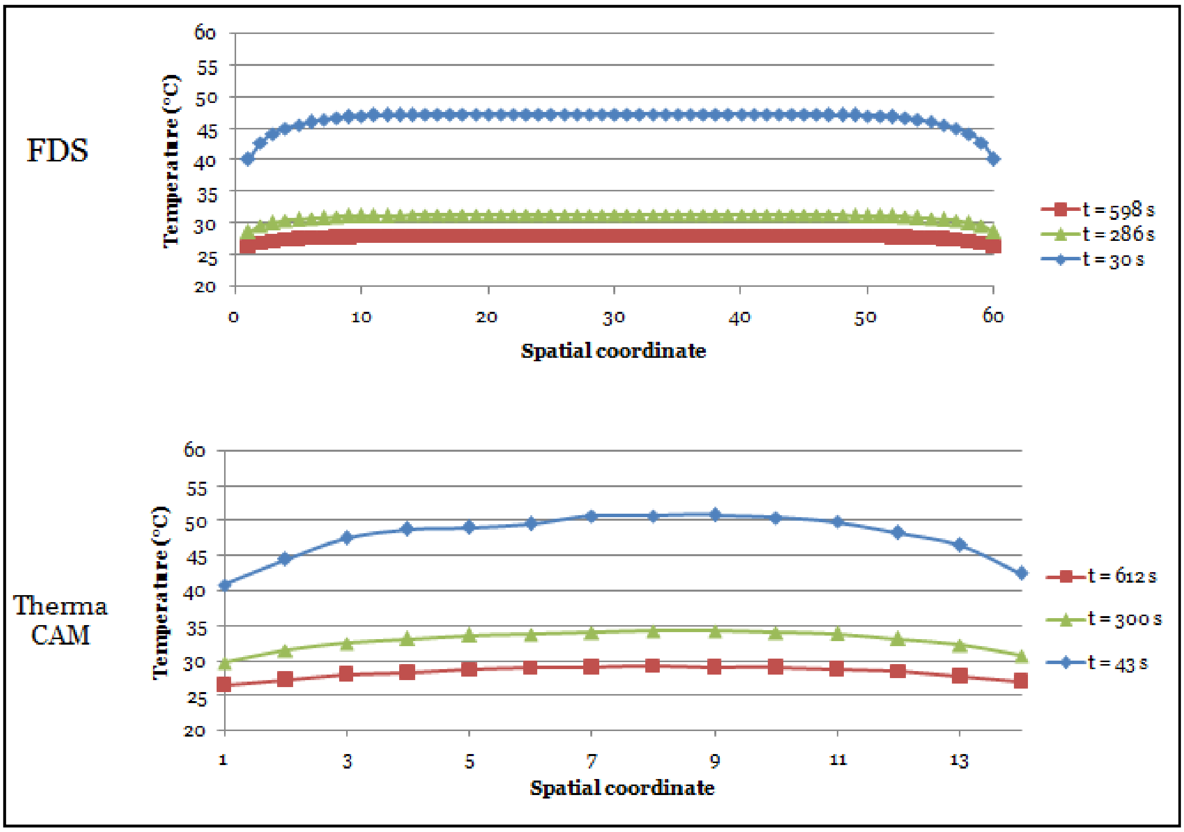

Figure 111: Comparison between experimental and simulated results for glass 0 (on the horizontal line, configuration CHG).

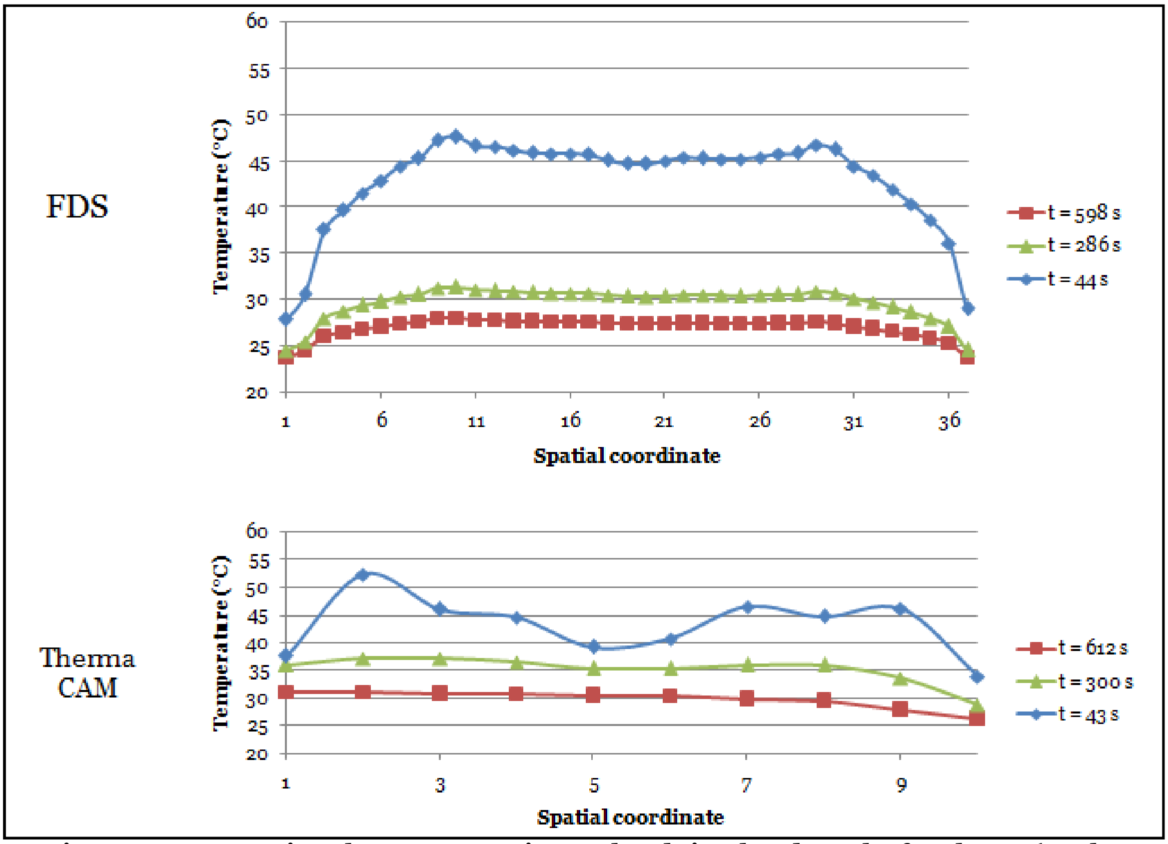

Figure 112: Comparison between experimental and simulated results for glass 0 (on the vertical line, configuration CHG).

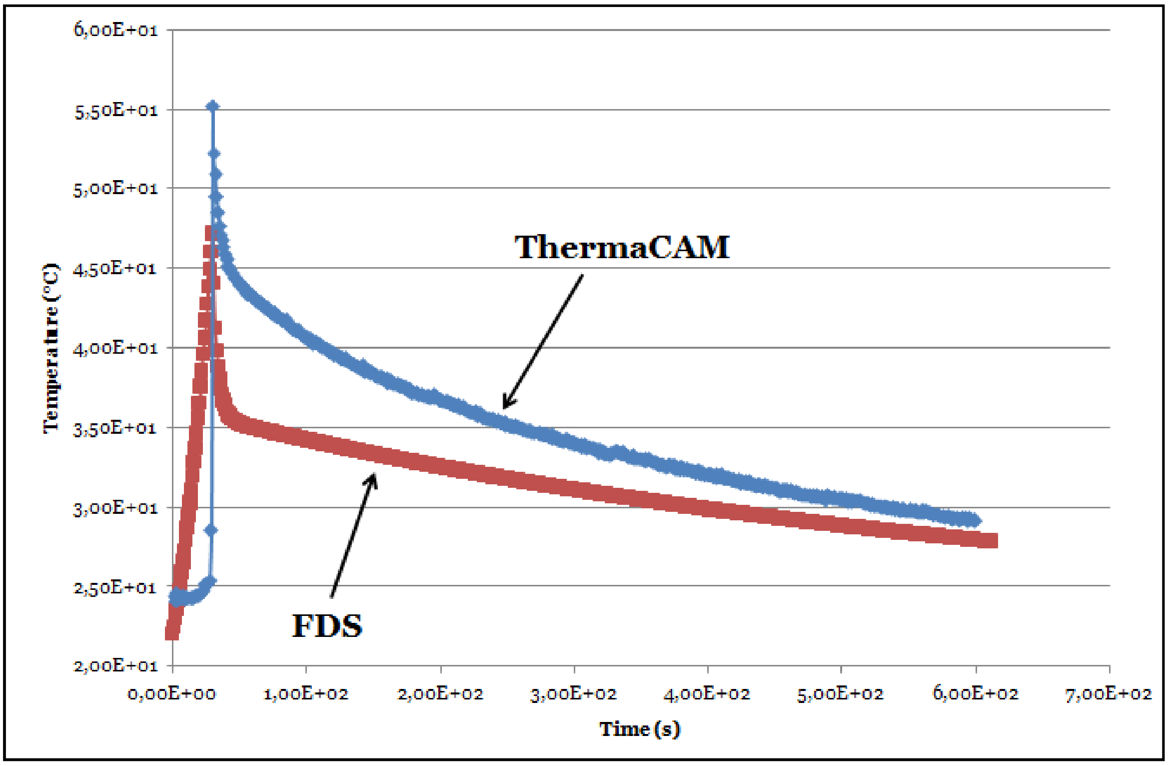

Figure 113: Comparison between experimental and simulated results for glass 0 (on the spot, configuration CHG).

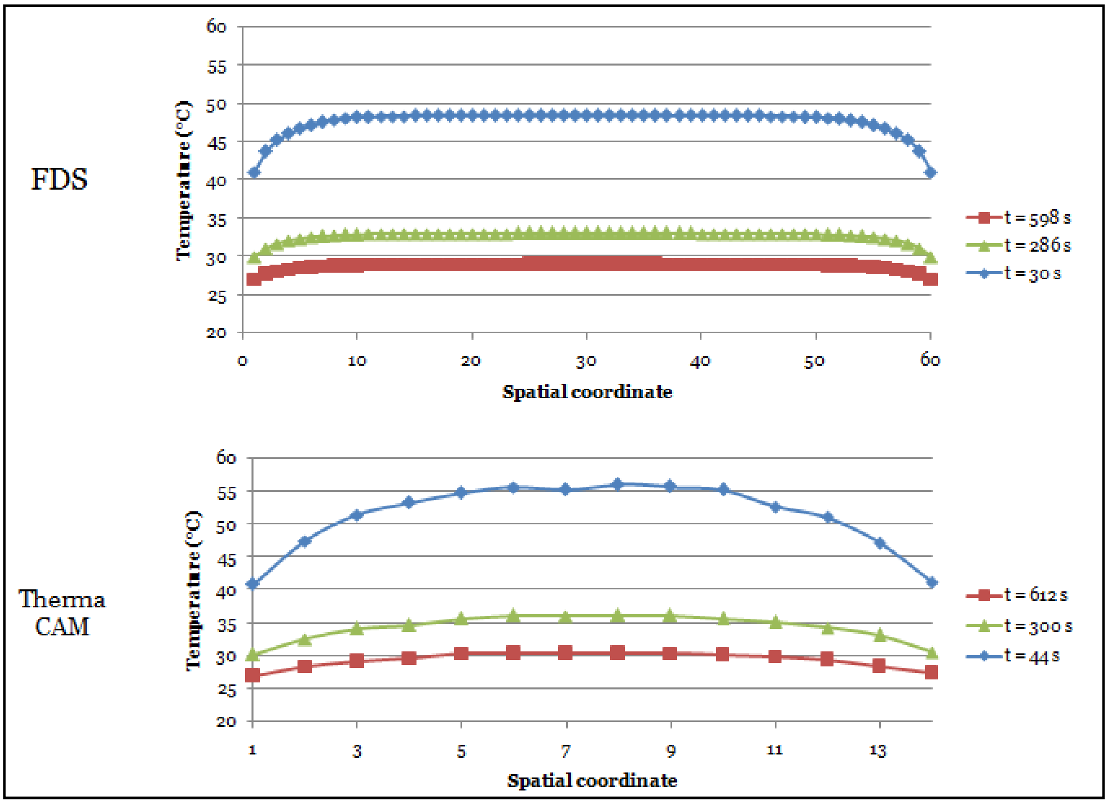

Figure 114: Comparison between experimental and simulated results for glass 1 (on the horizontal line, configuration CHG).

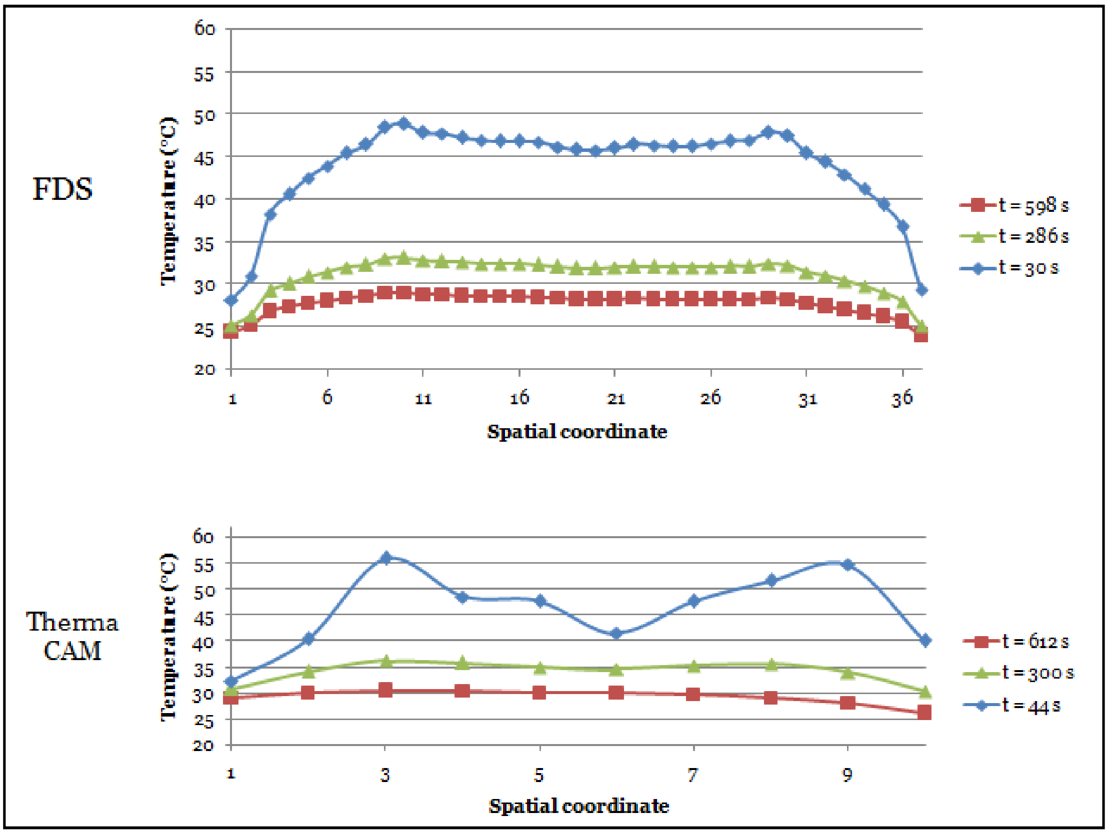

Figure 115: Comparison between experimental and simulated results for glass 1 (on the vertical line, configuration CHG).

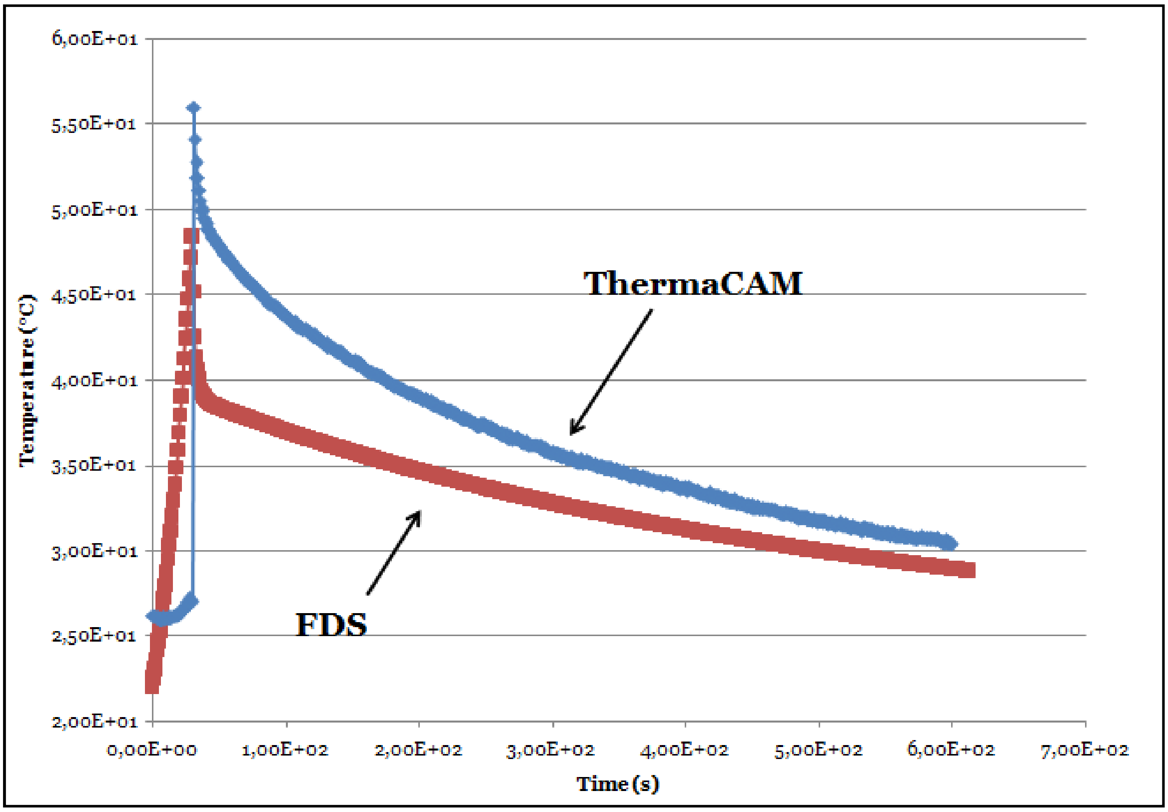

Figure 116: Comparison between experimental and simulated results for glass 1 (on the spot, configuration CHG).

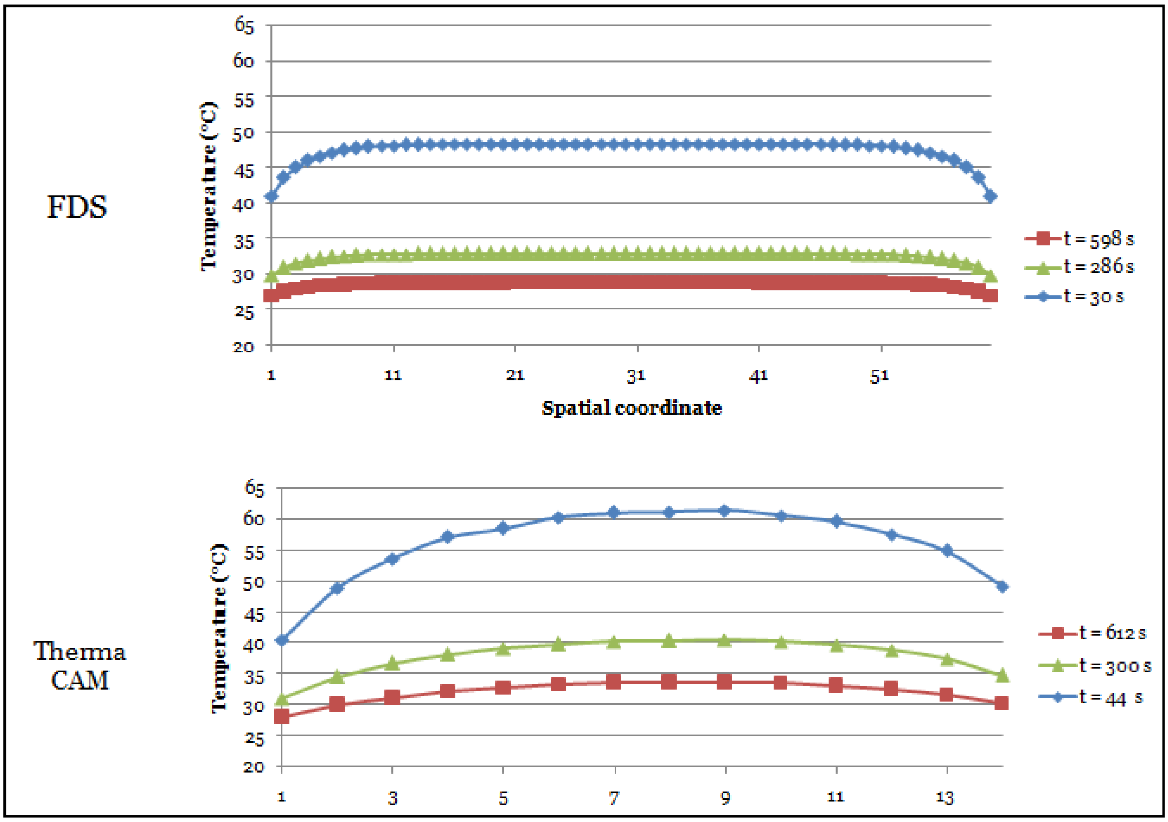

Figure 117: Comparison between experimental and simulated results for glass 4 (on the horizontal line, configuration CHG).

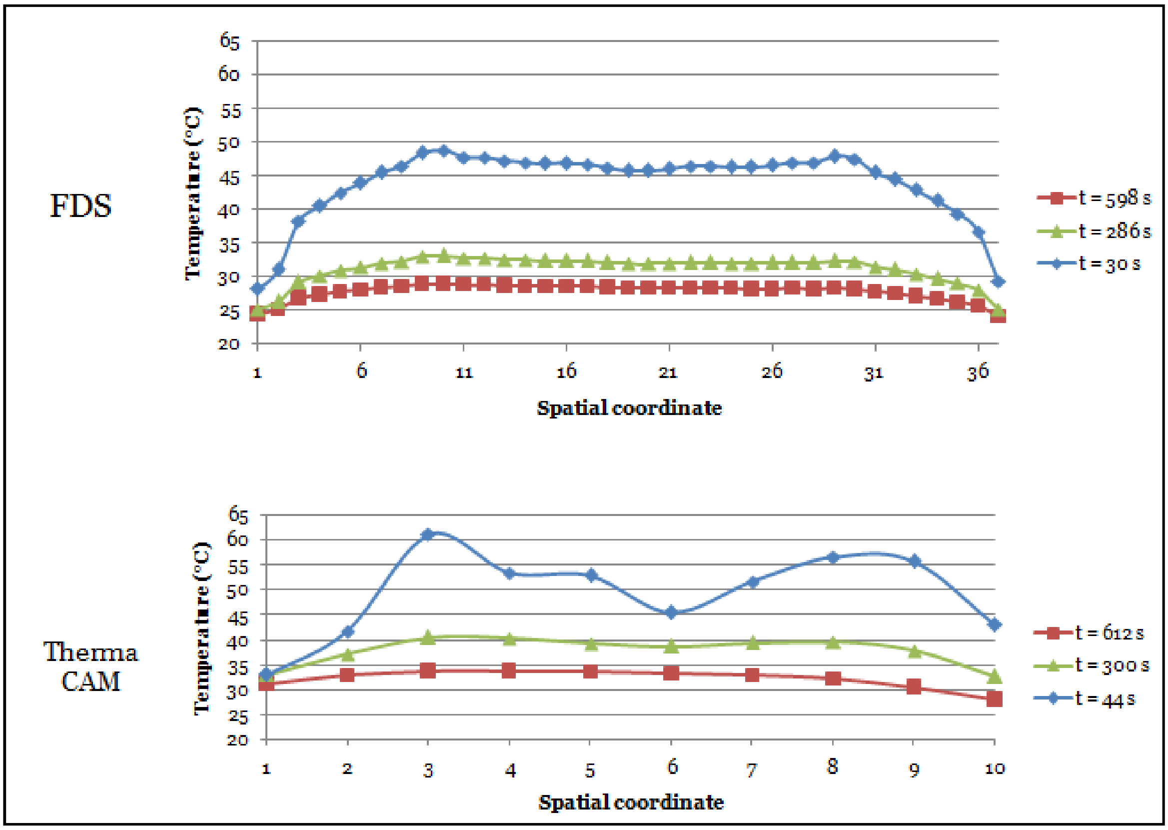

Figure 118: Comparison between experimental and simulated results for glass 4 (on the vertical line, configuration CHG).

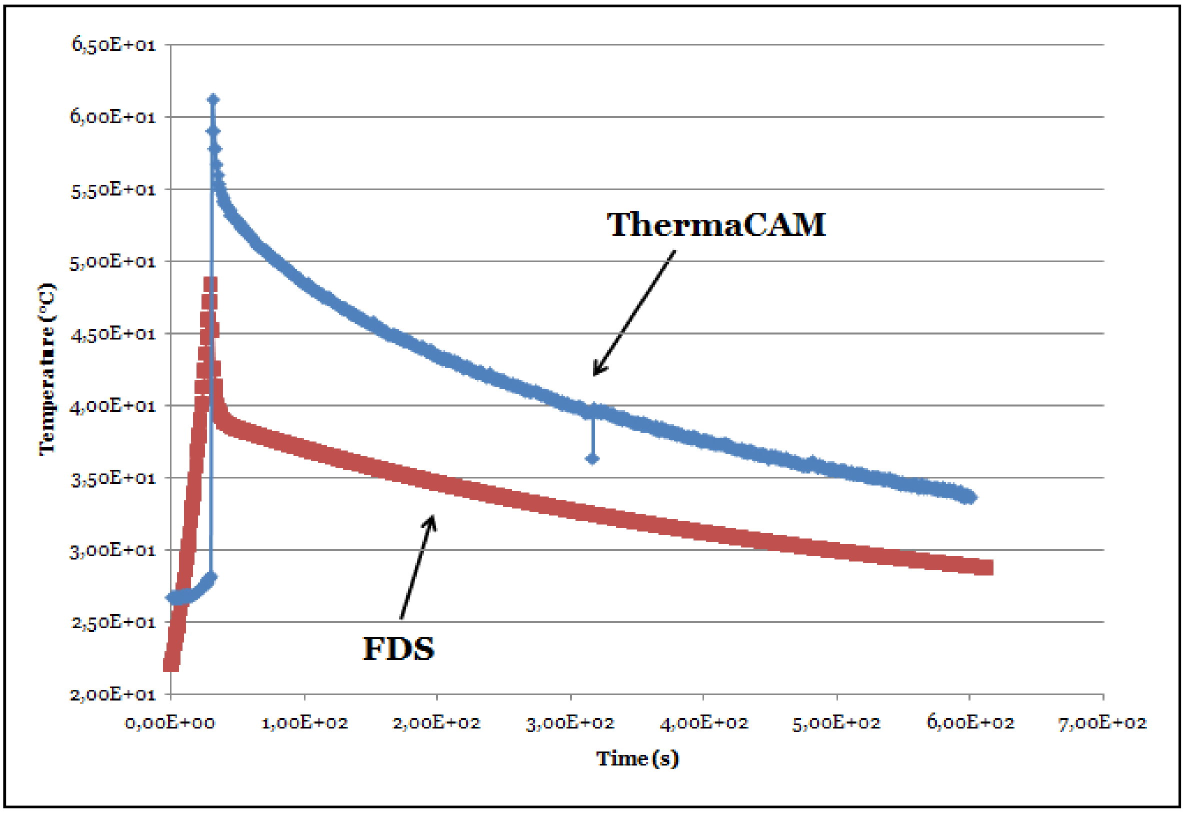

Figure 119: Comparison between experimental and simulated results for glass 4 (on the spot, configuration CHG)

4.5 Conclusion

The present research investigated the use of active IR thermography in order to identify a specific type of glass, without dismounting it and avoiding its breakage or removal. Five common glasses were tested and the experimental results were analysed in ThermaCAM, both during the glass heating and cooling phase. The study of the IR sequences made it possible to distinguish the thermal behaviour of a traditional glass from double-pane glasses, to recognize the thermal behaviour of a layer without any specific surface treatment and the low-E layer thermal pattern.

After reproducing the window thermal behaviour in FDS, the software output was compared with the IR recorded sequences: the difference between the experimental and simulated results vary from 2-4 °C in case of spatial temperature distribution up to 11 °C in case of time distribution. These differences decrease as far as the cooling phase continues, leading to very limited values at the end of the test (1°C). However, the shape of the curves both in experimental and simulated results is very similar: this means that the physical phenomenon is correctly described and the values need to be improved by working on the thermal properties of the glass itself.

CFD modelling seems to be an adequate tool to predict the glass thermal behaviour, as in Gloriant *et al.* (2015), Carlos and Corvacho (2014), and Ismail and Henriquez (2009). However, it has to be noted that it is not easy to accurately predict the response of such a system, especially in case of airflow windows or smart façades which involve complex geometry and radiative and convective heat exchange [Ismail and Henriquez, 2009].

According to Gloriant *et al.* (2015), two main indicators are used to characterize a window, namely the thermal transmittance U and the solar heat gain coefficient SHGC, whose definition is given in ISO-15099 (2003). While U corresponds to the heat loss factor providing heat transfer through the window per square meter for a temperature difference of one degree between inside and outside temperatures, SHGC is the solar heat gain coefficient which indicates the rate of solar radiation impacting the heat balance indoor. In order to improve the simulations in FDS, specific equations introducing U and SHGC may be added in the code while programming.

CONCLUSION

The present Doctoral thesis investigated the thermal behaviour of some energy-efficient technologies and the improvement which may be reached with specific interventions. Since the proposed actions involve the solution of heat differential equations, the analysis was based on the use of the Finite Element and Finite Difference Methods.

After describing the basics of heat transfer, three different case studies were analysed:

- ✓ Use of a Downhole heat exchanger for heating in the Province of Viterbo, after calculating the amount of withdrawable heat in Matlab and the heat transfer in the surrounding of the DHE in Comsol Multiphysics;
- ✓ Possible retrofitting actions on opaque enclosures and thermal bridges for an existing public building in Sabaudia (Latina, Central Italy) which concerned the use of 10-cm insulating thermal material to reduce the global energy performance, thermal transmittance, and heat losses;
- ✓ Use of active IR thermography to identify a specific type of glass which led to distinguish the thermal behaviour of a traditional glass from double-pane glasses, to recognize the thermal behaviour of a layer without any specific surface treatment and the low-E layer thermal pattern.

The research involved the use of software products based on FEM and FDM, speeding up the solving times which resulted to be very limited and avoiding any hand calculations.

The simulation in Comsol Multiphysics represented an extremely valid tool to evaluate the improvement of the energy efficiency of a specific action, both in case study 1 and 2.

Although some instructions in Fortran may be introduced while programming, FDS demonstrated to be an accurate software in predicting and describing the glass thermal behaviour during the heating and cooling phase.

References

Acuna J. Distributed thermal response tests – New insights on U pipe and coaxial heat exchangers groundwater-filled boreholes. Doctoral Diss., KTH School of Industrial Engineering and Management, Stockholm, Sweden, 2013.

Agarwal S. Fundamentals of finite difference methods (FDM). 9th Indo-German Winter Academy. IIT Bombay; December 10-12, 2010.

Al-Sanea S, Zedan MF. Effect of thermal bridges on transmission loads and thermal resistance of building walls under dynamic conditions. Appl Energ 2012; 98: 584-83.

Asdrubali F, Baldinelli G, Bianchi F. A quantitative methodology to evaluate thermal bridges in buildings. Appl Energ 2012; 97: 365-73.

ASHRAE Handbook, 2008.

Avdelidis NP, Moropoulou A. Emissivity considerations in building thermography. Energ Buildings 2003; 35: 663-7.

Balaras CA, Argiriou AA. Infrared thermography for building diagnostics. Energ Buildings 2002; 34: 171-83.

Cannas B, Caracangiu S, Concu G, Trulli N. Modeling of active infrared thermography for defect detection in concrete structures. Excerpt from the Proceedings of the 2012 COMSOL Conference in Milan; 2012.

Carlini M, Castellucci S. Efficient energy supply from ground coupled heat transfer source. ICCSA 2010, Part II, LNCS 6017, pp. 177-9. Springer-Verlag Berlin Heidelberg, Germany.

Carlini M, Monarca D, Biondi P, Castellucci S, Honorati T. A simulation model for the exploitation of geothermal energy for a greenhouse in Viterbo province. International Conference Ragusa SHWA September 16-18, 2010, Ragusa Ibla Campus, Italy.

Carlini M, Castellucci S. Modelling the vertical heat exchanger in thermal basin. ICCSA 2011, Part IV, LNCS 6785, pp. 277-86. Springer-Verlag Berlin Heidelberg, Germany.

Carlini M, Castellucci S, Allegrini E, Tucci A. Down-hole heat exchangers: Modelling of a low-enthalpy geothermal system for district heating. Mathematical Problems in Engineering 2012, art. no. 845192.

Carlini M, Allegrini E, Zilli D, Castellucci S. Simulating heat transfers through the building envelope: A useful tool in the economical assessment. Energy Procedia 2014; 45: 395-404.

Carlos JS, Corvacho H. Evaluation of thermal performance indices of a ventilated double window through experimental and analytical procedures: Uw-values. Renew Energ 2014; 63: 747-54.

Carotenuto A, Casarosa C, Vanoli L. Optimizing the position of the tube casing slotted section for geothermal wells with a down-hole exchanger. Geothermics 2001; 30: 133-57.

Carotenuto A, Massarotti N, Mauro A. A new methodology for numerical simulation of geothermal down-hole heat exchangers. Appl Therm Eng 2012; 48: 225-36.

Catalina T, Virgone J, Roux J-J, Blanco E. Effet de l'inertie thermique, de la surface vitree et du coeffcient de forme sur les besoins en chauffage d'une habitation. In: Congres IBPSA, Lyon, France; 2008

Cerdeira F, Vàzquez ME, Collazo J, Granada E. Applicability of infrared thermography to the study of the behaviour of stone panels as building envelopes. Energ Buildings 2011; 43: 1845-51.

Comitato Termotecnico Italiano (CTI).

Comsol Multiphysics. Heat transfer user's guide; 2013.

Cui P, Li X, Man Y, Fang Z. Heat transfer analysis of pile geothermal heat exchangers with spiral coils. Appl Energ 2011; 88: 4113-9.

Decreto Legge 16 aprile 2013 n. 75. Regolamento recante disciplina dei criteri di accreditamento per assicurare la qualificazione e l'indipendenza degli esperti e degli organismi a cui affidare la certificazione energetica degli edifici, a norma dell'articolo 4, comma 1, lettera c), del decreto legislativo 19 agosto 2005, n. 192.

Decreto Legge 4 giugno 2013, n.63 (convertito con modificazioni in Legge 3 agosto 2013, n.90). Disposizioni urgenti per il recepimento della Direttiva 2010/31/UE del Parlamento europeo e del Consiglio del 19 maggio 2010, sulla prestazione energetica nell'edilizia per la definizione delle procedure d'infrazione avviate dalla Commissione europea, nonché altre disposizioni in materia di coesione sociale.

Decreto Legislativo del 10 agosto 2005 n. 192. Attuazione della Direttiva 2002/91/CE relativa al rendimento energetico nell’edilizia.

Decreto Legislativo del 29 dicembre 2006 n.311. Disposizioni correttive ed integrative al D. Lgs. 192/05.

Decreto Legislativo del 30 maggio 2008 n. 115. Attuazione della Direttiva 2006/32/CE.

Decreto del Ministero dello Sviluppo Economico del 22 novembre 2012 recante modifiche alle Linee Guida Nazionali del 26 giugno 2009.

Decreto del Ministero dello Sviluppo Economico del 28 dicembre 2012. Incentivazione della produzione di energia termica da fonti rinnovabili ed interventi di efficienza energetica di piccole dimensioni.

Decreto del Presidente della Repubblica del 26 agosto 1993 n. 412. Regolamento recante norme per la progettazione, l'installazione, l'esercizio e la manutenzione degli impianti termici degli edifici ai fini del contenimento dei consumi di energia, in attuazione dell'art. 4, comma 4, della Legge 10/91.

Decreto del Presidente della Repubblica del 2 aprile 2009 n. 59. Regolamento attuativo all'articolo 4, comma 1, lettera a) e b), del D. Lgs. 10 agosto 2005 n. 192.

De Rosa M, Bianco V, Scarpa F, Tagliafico LA. Heating and cooling building energy demand evaluation; a simplified model and a modified degree days approach. Appl Energ 2014; 128:217-29.

Directive 2002/91/EC of the European Parliament and of the Council of 16 December 2002 on the energy performance of buildings.

Directive 2009/28/EC of the European Parliament and of the Council of 23 April 2009 on the promotion of the use of energy from renewable sources and amending and subsequently repealing Directives 2001/77/EC and 2003/30/EC.

Directive 2010/31/EC of the European Parliament and of the Council of 19 May 2010 on the energy performance of buildings (recast).

Directive 2012/27/EC of the European Parliament and of the Council of 25 October 2012 on energy efficiency, amending Directives 2009/125/EC and 2010/30/EU and repealing Directives 2004/8/EC and 2006/32/EC.

Evola G, Margani G, Marletta L. Energy and cost evaluation of thermal bridge correction in Mediterranean climate. Energ Buildings 2011; 43: 2385-93.

Fokaides PA, Kalogirou SA. Application of infrared thermography for the determination of the overall heat transfer coefficient (U-value) in building envelopes. Appl Energ 2011; 88: 4358-65.

Giorgi LD, Bertola V, Cafaro E. Thermal convection in double glazed windows with structured gap. Energy Build 2011; 43: 2034-8.

Gloriant F, Tittelein P, Joulin A, Lassue Stéphane. Modeling a triple-glazed supply-air window. Build Environ 2015; 84: 1-9.

Google Maps.

Hang Y, Niu JL, Chung TM. Study on performance of energy-efficient retrofitting measures on commercial building external walls in cooling dominant cities. Appl Energ 2013; 103:97-108.

Hughes TJR. The Finite Element Method: Linear Static and Dynamic Finite Element Analysis. Dover Publications, New York; 2000.

Incropera FP, DeWitt DP, Bergman TL, Lavine AS. Fundamentals of heat and mass transfer. 6th ed. John Wiley & Sons Inc.; 2007.

Ismail KAR, Salinas CT, Henriquez JR. A comparative study of naturally ventilated and gas filled windows for hot climates. Energy Convers Manag 2009; 50:1691-703.

Kapsalaki M, Leal V, Santamouris M. A methodology for economic efficient design of Net Zero Energy Buildings. Energ Buildings 2012; 55:765-78.

Lei HY, Dai CS. Heat transfer analysis of centric borehole heat exchanger with different backfill materials. Proceedings World Geothermal Congress 2015, Melbourne, Australia.

Lewis RW, Nithiarasu P, Seetharamu KN. Fundamentals of the finite element method for heat and fluid flow. John Wiley & Sons Inc.; 2004.

Linee Guida Nazionali per la Certificazione Energetica del 26 giugno 2009.

Lo Russo S, Boffa C, Civita MV. Low-enthalpy geothermal energy: An opportunity to meet increasing energy needs and reduce CO2 and atmospheric pollutant emissions in Piemonte, Italy. Geothermics 2009; 38: 254-62.

Lund JW. The use of down-hole heat exchangers. Geo-heat Center, Oregon Institute of Technology, Klamath Falls, OR, USA, 1999.

McGrattan K, Hostikka S, McDermott R, Floyd J, Weinschenk C, Overholt K. Fire Dynamic Simulator User's Guide. NIST Special Publication 1019, 6thEdition; 2013.

Mazzarella L, Piterà LA. Linee Guida per l'efficienza energetica; 2013.

Michopoulos A, Papakostas KT, Kyriakis N. Potential of autonomous ground-coupled heat pump system installations in Greece. Appl Energ 2011; 88: 2122-9.

Mohelnikova J. Materials for reflective coatings of window glass applications. Constr Build Mater 2009; 23:1993 - 8.

Muñoz M, Garat P, Flores-Aqueveque V, Vargas G, Rebolledo S, Sepùlveda S, Daniele L, Morata D. Estimating low-enthalpy geothermal energy potential for district heating in Santiago Basin-Chile. Renew Energ 2015; 76: 186-95.

Nikishov GP. Introduction to the Finite Element Method. Lecture Notes; 2004.

Ostergaard PA, Lund H. A renewable energy system in Friederikshavn using low-temperature geothermal energy for district heating. Appl Energ 2011; 88: 479-87.

Özisik MN. Finite difference methods in heat transfer. CRC Press, Inc.; 1994.

Pentenrieder B. Finite element solution of heat conduction problems in complicated 3D geometries using the multi-grid method. Degree Diss., Technische Universität München, Germany, 2005.

Piscopo V, Barbieri M, Monetti V, Pagano G, Pistoni S, Ruggi E, Stanzione D. Hydrogeology of thermal waters in Viterbo area, Central Italy. Hydrogeol J 2006; 14: 1508-21.

Scrocca D, Doglioni C, Innocenti F. Constraints for an interpretation of the Italian geodynamics:a review. Mem Descr Carta Geol d'It, 2003; LXII: 15-46.

Shengjun Z, Huaixin W, Tao G. Performance comparison and parametric optimization of subcritical Organic Rankine Cycle (ORC) and transcritical power cycle system for low-temperature geothermal power generation. Appl Energ 2011; 88: 2740-54.

Terés-Zubiaga J, Martìn K, Erkoreka A, Sala JM. Field assessment of thermal behaviour of social housing apartments in Bilbao, Northern Spain. Energ Buildings 2013;67:118-35.

Theodosiou TG, Papadopoulos AM. The impact of thermal bridges on the energy demand of buildings with double brick wall constructions. Energ Buildings 2008; 40: 2083-9.

ThermaCAM User's manual, FLIR Systems, 2007.

UNI 5364:1976. Impianti di riscaldamento ad acqua calda. Regole per la presentazione dell'offerta e per il collaudo.

UNI 10349:1994. Riscaldamento e raffrescamento degli edifici. Dati climatici.

UNI 10339:1995. Impianti aeraulici ai fini del benessere – Generalità, classificazione e requisiti.

UNI EN ISO 6946:2008. Componenti ed elementi per edilizia - Resistenza termica e trasmittanza termica - Metodo di calcolo.

UNI EN ISO 10077: 2007. Prestazione termica di finestre, porte e chiusure oscuranti - Calcolo della trasmittanza termica - Parte 1: Generalità.

UNI EN ISO 10211:2008. Ponti termici in edilizia - Flussi termici e temperature superficiali - Calcoli dettagliati.

UNI TS 11300/1: Determinazione del fabbisogno di energia termica dell'edificio per la climatizzazione invernale ed estiva.

UNI TS 11300/2: Determinazione del fabbisogno di energia primaria e dei rendimenti per la climatizzazione invernale e per la produzione di ACS.

UNI TS 11300/3: Determinazione del fabbisogno di energia primaria e dei rendimenti per la climatizzazione estiva.

UNI TS 11300/4: Utilizzo di energie rinnovabili e di altri metodi di generazione per la climatizzazione invernale e per la climatizzazione estiva.

Vollmer M and Möllmann KP. Infrared thermal imaging. Wiley VCH; 2010.

Wang HB. Heat transfer analysis of components of construction exposed to fire: A theoretical, numerical and experimental approach. Doctoral Diss., University of Salford, Manchester, England; 1995.

www.mathworks.com

www.flir.com

www.thermopedia.com

Zhao H, Magoulès F. A review on the prediction of building energy consumption. Renev Sust Energ Rev 2012; 16:3586-92.

Zienkiewicz OC and Taylor RL. The Finite Element Method. Volume 1, Butterworth and Heinemann; 2000.

Zilli D. Studio e sviluppo di edifici ad energia quasi zero del Corpo Forestale dello Stato. Doctoral Diss., Tuscia University, Italy, 2014.